De faseverdeling van een tweefasige koelmiddelstroom over een stotende T-junctie

Phase Distribution of a Refrigerant Two-Phase Flow over an Impacting T-Junction

Marijn Billiet

Promotor: prof. dr. ir. M. De Paepe
Proefschrift ingediend tot het behalen van de graad van
Doctor in de ingenieurswetenschappen: werktuigkunde-elektrotechniek

UNIVERSITEIT
GENT

Vakgroep Mechanica van Stroming, Warmte en Verbranding
Voorzitter: prof. dr. ir. P. De Baets
Faculteit Ingenieurswetenschappen en Architectuur
Academiejaar 2018 - 2019

ISBN 978-94-6355-191-5
NUR 961
Wettelijk depot: D/2018/10.500/109

Examination board

Prof. Dr. ir. Patrick De Baets (UGent, Chair)
Prof. Dr. ir. Michel De Paepe (UGent, Supervisor)
Prof. Dr. Remi Revellin (INSA Lyon)
Prof. Dr. Cees van der Geld (TU Eindhoven)
Prof. Dr. ir. Marc Vantorre (UGent)
Prof. Dr. ir.Joris Degroote (UGent, Secretary)
Dr. ir. Bernd Ameel (Daikin Europe)
Prof. Dr. ir. Tom De Mulder (UGent)

Promotor: prof. dr. ir. M. De Paepe
Proefschrift tot het behalen van de graad van
Doctor in de ingenieurswetenschappen:
werktuigkunde - elektrotechniek

UNIVERSITEIT
GENT

Vakgroep Mechanica van Stroming, Warmte en
Verbranding
Faculteit Ingenieurswetenschappen en Architectuur
Academiejaar 2018-2019

Universiteit Gent
Faculteit Ingenieurswetenschappen en Architectuur

Vakgroep Mechanica van Stroming, Warmte en Verbranding
Sint-Pietersnieuwstraat 41, B-9000 Gent, België

Tel.: +32 9 264 32 88
Fax.: +32 9 264 35 90

Dit werk kwam tot stand in het kader van een doctoraatsbeurs voor strategisch basisonderzoek van het Agentschap voor Innovatie door Wetenschap en Technologie (IWT-SB-141733).

Promotor: prof. dr. ir. M. De Paepe
Proefschrift tot het behalen van de graad van
Doctor in de ingenieurswetenschappen:
werktuigkunde - elektrotechniek

UNIVERSITEIT
GENT

Vakgroep Mechanica van Stroming, Warmte en
Verbranding
Faculteit Ingenieurswetenschappen en Architectuur
Academiejaar 2018-2019

Dankwoord

Ik zou graag eerst enkele mensen bedanken die direct of indirect hebben bijgedragen aan het tot stand komen van deze doctoraatsverhandeling.

Vooraleerst wil ik mijn promotor Michel De Paepe bedanken om mij deze kans te bieden en me te begeleiden tijdens de afgelopen 4 jaar. Verder wil ik hem ook bedanken voor het ter beschikking stellen van de fondsen nodig om mijn onderzoek uit te voeren.

Verder wil ik ook al mijn collega's bedanken voor de aangename sfeer op de werkvloer.

In het bijzonder wil ik Frederik Martens en Patrick De Pue bedanken voor hun technische ondersteuning.

Verder wil ik ook Bernd Ameel bedanken voor zijn advies en het bijbrengen van nieuwe inzichten.

Hartelijk dank aan Steven Lecompte en Flavio Brighenti voor het nalezen van mijn boek.

Yves Maenhout wordt bedankt voor de ICT ondersteuning.

Ook dank aan Griet Blondé, Annie Harri en Annick De Coster voor hun administratieve ondersteuning.

Tenslotte wil ik mijn vriendin Tineke, mijn ouders, mijn broer en de rest van de familie danken voor hun steun en interesse.

Gent, oktober 2018
Marijn Billiet

Table of Contents

Dankwoord i

Table of Contents iii

List of Figures vii

List of Tables xi

Nomenclature xiii

Nederlandse samenvatting xvii

English summary xxi

1 Introduction 1
- 1.1 Transition to Renewables . . . 1
- 1.2 Heat pump as heating and cooling source . . . 2
- 1.3 Objectives . . . 6
- 1.4 Outline . . . 6

2 Two-phase maldistribution in the literature 9
- 2.1 Introduction to two-phase flow . . . 9
  - 2.1.1 Two-phase flow parameters . . . 9
  - 2.1.2 Flow regimes and flow regime maps . . . 12
- 2.2 Impacting T-junction . . . 15
  - 2.2.1 Representation of results . . . 16
- 2.3 Existing research on impacting T-junctions . . . 19
  - 2.3.1 Horizontal impacting T-junctions . . . 19
    - 2.3.1.1 Influence of the inlet superficial velocities on the phase distribution . . . 19
    - 2.3.1.2 Influence of channel diameter on phase distribution . . . 21
    - 2.3.1.3 Influence of fluid properties on phase distribution 22
    - 2.3.1.4 Flow regime maps for impacting T-junctions . . 22
    - 2.3.1.5 Pressure drop over an impacting T-junction . . . 23
  - 2.3.2 Inclined impacting T-junctions . . . 24

2.3.3 Models available in the literature 27
2.4 Impacting Y-junction 29
2.5 Conclusion 30

3 Experimental setup **31**
3.1 Two-phase flow conditioner 32
3.1.1 Refrigerant loop 33
3.1.2 Cold water loop 34
3.1.3 Hot water loop 34
3.1.4 Saturation pressure control loop 35
3.2 Test Section 36
3.2.1 Overview of the test section 36
3.2.2 Pressure gradient measurement 36
3.2.3 Void fraction sensor 38
3.3 Test methodology 40
3.3.1 Verification of the experimental setup 41

4 Experimental results **45**
4.1 How to compare experimental results? 46
4.2 Parameters influencing the phase distribution 48
4.2.1 Influence of the superficial liquid velocity J_l and the superficial vapour velocity J_g 48
4.2.2 Influence of the fluid properties 51
4.2.3 Influence of the inclination angle 57
4.3 Pressure drop over an impacting T-junction 59
4.4 Conclusion 64

5 Phase distribution model **65**
5.1 Evaluation of the existing models 66
5.1.1 Evaluation using the data available in literature 67
5.1.2 Evaluation using the experimental data 68
5.2 Description of a new phase distribution model for horizontal impacting T-junctions 71
5.2.1 Conservation of mass 71
5.2.2 Conservation of momentum 72
5.2.3 Conservation of energy 75
5.2.4 Model implementation 76
5.3 Validation of horizontal phase distribution model 78
5.4 Extension to inclined T-junctions 82
5.5 Conclusions 84

6 Conclusion **85**
6.1 Conclusion 85
6.2 Future work 87

A Uncertainty Analysis **89**
A.1 Measurements . . . 89
A.1.1 Temperature measurement . . . 89
A.1.2 Pressure measurement . . . 90
A.1.3 Flow measurement . . . 91
A.1.4 Electrical power measurements . . . 91
A.2 Thermophysical properties . . . 92
A.3 Processing raw data and its uncertainty . . . 92
A.3.1 Mass flux . . . 92
A.3.2 Heat transferred to the refrigerant in the preheater . . . 93
A.3.3 Vapour quality after the preheater . . . 96
A.3.4 Heat transferred to the refrigerant in the evaporator section 96
A.3.5 Vapour quality at the inlet of a T-junction's branch . . . 98
A.3.6 $dP_{junction}$ . . . 98
A.4 P& ID . . . 98

B Void fraction measurements **101**
B.1 Measurement method . . . 101
B.1.1 Calibration curve . . . 102
B.2 Comparison with existing models . . . 103
B.3 Flow regime determination . . . 104

C List of experimental data **107**

D Evaluation of existing phase distribution models **111**
D.1 Models of Azzopardi *et al.* [57, 58] . . . 111
D.2 Models of Ottens *et al.* [52] . . . 114
D.3 Model of Hong and Christon [53] . . . 116
D.4 Model of Chien and Rubel [54, 73] . . . 117
D.5 Model of El-Shaboury *et al.* [47] . . . 118
D.6 Conclusion . . . 119

E Publications **121**
E.1 Related publications in peer-reviewed international journals . . . 121
E.2 Other publications in peer-reviewed international journals . . . 121
E.3 Related publications in proceedings of international conferences . 122
E.4 Other publications in proceedings of international conferences . . 122

References **125**

List of Figures

1.1 The yearly mean CO_2 concentrations measured at Mauna Loa Observatory, (Hawaii) [3] and the yearly global temperature anomaly [4] as function of time. 1
1.2 The primary energy use of the different sectors in the European Union [7]. 2
1.3 A basic thermodynamic heat pump cycle depicted in a T-s diagram. 3
1.4 Different types of distributors. 3
1.5 Configuration of the flash gas bypass method of Tuo *et al.* [12] . . 4
1.6 A vapour compression cycle equiped with individual superheat control (Kim *et al.* [15]) 5

2.1 The different void fraction definitions: (a) chordal, (b) cross-sectional and (c) volumetric void fraction. 10
2.2 An example of a flow regime map of Wojtan et al. [28]. The blue lines are the transition lines. In the adapted version of Barbieri *et al.* [29] the dashed blue line is replaced by the green dashed line. . 13
2.3 The probabilistic flow regime map of Canière *et al.* [30] drawn together with the flow regime map of Wojtan et al. [28] (thin black lines). The red, blue and green symbols are measurements with respectively a slug, an intermittent and annular flow according to the model of Canière *et al.* [30]. 14
2.4 Schematic representation of an impacting T-junction. 15
2.5 The different orientation angles of an impacting T-junction. 15
2.6 Different methods of representing phase distribution data (dotted line = even phase distribution). 16
2.7 Phase distribution data of El-Shaboury *et al.* [47] for the wavy and stratified-wavy flow regimes. 20
2.8 The pressure distribution over an impacting T-junction [47]. 24
2.9 F_g – F_l graphs of water-air (23 °C — 150 kPa) phase distribution experiments [42], the experiments were conducted at different inlet conditions and at different branch inclination angles. 26
2.10 Flow separation at varied angles of inclination for in $\dot{m}$ = 30 g/s and x = 15 % [12]. 27

3.1 Schematic overview of the two-phase flow conditioner. The conditioner consists of 4 main loops: a refrigerant loop, a cold water loop, a hot water loop and a saturation pressure control loop. 32
3.2 Schematic overview of the refrigerant loop. The liquid refrigerant is pumped out the buffer vessel through a mass flow meter, a preheater, a test section and a condensor. 33
3.3 Schematic overview of the cold water loop. A chiller provides a chilled water-glycol mixture for the condenser in the refrigerant loop. 34
3.4 Schematic overview of the hot water loop. The hot water loop provides hot water for the preheater in the refrigerant loop. 34
3.5 Schematic overview of the test section. 36
3.7 Picture of the pressure gradient measuring equipment 37
3.6 Positioning of the pressure tabs at the test section 37
3.8 Schematic representation of a simplified void fraction sensor. . . . 38
3.9 The relation between the void fraction time trace and the flow regime [64]. 39
3.10 Cross section of the void fraction sensor [22]. 39
3.11 The comparison of the variation of F_g-value in time during one experiment for different flow regimes. 41
3.12 The conservation of energy over the preheater for a single phase R32. 42
3.13 The conservation of energy over the test section for a single phase R32. 43
3.14 The Fanning friction factors f as function of the Reynolds number. The experimental values measured in the inlet and outlets of the T-junction are compared with the correlation of Gnielinski *et al.* [66]. 43

4.1 The liquid mass fraction F_l as function of the vapour mass fraction F_g of an R32 experiment (T_{sat} = 10 °C; J_g = 1 m/s; J_l = 0.2 m/s) with the fitted $F_g - F_l$ line. 46
4.2 The histogram of the slope b obtained by the Monte-Carlo method compared with the Gaussian probability density function. 48
4.3 Inlet conditions (vapour quality and mass flux) of the experiments of R32 at a saturation temperature of 10 °C displayed in a flow regime map of Wojtan *et al.* [28] extended by Barbieri *et al.* [29] (S: Stratified; SW: Stratified-Wavy; I: Intermittent; A: Annular; SL: Slug; M: Mist; D: Dry-out) 49
4.4 Inlet superficial velocities of the experiments of R32 at a saturation temperature of 10 °C displayed in a flow regime map of Wojtan *et al.* [28] extended by Barbieri *et al.* [29] (S: Stratified; SW: Stratified-Wavy; I: Intermittent; A: Annular; SL: Slug) 50
4.5 Slope b as function of the inlet superficial vapour velocity for different inlet superficial liquid velocities (R32; T_{sat} = 10 °C). . . 51

4.6 The liquid mass fraction F_l as function of the vapour mass fraction F_g for different superficial vapour velocities J_g and a superficial liquid velocity of $0.01\,\mathrm{m/s}$ [47]. 52
4.7 Slope b as function of the inlet superficial vapour velocity for different inlet superficial liquid velocities (R32; T_{sat} = 20 °C). . . 53
4.8 Slope b as function of the inlet superficial vapour velocity for different inlet superficial liquid velocities and different refrigerants. 54
4.9 Slope b as function of the density ratio $\frac{\rho_g}{\rho_l}$ for different inlet superficial liquid velocities, saturation temperatures and refrigerants. 55
4.10 Slope b as function of the momentum ratio of the inlet $\frac{\dot{m}_{1,g} \cdot v_{1,g}}{\dot{m}_{1,l} \cdot v_{1,l}}$ for different inlet superficial liquid velocities, saturation temperatures and refrigerants. 55
4.11 Slope b as function of the vapour-liquid viscosity ratio $\frac{\mu_g}{\mu_l}$ for different inlet superficial liquid velocities, saturation temperatures and refrigerants. 56
4.12 Slope b as function of the surface tension for different inlet superficial liquid velocities, saturation temperatures and refrigerants. 56
4.13 The liquid mass fraction towards the downward-facing outlet as function of the vapour mass fraction towards the same outlet for different T-junction inclination angles θ (R32; T_{sat} = 10 °C). . . . 57
4.14 The liquid mass fraction towards the downward-facing outlet as function of the vapour mass fraction towards the same outlet for different T-junction inclination angles θ (R125; T_{sat} = 10 °C). . . 58
4.15 Method for determining the pressure drop over a T-junction. The experimental data is used to extrapolate at the junction. 59
4.16 The pressure difference measured between the inlet of the test section and just before the first evaporator heater of outlet 2 as function of the pressure difference determined using extrapolation. 60
4.17 Experimentally obtained K_{1i}-values (all refrigerants tested) as function of the mass fraction flowing towards the outlet grouped by the flow regimes. 62
4.18 The pressure drop determined using the model as a function of the experimentally determined pressure drop. 63

5.1 Control volume of the phase distribution model. 71
5.2 The model's values of the term ① as function of the experimental values for all refrigerants. 74
5.3 The solving algorithm of the model. 77
5.4 The predicted liquid fraction F_l as function of the experimental value for the data of this work. 79
5.5 The predicted liquid fraction F_g as function of the experimental value for the data of this work. 80
5.6 The predicted liquid fraction F_l as function of the experimental value for the water-steam data [53, 54, 73]. 81

5.7 The predicted liquid fraction F_l as function of the experimental value for this work's inclined data. 83
5.8 The predicted vapour fraction F_g as function of the experimental value for this work's inclined data. 83

A.1 A schematic representation of the model used to estimate the heat losses to the environment at the preheater. (refrigerant; 1-2: inner tube wall; 2-3: hot water; 3-4: outer tube wall; 4-5: insulation; ambient air) 94
A.2 A schematic representation of the model used to estimate the heat losses to the environment at the evaporator section. (refrigerant; tube wall; electrical heater; 1-2: insulation; ambient air) 97
A.3 P& ID of the flow conditioner. 99
A.4 P& ID of the test section. 100

B.1 The void fraction sensor calibration curves for R32. 102
B.2 The simplified geometries implemented in the FEMM [87] simulations. (black: Kapton tube wall; blue: liquid phase; white: vapour phase; orange: electrodes) 102
B.3 The void fractions measured experimentally compared to the void fractions determined with the model of *Steiner* [26] 103
B.4 The void fractions measured experimentally compared to the void fractions determined with the model of *Shoham et al.* [88] 104
B.5 The difference between the 3rd and 4th wavelet variance as function of the superficial vapour velocity (R32; T_{sat} = 10 °C; J_l = $0.2\,\mathrm{m/s}$). The dashed lines indicate the flow regime transitions according to Wojtan *et al.* [28]. 105

List of Tables

2.1 Overview of literature about two-phase distribution over an impacting T-junction 18
2.2 Summary of the influences studied in the literature. 30

3.1 The inlet parameters of the experimental setup with their range and uncertainty. 40

4.1 The properties and the slope b determined using the model of El-Shaboury *et al.* [47] for a water-air mixture (T = 20 °C; P = 1.5×10^5 Pa). 52
4.2 Flow regime dependent coefficients of the K_{1i}-model with its 95 % confidence intervals. 61

5.1 The existing models which were evaluated with their design mixture and their input and output parameters. 66
5.2 The prediction capabilities of the model of Chien and Rubel [54, 73] for the data found in the literature. 67
5.3 The predictive capabilities of existing phase distribution models for water-air mixtures (277 datapoints). 68
5.4 The predictive capabilities of existing phase distribution models for water-steam mixtures (174 datapoints). 68
5.5 The predictive capabilities of existing phase distribution models for the experimental data grouped by refrigerant. 69
5.6 The predictive capabilities of existing phase distribution models for the experimental data grouped by inlet flow regime. 70
5.7 Fitting constants of the momentum equation. 74
5.8 The predictive capability of the new phase distribution model (F_l) for the data gathered in this work grouped by refrigerant. 78
5.9 The predictive capability of the new phase distribution model (F_l) for the experimental data grouped by inlet flow regime. 78
5.10 The predictive capability of the new phase distribution model for the experimental data grouped by refrigerant. 79
5.11 The predictive capability of the new phase distribution model (F_l) for this work's inclined data. 82

A.1 Uncertainty of Pressure Transducers 91
A.2 The uncertainty of the thermophysical properties given by Coolprop for different fluids. 92

B.1 The mean absolute error (MAE) and the mean relative error (MRE) of Steiner's model [26] for the different flow regimes. 103
B.2 The mean absolute error (MAE) and the mean relative error (MRE) of Shoham's models [88] for the different flow regimes. 104

C.1 The overview of the experimental inlet conditions tested in this work (part 1). 108
C.2 The overview of the experimental inlet conditions tested in this work (part 2). 109

D.1 The prediction capabilities of Azzopardi's [57] model for the data found in the literature. 112
D.2 The prediction capabilities of Azzopardi's [58] model for the data found in the literature. 113
D.3 The prediction capabilities of the double stream model [52] for the data found in the literature. 114
D.4 The prediction capabilities of the advanced double stream model [52] for the data found in the literature. 115
D.5 The prediction capabilities of the model of Hong and Christon [53] for the data found in the literature. 116
D.6 The prediction capabilities of the model of Chien and Rubel [54, 73] for the data found in the literature. 117
D.7 The prediction capabilities of the model of El-Shaboury *et al.* [47] for the data found in the literature. 118

Nomenclature

A	annular flow
B	bubble flow
COP	Coefficient of Performance
D	dry-out flow
EU	European Union
I	intermittent flow
M	mist flow
MAD	mean absolute deviation
MAE	mean absolute error
MD	mean deviation
MODWT	maximum overlap wavelet transform
MRE	mean relative error
PI	prediction interval
PID	proportional integral derivative
S	stratified flow
SE	standard error
SL	slug flow
SW	stratified-wavy flow

Greek symbols

$\bar{\mu}$	mean	
$\bar{\sigma}$	standard deviation	
χ^2	Chi squared distribution	
δ	error of	[-]
ϵ	cross-sectional void fraction	[-]
ϵ_0	absolute permittivity of free space	$[\mathrm{F/m}]$
$\hat{\rho}$	homogeneous density	$[\mathrm{kg/m^3}]$
λ	Laplace Constant	$[\mathrm{m}]$
μ	dynamic viscosity	$[\mathrm{N{\cdot}s/m^2}]$
ϕ	inclination angle of the inlet with respect to the horizontal plane	[°]
ρ	density	$[\mathrm{kg/m^3}]$
σ	surface tension	$[\mathrm{N/m}]$
θ	inclination angle of outlet branch 2 with respect to the horizontal plane	[°]
ξ	volume	$[\mathrm{m^3}]$

Symbols

$\bar{D}$	mean diameter	$[\mathrm{m}]$
$\dot{M}$	momentum flux	$[\mathrm{kg/(m{\cdot}s^2)}]$
$\dot{m}$	mass flow rate	$[\mathrm{kg/s}]$
$\dot{M}_r$	momentum flux ratio	[-]
ϵ_r	dielectric constant (= relative permittivity)	[-]
$\hat{v}$	homogeneous velocity	$[\mathrm{m/s}]$
A	surface area	$[\mathrm{m^2}]$
a	intercept	[-]
A_c	cross-sectional area	$[\mathrm{m^2}]$
b	slope	[-]
C	capacity	[F]
C'	capacity per length	$[\mathrm{F/m}]$
C_p	specific heat capacity at constant pressure	$[\mathrm{J/(kg{\cdot}K)}]$
D	diameter	$[\mathrm{m}]$
E	the amount of liquid entrained in the vapour core as droplets	[-]
F	force	$[\mathrm{kg{\cdot}m/s^2}]$
f	frequency	[Hz]
F_g	the mass fraction of the vapour phase that goes to one branch	[-]
F_l	the mass fraction of the liquid phase that goes to one branch	[-]
G	mass flux	$[\mathrm{kg/(m^2{\cdot}s)}]$
g	standard gravity	$[9.81\,\mathrm{m/s^2}]$
H	enthalpy	$[\mathrm{J/kg}]$
h	convection coefficient	$[\mathrm{W/(m^2{\cdot}K)}]$
I	current	[A]
J	superficial velocity	$[\mathrm{m/s}]$
K	irreversible loss coefficient	[-]
k	thermal conductivity	$[\mathrm{W/(m{\cdot}K)}]$
L	length	$[\mathrm{m}]$
Nu	Nusselt number	[-]
P	pressure	[Pa]
$P[\ ]$	probability of	[-]
Pr	Prandtl number	[-]
Q	heat transfer	$[\mathrm{J/s}]$
R	thermal resistance	$[\mathrm{K/W}]$
S	velocity ratio (slip ratio)	[-]
s	entropy	$[\mathrm{J/K}]$
T	temperature	[K]
V	voltage	[V]
v	real velocity	$[\mathrm{m/s}]$
$v^\star$	wavelet variance	[-]
W	work	$[\mathrm{J/s}]$
x	vapour quality	[-]

Subscripts

$b2$	outlet branch 2
g	vapour
l	liquid
lg	liquid to gas
exp	experimental
i-a	intermittent to annular transition
i-sl	slug to intermittent transition
pred	predicted
sat	at saturation

Nederlandse samenvatting –Summary in Dutch–

Klimaatverandering is momenteel een wereldwijde zorg. Het verwarmen en koelen van onze woningen draagt sterk bij tot deze klimaatverandering. Momenteel wordt $40\,\%$ van het totale energiegebruik in de Europese Unie gebruikt door gebouwen. Dit is $36\,\%$ van de Europese CO_2 uitstoot [1]. Om het energiegebruik van een woning te doen dalen, moet men de isolatiegraad van de huidige woningvoorraad verhogen. Bovendien moet men de huidige verwarmingsinstallatie vervangen door een installatie die niet afhankelijk is van fossiele brandstoffen. Een mogelijke kandidaat is de warmtepomp. Deze kan op hernieuwbare energie werken en heeft een veel hogere efficiëntie dan de conventionele systemen.

Een warmtepomp maakt gebruik van een thermodynamische cyclus om warmte met een lage temperatuur naar een hogere temperatuur te brengen. Deze warmtepompcyclus is een gesloten cyclus bestaande uit 4 hoofdcomponenten: een compressor, een condensor, een expansieventiel en een verdamper. Binnen deze gesloten cyclus stroomt een fluïdum dat men een koelmiddel noemt. Het koelmiddel bevindt zich in het tweefasig gebied wanneer het de verdamper bereikt. Een tweefasige stroming is een mengsel van 2 fasen, in dit geval een vloeistof en een gas. Deze tweefasige stroming moet dan verdeeld worden over de verschillende parallelle kanalen van de verdamper. Dit wordt gedaan aan de hand van een verdeelkop. Echter, deze verdeling van de verschillende fasen over de parallelle kanalen is vaak niet homogeen. Deze niet-homogene verdeling kan worden veroorzaakt door een incorrecte plaatsing van de warmtepomp, productietoleranties, een fluctuerende warmtevraag, bevuiling en indirecte oorzaken die de drukval in de parallelle kanalen beïnvloeden zoals ijsvorming of bevuiling aan de luchtzijde van de verdamper. Deze niet-homogene verdeling resulteert in een significante daling van de COP (Coefficient of Performance) en de capaciteit van de warmtepomp.

Dit boek zal zich beperken tot circulaire verdeelkoppen met slechts 2 uitgangen. Deze geometrie kan men vereenvoudigen tot een stotende T-junctie. Een stotende T-junctie is een T-junctie waarvan de twee uitlaten loodrecht op de inlaat staan. Het doel van dit werk is om de kennisleemtes in de literatuur te onderzoeken en een nieuw fasedistributiemodel te ontwikkelen.

Om te starten werd er een overzicht gemaakt van het bestaande onderzoek en werd er gewezen op de ontbrekende delen. Allereerst observeerden

verscheidene auteurs een anomaliteit bij de invloed van de oppervlaktesnelheid op de faseverdeling wanneer er een overgang is tussen stromingspatronen. Het eerste doel van dit werk is dus om de invloed van de stromingspatronen op de faseverdeling in detail te bestuderen. Verder werden in het verleden de meeste experimenten uitgevoerd met water-lucht mengsels. Er is dus weinig informatie beschikbaar over de invloed van de stofeigenschappen op de verdeling van de fasen. Dit werk zal de huidige dataset verder uitbreiden met experimentele data, uitgevoerd met verschillende koelmiddelen. Het zal verder ook de invloed van verschillende stofeigenschappen op de verdeling van de fasen bespreken.

Om deze faseverdeling over een stotende T-junctie te bestuderen, werd een nieuwe proefopstelling ontworpen. Deze proefopstelling kan een koelmiddelstroom genereren met een maximale massa flux van $700\,\mathrm{kg/(m^2{\cdot}s)}$ op een saturatietemperatuur tussen $10\,°\mathrm{C}$ en $20\,°\mathrm{C}$ en met een dampkwaliteit tussen 0 en 1. De binnendiameter van de T-junctie is $8\,\mathrm{mm}$. In totaal werden er 696 experimenten uitgevoerd met vier verschillende koelmiddelen: R32, R125, R1234ze en R134a. Met andere woorden: de verdeling van de fases werd bepaald over een bereik van massafracties voor 60 verschillende inlaatcondities. De warmtebalans over de opstelling sluit met een gemiddelde fout van $2\,\%$ en deze fout is steeds kleiner dan $5\,\%$. De stabiliteit van de experimentele opstelling werd geverifieerd door enkele willekeurige experimenten te herhalen.

Om de experimentele resultaten te vergelijken werd een nieuwe kwantitatieve methode voorgesteld. Op basis van de experimentele resultaten werd een sterke invloed van het stromingspatroon op de verdeling van de fasen waargenomen. Wanneer men de oppervlaktesnelheid van de gasfase incrementeel verhoogt, kan men een discontinuïteit in de faseverdeling opmerken. Verder heeft de vloeistoffase een dalende voorkeur om naar de uitlaat met het laagste massadebiet te stromen met stijgende oppervlaktesnelheid van de gasfase, wanneer de oppervlaktesnelheid van de vloeistoffase groter of gelijk is dan $0.2\,\mathrm{m/s}$. Echter, wanneer de oppervlaktesnelheid van de vloeistoffase kleiner of gelijk is dan $0.1\,\mathrm{m/s}$ heeft de vloeistoffase een stijgende voorkeur om naar de uitlaat met het laagste massadebiet te stromen met stijgende oppervlaktesnelheid van de gasfase.

Verder werd de invloed van drie stofeigenschappen (densiteit, viscositeit en oppervlaktespanning) onderzocht. De viscositeit had geen invloed op de verdeling van de fasen over de T-junctie. Echter, de fasen worden meer homogeen verdeeld als de densiteitsverhouding (ρ_g/ρ_v) vergroot. Verder worden de fasen meer homogeen verdeeld als oppervlaktespanning verkleint.

Tijdens de experimenten werden de drukgradiënten over de T-junctie opgemeten. Deze drukgradiënten werden dan gebruikt om een model op te stellen die de drukval over de T-junctie kan voorspellen. Dit drukvalmodel is accurater voor de experimentele data verzameld tijdens dit werk, vergeleken met de modellen uit literatuur. Verder kan dit model de drukval voor verschillende stromingspatronen voorspellen.

Vooraleer er een nieuw fasedistributiemodel werd voorgesteld, werden zeven bestaande modellen geëvalueerd, gebruikmakend van bestaande data en de data verzameld in dit werk. Alle bestaande modellen werden ofwel ontwikkeld voor

water-lucht mengsels, ofwel voor water-stoom mengsels. Algemeen gezien is de voorspellende kracht van de modellen het grootst voor het mengsel waarvoor het model ontworpen is. Dus geen van de modellen neemt de invloed van de stofeigenschappen in rekening. Daaruit volgt dat geen enkel model de data verzameld in dit werk, nauwkeurig kan voorspellen.

In dit werk wordt er een nieuw fasedistributiemodel voorgesteld, op basis van de inzichten verworven tijdens het analyseren van de experimentele data. Het fasedistributiemodel is gebaseerd op de drie hoofdwetten: behoud van massa, impuls en energie. Dit model is geëvalueerd gebruikmakend van bestaande data en de data verzameld in dit werk. Het model werkt zeer goed voor de data verzameld in dit werk en is aanvaardbaar voor water-stoom mengsels en water-lucht mengsels.

Als laatste wordt dit nieuwe model uitgebreid naar een model voor gehelde stotende T-juncties. Het gehelde model kan de massa fractie van de vloeistoffase F_l correct voorspellen voor de data verzameld in dit werk. Echter, de voorspelling van de massafractie van de gasfase F_g is minder goed dan van het horizontale model.

English summary

Climate change is a major global concern. Heating and cooling of buildings contributes significantly to the climate change. Currently, $40\,\%$ of the total energy use and $36\,\%$ of the total CO_2 emissions in the European Union (EU) arise from buildings [1]. To decrease the emissions of buildings, the insulation grade of the current building stock should be improved and the current heating and cooling installations should be replaced with ones not depending on fossil fuels. A promising technology is a heat pump, which can be powered by renewable energy and has a higher efficiency than conventional systems.

A heat pump uses a thermodynamic cycle to convert heat from a low temperature to a higher temperature. The heat pump cycle is a closed cycle containing a refrigerant and consisting of 4 components: a compressor, a condenser, an expansion valve and an evaporator. When the refrigerant enters the evaporator, it is typically in the two-phase region. A two-phase flow is a flow consisting of two phases which are in this case liquid and vapour. To distribute the two-phase flow over the parallel tubes of the evaporator a distributor is used. However, this distribution is often not homogeneous. Maldistribution can occur due to improper placement of the heat pump, production tolerances, varying heat loads, fouling and indirect causes which affect the pressure gradient in the parallel sections like frosting and dirt accumulation at the air side. This maldistribution results in a significant drop in coefficient of performance (COP) and capacity of the heat pump [2].

This work limits its scope to a tubular distributor head with only two outlets. This geometry can be reduced to an impacting T-junction. An impacting T-junction is a T-junction of which the two outlets are perpendicular to the inlet tube. The purpose of this work is to fill the gaps in literature concerning the phase distribution over an impacting T-junction and to develop a new phase distribution model. To start, this work gives the overview of the current state of art and tries to indicate the gaps. Several authors found an inconsistency of the influence of the inlet superficial velocities when there is a flow regime transition. Hence, a first goal of this work is to study the influence of the inlet superficial velocities on the phase distribution in the vicinity of flow regime transitions. Further, most experiments found in literature are executed with water-air mixtures. Hence, little information is available on the influence of fluid properties on the phase distribution. This work will add extra data to literature for different refrigerants and discusses the influence of different fluid properties.

To fill these gaps in literature, an experimental setup was developed which

allows to test the phase distribution of two-phase refrigerant flows over an impacting T-junction. The setup is capable of testing refrigerant flows with a mass flux up to $700\,\mathrm{kg/(m^2{\cdot}s)}$ at a saturation temperature between $10\,°\mathrm{C}$ and $20\,°\mathrm{C}$ and with a vapour quality between 0 and 1. The diameter of the impacting T-junction is $8\,\mathrm{mm}$. In total 696 experiments were performed with four different refrigerants: R32, R125, R1234ze an R134a. In other words, the phase distribution over the whole mass fraction range of 60 different inlet flows was tested. The conservation of energy has an average error of $2\,\%$ and is always smaller than $5\,\%$. The consistency of the experimental setup was verified by repeating random experiments.

To compare the experimental results, a new quantitative method was proposed. Based on the experimental results, a strong influence of the flow regime on the phase distribution was observed. While sweeping through a range of inlet superficial vapour velocities, discontinuities in the phase distribution were observed at the flow regime transitions. Further, the liquid has a decreasing preference of flowing to the branch with the lowest mass flow rate with increasing inlet superficial vapour velocity for an inlet superficial liquid velocity equal or higher than $0.2\,\mathrm{m/s}$. In contrast, for an inlet superficial liquid velocity equal or lower than $0.1\,\mathrm{m/s}$, the liquid has a increasing preference of flowing to the branch with the lowest mass flow rate with increasing inlet superficial vapour velocity.

The influence of three fluid properties (density, viscosity and surface tension) was also investigated. The viscosity does not have any influence on the phase distribution. The phases are distributed more homogeneous when the density ratio (ρ_g/ρ_l) increases. The maldistribution of the phases increases with increasing surface tension.

During the experiments, the pressure gradient over the T-junction was measured. These pressure gradient measurements were used to create a model which predicts the pressure drop over the T-junctions. This new pressure drop model is more accurate for this work's data and expands the prediction capabilities to other flow regimes compared to models found in literature.

Before a new phase distribution model was proposed, the seven existing models were evaluated using the data from literature and this work's data. The models available were designed for either water-air or water-steam flows. In general, the models have the highest predictive capability for their design two-phase mixture. Hence, none of the models captures the influence of the fluid properties. Also, none of the models was able to predict this work's data properly.

A new model was proposed based on the insights gained from the experimental results. The model is based on three fundamental laws: conservation of mass, momentum and energy. The new model is then evaluated using this work's data and the data from literature. The new model works well for this work's data and is acceptable for the water-steam and water-air data. Finally, the model is extended to inclined impacting T-junctions. The inclined model is able to predict the liquid mass fraction F_l correctly for this work's data. However, the prediction of the vapour mass fraction F_g is less accurate compared to the horizontal model.

1 Introduction

1.1 Transition to Renewables

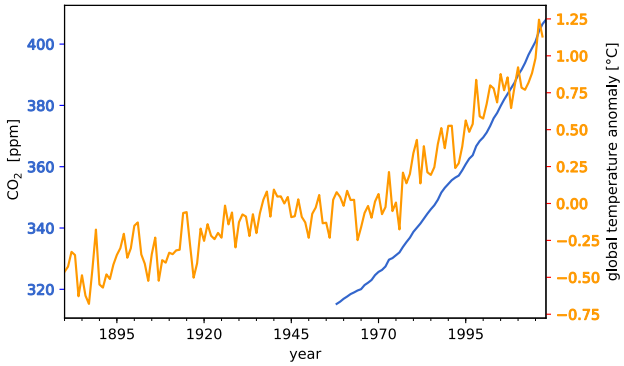

Figure 1.1: The yearly mean CO_2 concentrations measured at Mauna Loa Observatory, (Hawaii) [3] and the yearly global temperature anomaly [4] as function of time.

Climate change is a major global concern. The global mean temperature is increasing every year as shown in figure 1.1. This is mainly due to mankind's production of carbon dioxide emissions (figure 1.1) [5]. Global warming will have a large impact on life here on earth. It leads amongst others to more extreme

weather patterns, rising sea levels and fresh water shortage. In recent decades mitigating projects have been started, for example the European Union (EU) wants to reduce its carbon dioxide emissions significantly by 2050 [6].

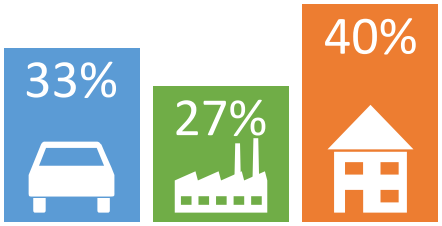

Figure 1.2: The primary energy use of the different sectors in the European Union [7].

Figure 1.2 shows that 40% of the primary energy in the European Union is used by buildings (residential and services). Most of the primary energy is still from a fossil fuel source leading to carbon emissions. Hence, buildings are responsible for 36% of all carbon dioxide emissions in the EU. Therefore, the European Commission sets a target to decrease the emissions of buildings by 90% by 2050. To reach this target, the Energy Performance of Buildings Directive obliges all new buildings from 2020 to be nearly zero energy buildings [1].

A large portion of the primary energy is used for heating and cooling of the building. To reduce the primary energy use, buildings should be insulated properly. For example, an uninsulated building of 50 years or older easily requires 5 times more energy for heating and cooling than a new well-insulated building [1]. To reduce the carbon emission even further, the small amount of energy still required for heating and cooling should originate from renewable energy sources. A heat pump is a highly efficient heating and cooling installation running on electricity that can be generated using renewables.

1.2 Heat pump as heating and cooling source

A heat pump uses a thermodynamic cycle to convert low temperature heat to a higher temperature. The thermodynamic cycle of an ideal basic heat pump is depicted in a T-s diagram in figure 1.3.

The basic heat pump cycle consists of 4 main components in a closed circuit: a compressor, a condenser, an expansion valve and an evaporator. The fluid used in the cycle is called the working fluid or refrigerant. First, the compressor compresses the gaseous refrigerant to a higher pressure. At this higher pressure, the refrigerant condenses at the saturation temperature corresponding with the imposed pressure. In this process, heat is rejected from the condenser. After the

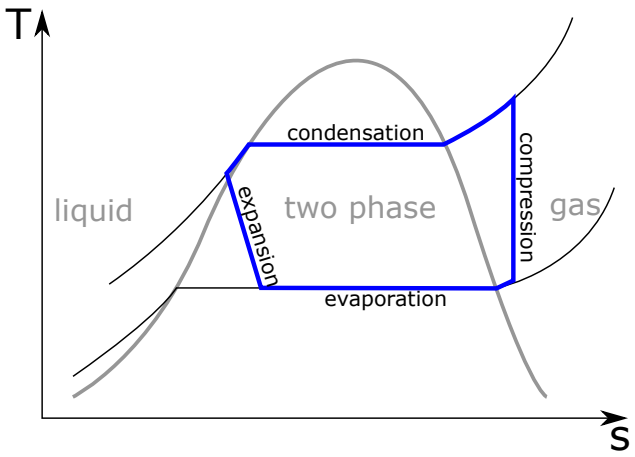

Figure 1.3: A basic thermodynamic heat pump cycle depicted in a T-s diagram.

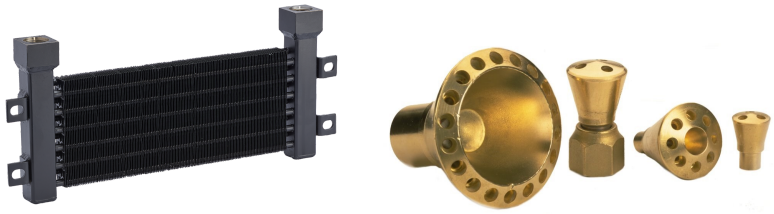

(a) Manifold type *(b) Tubular type*

Figure 1.4: Different types of distributors.

condenser, the liquid refrigerant is expanded over an expansion valve. This lowers the pressure. Due to the adiabatic expansion, part of the liquid flashes to a gaseous state. The refrigerant is now in the two-phase region. Finally, the two-phase refrigerant evaporates at a lower saturation temperature in the evaporator by extracting heat from a source. The Coefficient of Performance (COP) is a measure for the efficiency of the cycle. The COP is the heat released by the condenser divided by the work delivered by the compressor.

The refrigerant flow entering the evaporator is in the two-phase region as seen in figure 1.3. Furthermore, a typical evaporator, which is heated by air, consists of multiple parallel tubes to increase the heat transfer area while keeping the pressure drop low. To distribute the two-phase refrigerant mixture evenly over the different parallel tubes, a distributor is used. As shown in figure 1.4, two different distributor types exist: tubular distributors and manifold distributors. This work focuses on the tubular distributor.

In reality the distribution of the two phases is often not homogeneous over

a distributor. This can have different causes: manufacturing tolerances, uneven heat load of the different tubes, fouling, frost formation, partial load operation... Maldistribution leads to a non-uniform superheat at the outlet of the different tubes, which reduces the effectiveness of the heat exchanger. Several authors studied the effects of maldistribution in heat exchangers experimentally [8–12] and numerically [2, 13–18]. All authors agree that maldistribution leads to a reduction in capacity and the coefficient of performance (COP) of the heat pump. Depending on the boundary conditions, the reduction in capacity varied between 2% and 40%. According to Bach *et al.* [10], no strong maldistribution occurs in a well-designed and well-maintained heat pump. Hence, in reality the reduction in capacity will normally never reach values of 40%.

Vist [14] observed less capacity reduction caused by maldistribution for CO_2 than for R134a. Further he noticed a strong connection between the flow regime at the inlet and the extent of the maldistribution.

Mader *et al.* [2] did an economic study on the costs of phase maldistribution. The authors found that maldistribution will increase the annual operating cost up to 5%.

Several counteracting technologies for mitigating the performance drop due to maldistribution exist [18]. One of the simplest solutions is to avoid the origin of maldistribution such as reducing fouling and manufacturing tolerances. Mader *et al.* [2] noticed that oversizing of the evaporator can partly recover the maldistribution-induced losses. However, this increases the pressure losses and adds to the investment cost.

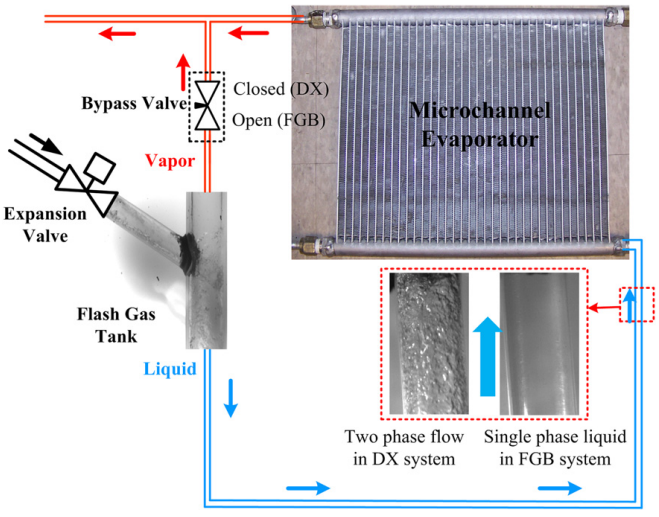

Figure 1.5: Configuration of the flash gas bypass method of Tuo et al. *[12]*

Tuo *et al.* [12] suggested a flash gas bypass system. After the expansion valve, the liquid phase is separated from the vapour using a flash tank or another separating device such as a vertical T-junction (see figure 1.5). The vapour bypasses the evaporator; only the liquid phase is evaporated in the evaporator. Hence, maldistribution of the phases cannot occur. However, uneven superheat can still occur if one tube is for example fouled. Further, the size and price of the phase separator is large. Milosevic *et al.* observed a 55% increase of their experimental setup's COP by applying the flash gas bypass when there is a large maldistribution.

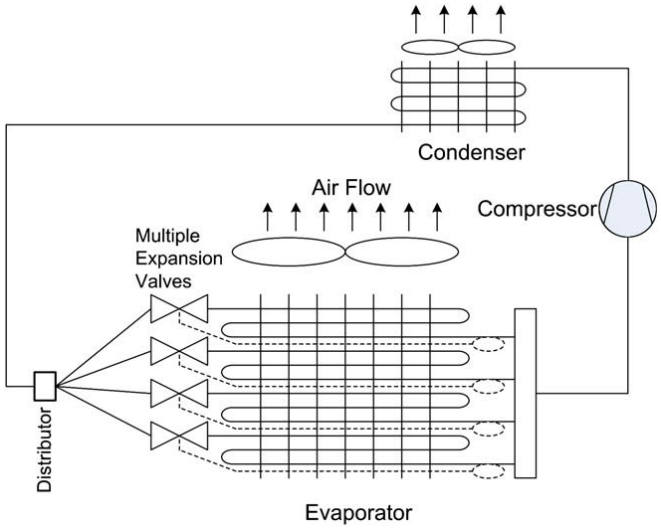

Figure 1.6: A vapour compression cycle equiped with individual superheat control (Kim et al. *[15])*

Both Kim *et al.* [15] and Kærn *et al.* [17] proposed individual superheat control of the parallel evaporator passes, but with different techniques. Kærn *et al.* [17] used an expensive expansion valve for each evaporator pass, while Kim *et al.* [15] uses one big expensive expansion valve combined with smaller and cheaper valves for the different passes (see figure 1.6). With both systems, one can change the mass flow rate of each pass and thereby control the outlet superheat. Technically this is the best solution but also the most expensive one. Mader *et al.* [18] did an economic study on the individual superheat control strategy. The payback time in an average climate is about 10 years while it is 2 years more for the flash gas bypass system. Finally, evaporator and distributor designs are currently optimised experimentally for its nominal operating condition. However this optimal design can be suboptimal for part load operation. The optimisation of the system over the whole working range would make the system more robust.

To develop optimised distributor designs, a good understanding and model should be available. However, currently little is known about the distribution of two-phase refrigerant flows in distributor heads. To the author's knowledge, only two experimental studies aimed to improve a tubular distributor head (Nakayama *et al.* [19] and Yoshioka *et al.* [20]). Both authors optimised the geometry of an existing distributor head using experimental techniques which leads to case specific models.

1.3 Objectives

The objective of this work is to get a better understanding of the phase maldistribution in tubular distributors. The work is confined to the distribution over two parallel circuits. In this case, the tubular distributor is reduced to an impacting T- or Y-junction. The main objective is to get a good understanding of parameters influencing the distribution of the two phases. Moreover, a new generalised phase distribution model for refrigerants will be developed.

The knowledge acquired in this work can be extended to multiple parallel circuits in future work. This will in turn improve evaporator designs. Hence, they can cope with manufacturer tolerances, partial load operation and are more robust against fouling and icing.

1.4 Outline

The manuscript is composed according to the following outline. In Chapter 2, the basic two-phase flow concepts necessary to understand the remainder of this thesis are explained. This chapter also gives a literature review about impacting T- and Y-junctions. The main influences on the phase distribution are discussed based on the literature. Furthermore, the phase distribution models available in the literature are summarised.

The working principle of the experimental setup is described in Chapter 3. This chapter also describes the void fraction sensor and its working principle, which was developed in the works of De Kerpel [21] and Canière [22]. This void fraction sensor was used to measure the void fraction and evaluate existing void fraction models (Appendix B). Finally, the measuring procedure used is explained briefly. The uncertainty analysis and the calibration procedures are found in Appendix A.

The experimental results are discussed in Chapter 4. First, a methodology to compare the experimental results is given. Further, the chapter discusses the main influences on the phase distribution over an impacting T-junction. In the last section, a pressure drop model is constructed.

The existing phase distribution models are evaluated using the experimental

data in Chapter 5. The evaluation of the models using the data from the literature can be found in Appendix C. Based on the insights obtained in Chapter 4, a new phase distribution model is proposed. This new model is evaluated using the data of this work and the data from the literature.

In Chapter 6, conclusions are drawn and recommendations for future work are proposed.

2

Two-phase maldistribution in the literature

2.1 Introduction to two-phase flow

A two-phase flow is a flow where two phases coexist; this can for example be a liquid and a vapour phase. On the interface between the vapour and liquid phase different forces interact: surface tension, shear stress and gravitational forces. Due to the equilibrium of the different forces, different spatial distributions of the phases in a channel exist. These different spatial distributions of the phases are referred to as flow regimes. These flow regimes have an important influence on the pressure drop and the heat transfer.

This section first discusses several general two-phase flow parameters. Then it discusses the different flow regimes and finally it introduces a number of methods to determine the flow regime.

2.1.1 Two-phase flow parameters

Vapour quality The vapour quality x is defined as the fraction of the total mass flow rate $\dot{m}$ being in the vapour phase.

$$x = \frac{\dot{m}_g}{\dot{m}} \tag{2.1}$$

Mass flux The mass flux G $[\mathrm{kg}/(\mathrm{m}^2{\cdot}\mathrm{s})]$ is defined as the mass flow rate $\dot{m}$ divided by the inner cross-sectional area of the tube A_c. D is the inner tube diamater.

$$G = \frac{\dot{m}}{A_c} = \frac{\dot{m}}{\pi \left(\frac{D}{2}\right)^2} \tag{2.2}$$

Superficial velocities Both the superficial vapour velocity J_g and the superficial liquid velocity J_l are defined as the velocity of the phase as if it would be the only one flowing through the tube. In equations 2.3 and 2.4, ρ_g and ρ_g are respectively the density of the vapour phase and the liquid phase.

$$J_g = \frac{\dot{m}_g}{A_c\,\rho_g} = \frac{G\,x}{\rho_g} \tag{2.3}$$

$$J_l = \frac{\dot{m}_l}{A_c\,\rho_l} = \frac{G\,(1-x)}{\rho_l} \tag{2.4}$$

The doublet mass flux and vapour quality $(G; x)$ is equivalent to the duplet superficial vapour velocity and the superficial liquid velocity $(J_g; J_l)$.

Void fraction As illustrated in figure 2.1, different void fraction definitions exist in the literature: local, chordal, cross-sectional and volumetric void fraction [23]. In this work, only the cross-sectional void fraction ϵ will be used.

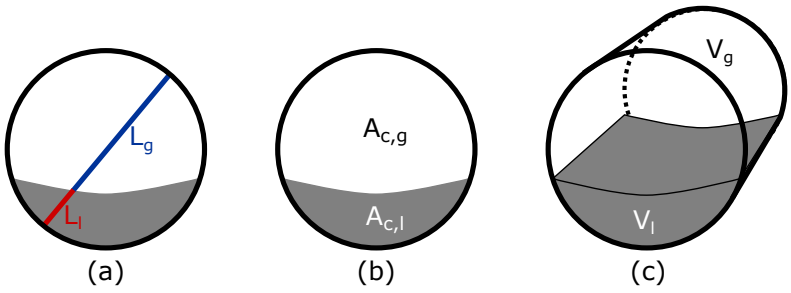

Figure 2.1: The different void fraction definitions: (a) chordal, (b) cross-sectional and (c) volumetric void fraction.

The cross-sectional void fraction ϵ, denoted as void fraction in this work, is defined as the ratio of the cross-sectional area occupied by vapour phase to the total cross-sectional area of the tube (see figure 2.1b).

$$\epsilon = \frac{A_{c,g}}{A_c} = \frac{A_{c,g}}{A_{c,g} + A_{c,l}} \tag{2.5}$$

Typically, the vapour quality x is not equal to the void fraction ϵ as a result of the difference in mean velocity between the two phases, referred to as slip, and the

difference in density. In the literature, several correlations exist for calculating the void fraction. A review of these different correlations was made by Wojtan [24]. The correlations can be classified into two groups: separated flow models and drift flux models. The separated flow model assumes that the two phases are flowing each at their own velocity v and separated from each other. Equation 2.6 forms the basis of the separated flow model. Different authors proposed expressions for the velocity ratio S also referred to as the slip ratio.

$$\epsilon = \frac{\frac{x}{\rho_g}}{\frac{x}{\rho_g} + S\frac{1-x}{\rho_l}} = \frac{\frac{x}{\rho_g}}{\frac{x}{\rho_g} + \frac{v_g}{v_l}\frac{1-x}{\rho_l}} \tag{2.6}$$

A special separated flow model is the homogeneous model with $S = 1$. The homogeneous model assumes both phases have the same velocity.

The separated flow models assume a discontinuity at the vapour-liquid interface which is not physical. The drift flux models were proposed to address this. The drift-flux model of Rouhani-Axelsson [25] is recommended by Steiner [26] for horizontal refrigerant flows. This model incorporates, in contrast to other drift-flux models, a dependency on the surface tension and the mass velocity. The drift-flux model of Rouhani-Axelsson [25] is given in equation 2.7 and will be used in this work.

$$\epsilon = \frac{x}{\rho_g}\left[\left(1 + 0.12\left(1-x\right)\right)\left(\frac{x}{\rho_g} + \frac{1-x}{\rho_l}\right) + \frac{1.18\left(1-x\right)\left(g\sigma\left(\rho_l - \rho_g\right)\right)^{0.25}}{G\sqrt{\rho_l}}\right]^{-1} \tag{2.7}$$

Momentum flux ratio The liquid momentum flux $\dot{M}_l$ and vapour momentum flux $\dot{M}_g$ are defined as:

$$\dot{M}_l = \rho_l\, v_l^2 \tag{2.8}$$

$$\dot{M}_g = \rho_g\, v_g^2 \tag{2.9}$$

The velocity v is the real velocity of the phase, not the superficial velocity J.

The momentum flux ratio is defined as the ratio of the vapour momentum flux to the liquid momentum flux.

$$\dot{M}_r = \frac{\dot{M}_g}{\dot{M}_l} \tag{2.10}$$

2.1.2 Flow regimes and flow regime maps

The two phases of a two-phase flow have multiple options to distribute themselves spatially. This spatial distribution of the two phases has a significant influence on the pressure drop and the local heat transfer. Several authors tried to recognise and classify the different flow regimes. This classification is often subjective, resulting in a different number of flow regimes: Wong and Yau [27] recognise 16 different flow regimes while Wojtan *et al*. [28] only recognise 8. In this work, the flow regimes proposed by Wojtan *et al.* [28] are used, as they are recognized by a large part of the scientific community. The definitions of the eight flow regimes by Wojtan *et al.* [28] are given below:

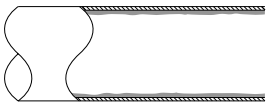

Annular (A) Around the perimeter of the tube a continuous liquid film exists. In the center there is a gas core which can contain some droplets. The liquid film is thicker at the bottom than at the top due to gravity.

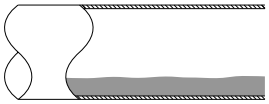

Stratified (S) There is a complete separation of the two phases. The gas at the top of the tube is separated by an undisturbed horizontal interface from the liquid at the bottom of the tube.

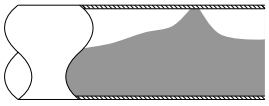

Slug (SL) Liquid slugs separate elongated bubbles which have diameters similar in size to the channel diameter.

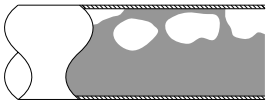

Intermittent (I) Large amplitude waves washing the top of the tube are alternated with smaller amplitude waves. The large amplitude waves can contain entrained gas bubbles.

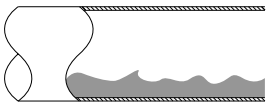

Stratified-Wavy (SW) The stratified-wavy flow is similar to the stratified flow but now the interface is not undisturbed. The interface between the two phases contains waves of which the crests do not reach the top of the tube.

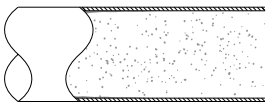

Dry-out (D) and Mist (M) The mist flow consists of very small liquid droplets entrained in a continuous gas phase. Further, the wall is dry during mist flow. Dry-out flow is the transition between annular flow and mist flow. Still some liquid is left on the tube walls but some sections are already dry. Due to the thinner liquid layer at the top of the tube, dry-out starts there.

To assign a certain flow regime to a flow, based on measurable properties, flow regime maps were developed. The most common type of a flow regime map uses the mass flux G and vapour quality x to determine the flow regime. Figure 2.2 shows an example of such a graph.

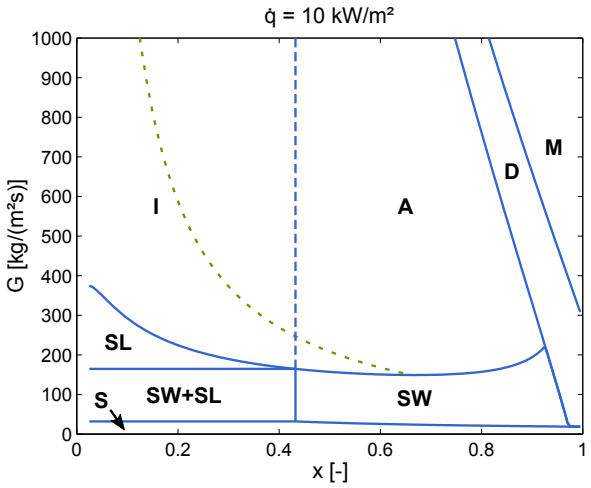

Figure 2.2: An example of a flow regime map of Wojtan et al. [28]. The blue lines are the transition lines. In the adapted version of Barbieri et al. *[29] the dashed blue line is replaced by the green dashed line.*

The blue lines indicate the transitions between the different flow regimes. Wojtan *et al.* [28] used subjective visual interpretation of the flow patterns to construct this flow regime map.

To mitigate the subjectivity of the human interpretation, Canière *et al.* [30] developed a probabilistic flow regime map using clustering techniques. The authors used a numerical clustering algorithm to classify measured time traces of the void fraction. An example of a probabilistic flow regime map is shown in figure 2.3 together with the flow regime map of Wojtan *et al.* [28]. As seen on figure 2.3, the transition between intermittent and annular flow is not predicted very well by the flow pattern map of Wojtan *et al.*. Hence, Barbieri *et al.* [29] proposed a new transition line which is drawn as a red dashed line in figure 2.3 and as a dashed green line in figure 2.2. In this work the flow regime map of Wojtan *et al.* [28] adapted to Barbieri *et al.* [29] will be used. This flow regime map was chosen due to its accuracy and its simplicity compared to the probabilistic flow regime maps.

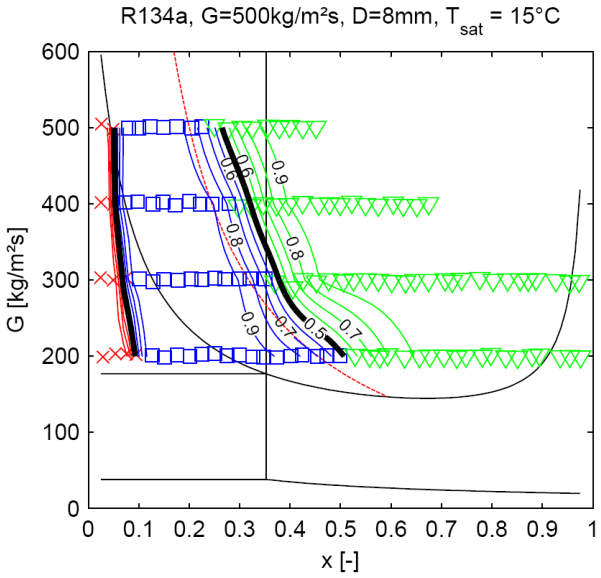

Figure 2.3: The probabilistic flow regime map of Canière et al. *[30] drawn together with the flow regime map of Wojtan et al. [28] (thin black lines). The red, blue and green symbols are measurements with respectively a slug, an intermittent and annular flow according to the model of Canière* et al. *[30].*

2.2 Impacting T-junction

T-junctions can be classified in two categories: impacting and branching T-junctions. For a branching T-junction one of the outlets branches off, whereas the other one is a continuation of the inlet. In contrast, an impacting T-junction has two outlets perpendicular to the inlet, see figure 2.4. This work will focus on the impacting T-junction.

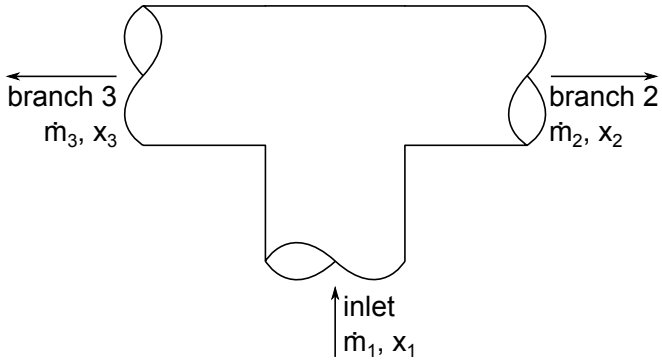

Figure 2.4: Schematic representation of an impacting T-junction.

The T-junction can have multiple orientations. Figure 2.5 displays the definitions used in this work for the different orientations. The inclination angle of outlet branch 2 with respect to the horizontal plane is given by θ. The inclination angle of the inlet with respect to the horizontal plane is given by ϕ.

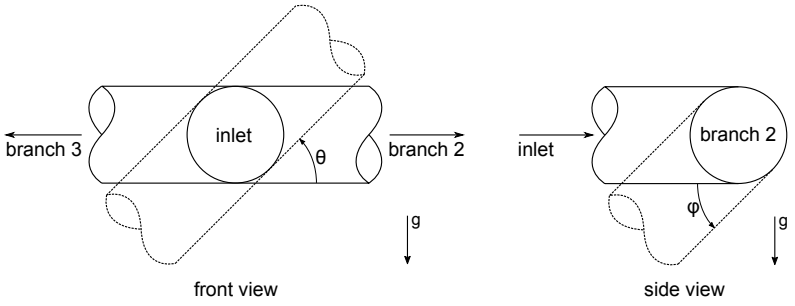

Figure 2.5: The different orientation angles of an impacting T-junction.

2.2.1 Representation of results

In the literature, the results of phase distribution experiments are often represented as the mass fraction of the vapour phase (F_g) that goes to one outlet as function of the fraction of the liquid phase (F_l) that goes to the same outlet.

$$F_l = \frac{\dot{m}_{l,2}}{\dot{m}_{l,1}} = \frac{\dot{m}_2\ (1 - x_2)}{\dot{m}_1\ (1 - x_1)} \tag{2.11}$$

$$F_g = \frac{\dot{m}_{g,2}}{\dot{m}_{g,1}} = \frac{\dot{m}_2\, x_2}{\dot{m}_1\, x_1} \tag{2.12}$$

A sample of this typical way of representing phase distribution data, the F_g – F_l-graph, can be seen in figure 2.6a. Sometimes another representation method is used in the literature which is given in figure 2.6b. Figure 2.6b represents the ratio of the inlet to the outlet vapour quality as function of the ratio of the inlet and outlet mass flow. Using this representation method, it is harder to compare the results of different experiments with each other. For this reason the representation of the results in this work will be done using the F_g – F_l-graph.

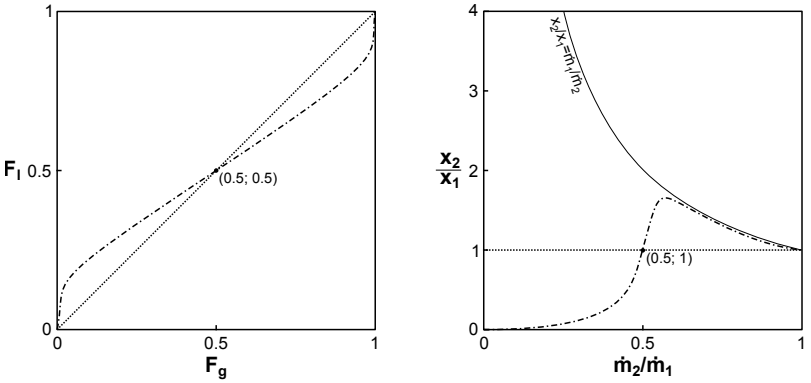

(a) F_g – F_l graph *(b) $\frac{\dot{m}_2}{\dot{m}_1}$ versus $\frac{x_2}{x_1}$ graph*

Figure 2.6: Different methods of representing phase distribution data (dotted line = even phase distribution).

In both figure 2.6a and 2.6b a dotted line is drawn which contains all the points where the two phases are distributed evenly. This means that the outlet vapour qualities x_2 and x_3 are equal to the inlet vapour quality x_1.

The dash-dotted line in figure 2.6a is an example of a phase distribution experiment represented in a F_g – F_l-graph. By changing the total mass fraction towards outlet 2 ($\frac{\dot{m}_2}{\dot{m}_1}$), you move along this line. By moving along the line to the lower left corner, the total mass fraction towards outlet 2 ($\frac{\dot{m}_2}{\dot{m}_1}$) decreases. This and

all other possible examples start in the point $(0; 0)$. At point $(0; 0)$, the total mass fraction towards outlet 2 ($\frac{\dot{m}_2}{\dot{m}_1}$) is 0, meaning that the total mass flow rate only goes through the outlet 3. Furthermore, the line in a $F_g - F_l$-graph should always end in $(1; 1)$. At point $(1; 1)$, the total mass fraction towards outlet 2 ($\frac{\dot{m}_2}{\dot{m}_1}$) is 1, meaning that the total mass flow rate passes through the outlet 2.

For the example shown here, the F_l-value is larger than the F_g-value in the lower left quadrant of the graph. This implies that more liquid, compared to a homogeneous flow, is flowing through outlet 2. In the upper right quadrant of the graph, the F_g-value is larger than the F_l-value, implying that more vapour, compared to a homogeneous flow, is flowing through outlet 2.

Furthermore, every line in a $F_g - F_l$-graph of a horizontal symmetric impacting T-junction is centrally symmetric. This can be be explained intuitively: if the T-junction is geometric symmetric, the flow will not notice a difference between the left and right outlet. It will only be affected by the boundary conditions at these outlets. Hence, if you swap the the right and left boundary conditions, the flows flowing through the two outlets will also be swapped.

Finally, due to the centrally symmetry, every $F_g - F_l$-line should pass through the center point $(0.5; 0.5)$.

Table 2.1: Overview of literature about two-phase distribution over an impacting T-junction

	ϕ [deg]	θ [deg]	Fluid	P_1 [MPa]	T_1 [°C]	D_{in} [mm]	D_{branch} [mm]	$J_{g,1}$ [m/s]	$J_{l,1}$ [m/s]	flowregime
Sun [31]	0	0	nitrogen-water	0.12	25	1x0.5	0.4x0.5, 0.6x0.5, 0.8x0.5	0.47 - 15.07	0.013 - 0.41	SL, A
Zheng [32]	0	90	R134a/R245fa, R290/R600a	/[a]	/[a]	8	17.5	/[a]	/[a]	SW, I, A
Zheng [33]	0	90	R134a	0.71 - 0.85	27 - 33	8	17.5	0.24 - 8.67	0.03 - 0.46	SL, SW, I, A
Zheng [34]	0	90	R134a/R245fa	/[a]	/[a]	8	17.5, 47.8	/[a]	/[a]	/[a]
Chen [35, 36]	0	0	nitrogen-water	0.11 - 0.12	18 - 22	0.5x0.5	0.5x0.5	0.36 - 30	0.018 - 0.9	SL, A
Mohamed [37]	0	0	air-water	0.15, 0.2	ambient	13.5; 37.8	13.5; 37.8	2 - 40	0.01 - 0.18	S, W, A
Bertani [38]	0	0	air-water	0.24	ambient	10	10	0 - 35	0 - 3.5	B, I, A
Tuo [12, 39]	0 - 45	90	R134a, R410a	/[a]	/[a]	8.7	13.4, 18.3	0.26 - 5.46[b]	0.098 - 0.5[b]	S, SW, I
Elazhary[d] [40, 41]	0	0	air-water	0.2	ambient	1.87x20	1.87x20	0.04 - 10	0.02 - 0.7	B, I, A
Mohamed [42, 43]	0	0 - 90	air-water	0.2	ambient	13.5	13.5	2 - 40	0.01 - 0.18	S, W, A
Milosevic [44]	0	90	R134a	0.7 - 1	25 - 40	8.7, 12	18.3, 23.8	0.24 - 2.25	0.10 - 0.40	S, A
Doherty[d] [45]	0	0	air-water	/[a]	/[a]	26	26	0.5 - 25	0.008 - 0.8	S, W, A
Murphy[d] [46]	0	0	air-water	ambient	ambient	45.4	45.4	0.15 - 30	0.05 - 1.02	S, SL, I, A
El-Shaboury [47]	0	0	air-water	0.15	ambient	37.8	37.8	0.5 - 40	0.0026 - 0.18	S, W, A
Wang [48]	90	0	air-water	ambient	ambient	15	15	0.09 - 7.08	0.09 - 0.19	I
Tshuva [49]	0	0 - 90	air-water	ambient	ambient	24	24	0.15 - 5.6	0.02 - 3.03	SL
Hatziavramidis[c] [50]	0	0	air-water	0.13 - 0.19	ambient	38	38	1.33 - 5.34	1.35 - 2.7	S, B
Fuiji [51]	0	0	air-water	/[a]	/[a]	10	10	0.03 - 12	0.05 - 0.5	SW, I, A
Ottens [52]	0	0	air-water	ambient	ambient	29.5	29.5	15.8	0.000 63 - 0.03	/[a]
Hong [53]	0	0	water	/[a]	/[a]	50.8, 101.6	50.8, 101.6	1.5 - 21.3	0.015 - 2.1	/[a]
Hong [53]	0	0	air-water	ambient	ambient	19	19	4.6 - 22.86	0.045 - 1.35	S, A
Chien [54]	0	0	water	2.86 - 4.24	231 - 253	49.2	49.2	12.2 - 33.5	0.082 - 1.74	/[a]
Lightstone[d] [55]	0	0	air-water	ambient	ambient	20	20	0.1 - 2.65	0.01 - 0.18	S, B, SW, SL, A
Hwang [56]	0	0	air-water	0.13 - 0.19	ambient	38	38	1.33 - 5.34	1.35 - 2.7	S, B
Azzopardi [57, 58]	90	0	air-water	0.17	ambient	31.8	31.8	1.6 - 35.3	0.042 - 0.80	I, A

[a] Missing data; [b] Assumed saturation temperature of 25 °C; [c] Simulations; [d] Only pressure drop and flowpattern measurements

2.3 Existing research on impacting T-junctions

Early on it was assumed that due to the symmetry of an impacting T-junction, the liquid and vapour phase would distribute evenly over the two outlets. However, in the first applications it was discovered that this assumption was not correct. This led to research into the flow behaviour of liquid-vapour flows. Table 2.1 summarises all the literature known to the author on the distribution of two-phase flows over impacting T-junctions.

Based on table 2.1, it is clear that most research is done on water-air mixtures. Research with fluids at vapour-liquid equilibrium, like steam and refrigerants, is very scarce. One goal of this work is to fill in this gap with new experimental data.

First of all, the literature can be divided in two groups: horizontal and inclined T-junctions. The authors which investigated the inclined T-junctions were mainly interested in the capacity of the T-junction of being a phase separator. Most of them did not investigate how the phases are distributed but limited their research to the occurrence of full separation. The following section will first discuss the different influences on the phase distribution over horizontal impacting T-junctions found in the literature. The second section will discuss the inclined impacting T-junctions.

2.3.1 Horizontal impacting T-junctions

First of all, all authors confirm that the phases are only distributed evenly over the branches of an horizontal impacting T-junction when the total mass flow rate is split evenly over its branches. This is a logical result of geometrical symmetry. Generally, in all other cases, maldistribution of the two phases will occur. Further, in the literature the influences of inlet superficial velocities, channel diameter, fluid properties, flow regimes and pressure drop on the phase distribution were investigated. The next subsections will discuss them in more detail.

2.3.1.1 Influence of the inlet superficial velocities on the phase distribution

Almost every author in the literature investigated the influence of the inlet superficial velocities or their equivalent duplet of mass flux G and vapour quality x. Azzopardi *et al.* [57] were the first authors to investigate the influence of the inlet superficial velocities. Compared to all the later research, they did not see any significant effect due to the inlet superficial velocities. Either their results contain an error, or it is due to their limited test range. Furthermore, it is the only research with a vertical inlet. The flow regimes occurring in a vertical tube are different from the ones occurring in a horizontal tube. Therefore, the inlet flow regimes observed in the work of Azzopardi *et al.* [57] will be different, which could also explain the difference in results.

If the inlet superficial vapour velocity increases while the superficial liquid velocity is fixed, the F_g-F_l curve rotates around its centre point in anti-clockwise direction. When the inlet superficial vapour velocity is fixed, the F_g-F_l curve rotates in clockwise direction with increasing superficial liquid velocity. So in other words, the liquid phase has an increasing preference flowing to the branch with the lowest mass flow rate with decreasing inlet superficial vapour velocity and vice versa.

The trends above can be translated to the effects of mass flux and inlet vapour quality. For a fixed mass flux, the F_g-F_l curve rotates counter-clockwise with increasing vapour quality [42].

Both El-Shaboury *et al.* [47] and Elazhary *et al.* [40, 41] found that if there is a transition to another flow regime, there is an inconsistency in the above trends. Within one flow regime the trend seems to remain valid. Due to a limited amount of data points around flow regime transition, no conclusion could be made and further research is needed.

Furthermore, El-Shaboury *et al.* [47] found an inlet condition that gives an even split over the whole range. There is no maldistribution when the inlet flow has respectively a superficial vapour and superficial liquid velocity of $10\,\mathrm{m/s}$ and $0.01\,\mathrm{m/s}$ (data set W1 in figure 2.7).

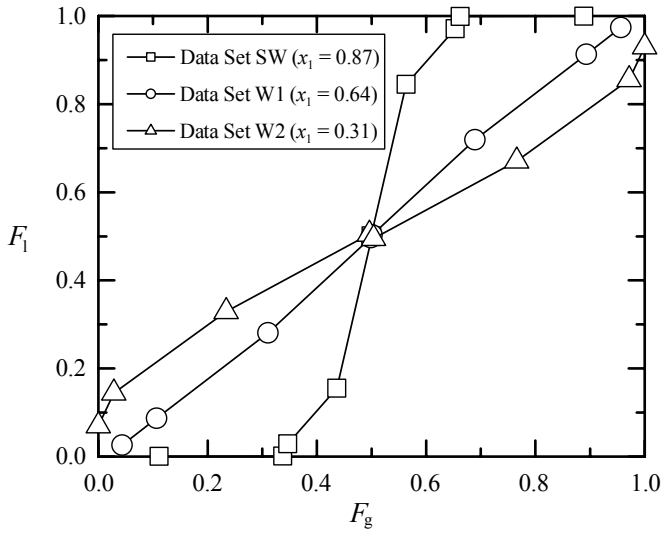

Figure 2.7: Phase distribution data of El-Shaboury et al. *[47] for the wavy and stratified-wavy flow regimes.*

Elazhary *et al.* [40] and Chen *et al.* [35, 36] both tested microchannel T-junctions. According to Serizawa *et al.* [59], a tube is classified as a microtube when the channel diameter d is smaller than $\lambda/3.3$, where λ is the Laplace constant

($\lambda = \sqrt{\sigma / (g\,(\rho_l - \rho_g))}$), defined by Suo and Griffith [60]. Elazhary *et al.* [40] and Chen *et al.* [35, 36] noticed that the effect of inlet superficial velocities is less pronounced than for macrochannel T-junctions. Instead of gravity and inertia, the viscous and surface tension force are the dominant forces in microchannels. Hence, a change in inertial forces will have less effect on the phase distribution.

The ratios of forces are often represented as dimensionless numbers. The inertial force over the surface tension force is given by the Weber number:

$$We = \frac{\rho\, v^2\, D}{\sigma} \tag{2.13}$$

σ is the surface tension. The inertial force over the viscous force is given by the Reynolds number:

$$Re = \frac{v\, \rho\, D}{\mu} \tag{2.14}$$

The dynamic viscosity is denoted by μ and D is the hydraulic diameter of the channel.

2.3.1.2 Influence of channel diameter on phase distribution

Few authors [31, 35, 37] investigated the influence of the channel diameter on the phase distribution.

Mohamed *et al.* [37] compared his data (D = $13.5\,\mathrm{mm}$) with the data of El-Shaboury *et al.* [47] (D = $37.8\,\mathrm{mm}$). The authors noticed only a very small effect due to the diameter change. Furthermore, the magnitude of this effect decreases with increasing inlet superficial velocities. At higher inlet superficial velocities, the inertial forces and the accompanying momentum will be more dominant due to the quadratic dependence on the velocity.

Both Sun *et al.* [31] and Chen *et al.* [35, 36] investigated the effect of the branch diameter on the phase distribution for microchannels. The phenomena occurring in microchannels are fundamentally different from the ones in macrochannnels. The dominant phenomena in macrochannels are gravity and inertia, whereas in microchannels the viscous and surface tensions force become more important. In general, the maldistribution is less severe for microchannels than for macrochannels. For both a slug and an annular flow in a micro-channel, the liquid has an increasing tendency to go to the channel with the smallest mass flow rate for an increasing channel diameter. In both cases the degree of maldistribution decreased with decreasing diameter. Furthermore, if the superficial velocities increase, the effect of the diameter is reduced. This was also found for macrochannels.

2.3.1.3 Influence of fluid properties on phase distribution

The available literature that investigated the effect of the fluid properties on the phase distribution is rather scarce. Most authors investigate the fluid properties indirectly by varying parameters such as the pressure or the fluid itself.

Chien and Rubel [54] investigated the effect of the steam pressure on the phase distribution. A change in saturation pressure affects mainly the density ratio between vapour and liquid. However, the authors did not see a significant effect. Mohamed *et al.* [37] investigated the effect of pressure on the phase distribution but for a water-air mixture. They observed a strong effect for low inlet velocities but this effect decreased for an increasing inlet velocity. The preference of the liquid phase to exit through the branch with the lowest mass flow rate decreases, with increasing pressure (= increasing mass density ratio ρ_g/ρ_l) if both inlet superficial velocities remain the same.

Hong *et al.* [53] compared their water-air experiments with their steam experiments. The trends observed are the same but especially at lower vapour qualities there was a larger difference in absolute values.

Chen *et al.* [36, 36] investigated the effects of viscosity and surface tension on the phase distribution. Note that the T-junction used in the work of Chen *et al.* is made of micro-channels. The effects for viscosity and surface tension will probably be much smaller in macro-channels according to the authors. In macro channels; the gravitational and inertial force are two to three orders of magnitude larger than the viscous forces and the surface tension. Due to the larger surface tension forces in micro-channels, the liquid sticks to the wall. Hence, annular flow is very common. For an annular flow, the preference of the liquid phase to exit through the branch with the lowest mass flow rate increases with decreasing surface tension. This means that the maldistribution gets worse. However, for a slug flow with a slug length smaller than 5 times the channel diameter, the opposite effect is noticed. According to the authors, the surface tension does decrease the liquid kinetic energy which makes the liquid divide more evenly. Due to the higher surface tension, the liquid flows along the wall which slows down the liquid flow by viscous drag. The trend for the slug flow was explained by the fact that a gas slug can break up easier to divide over the two branches when the surface tension is lower. For the annular flow, the authors also investigated the effect of viscosity on the phase distribution. The authors observed a minor effect of the liquid viscosity, which has a similar effect as the inlet liquid superficial velocity. The velocity of the liquid film decreases with increasing liquid viscosity.

2.3.1.4 Flow regime maps for impacting T-junctions

Several authors [34,38,41,42,45,46,55] compared the observed flow regimes in the inlet tube with an existing flow regime map of a regular straight tube. In general,

the existing flow regime maps match very well with the observed flow regimes. However, Zheng *et al.* [34] noticed that the intermittent to annular transitions of the map of Wojtan *et al.* [28] do not fit the observed values, especially at higher mass fluxes. As mentioned in section 2.1.2, the flow regime map of Wojtan *et al.* [28] does not capture the intermittent to annular transition for the data of straight observations either. Furthermore, Lightstone *et al.* [55] observed a faster transition from stratified-smooth to stratified-wavy. Lightstone *et al.* [55] and Doherty *et al.* [45] also noticed a decrease in void fraction just before the junction for stratified flows, as e.g. the liquid level increases. According to the authors, this can be attributed to both a flow regime change and a fluid deceleration over the T-junction.

Murphy *et al.* [46] and Doherty *et al.* [45] investigated the flow regimes in the two outlets, as well as the flow regime in the inlet. Both studies compared the flow regime map for a straight tube with their observations. They noticed that most transitions occur sooner due to the sudden change in pressure over the T-junction. Only for the transition from stratified to stratified-wavy the opposite was noticed. The flow in the outlet remained much longer stratified-smooth than in a normal straight tube. The authors did not give any explanation for this.

2.3.1.5 Pressure drop over an impacting T-junction

The first authors investigating the pressure drop over an impacting T-junction were Lightstone *et al.* [55]. The pressure drop over an impacting T-junction is measured by extrapolating pressure measurements up- and downstream of the junction as seen in figure 2.8. This extrapolation method will be explained in more detail in paragraph 4.3.

Lightstone *et al.* [55] modelled the pressure drop over an impacting T-junction as a sudden expansion of the tube. Besides the irreversible losses due to sudden expansion, they accounted for additional losses due to the turning of the flow.

Later, Wang *et al.* [48] studied the temporal behaviour of the pressure drop over an impacting T-junction. They noticed an increased fluctuation of the pressure drop with increasing inlet superficial velocities and with increasing mass split ratio ($\dot{m}_2/\dot{m}_1$). The pressure drop also increases with increasing inlet superficial velocities as found by many authors [45, 47, 48].

Finally, El-Shaboury *et al.* [47] measured the pressure gradient over an impacting T-junction. The authors noticed a strong effect of the flow regime on the pressure drop as you can see in figure 2.8. Doherty *et al.* [45] also noticed this dependency. Stratified flows had a smaller pressure drop than the other flow regimes. Furthermore, the zone of influence of the pressure gradient at the inlet is longer compared to the other regimes as can be seen in figure 2.8b. This is related to the increasing liquid level at the inlet for a stratified flow. Murphy *et al.* [46] even saw a pressure rise for a stratified flow instead of a pressure drop.

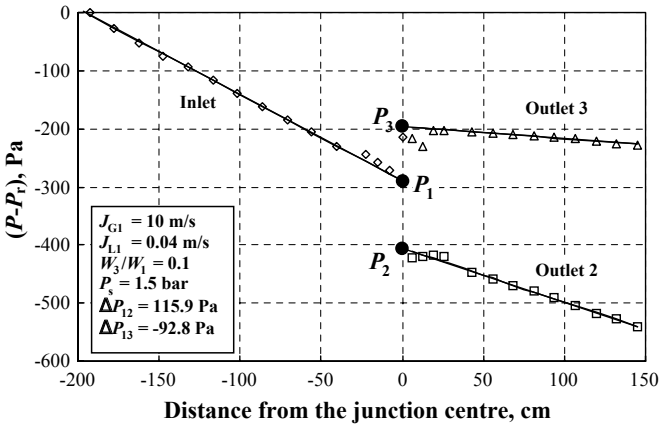

(a) Wavy flow

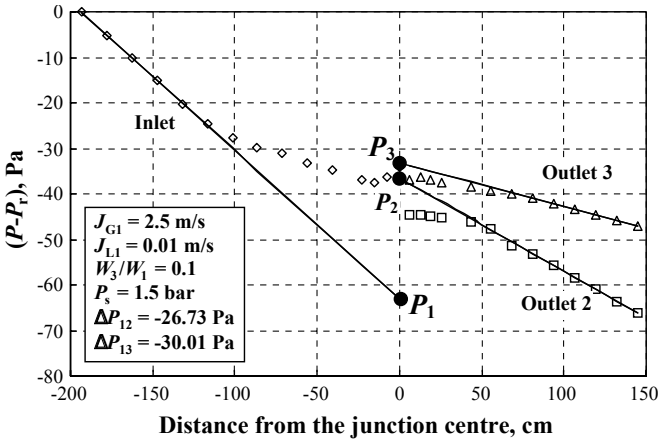

(b) Stratified flow

Figure 2.8: The pressure distribution over an impacting T-junction [47].

2.3.2 Inclined impacting T-junctions

Mohamed *et al.* [42, 43] studied the influence of branch inclination on the phase distribution. According to the authors, there is a strong dependence between the phase distribution and the inclination angle of the branches for stratified flows. Figure 2.9a shows the result of one of their stratified experiments. With increasing inclination angle, the curve shifts towards the upper left corner. In this case when the branch is facing downward with an angle of $0.7°$ or more, all the liquid will flow to this branch.

Figure 2.9b shows the results for a wavy flow. Clearly, a wavy flow is less sensitive to branch inclination than a stratified flow. For this case there is full

separation of the two phases for an inclination angle of $87.5°$. However, for another wavy experiment, there was even no full separation at an angle of $90°$.

Finally, figure 2.9c shows the results for an annular flow. Here, the effect of branch inclination is really small. Even for large inclination angles, the curves are just shifted a bit towards the upper left corner.

Mohamed *et al.* [42, 43] explains the results as follows. In macro channels, the two main forces acting are gravity and inertia. For a stratified flow, the inertial forces are rather low, for this reason this flow regime is more susceptible to the gravitational force.

Mohamed *et al.* [42, 43] also made a correlation to predict the limiting inlet conditions where full separation can occur at a certain inclination angle of the branches.

Both Milosevic [44] and Tuo *et al.* [12, 39] applied the T-junction as a phase separator. In this case, the branches should be oriented vertically to maximise the separating effect of gravity. They limited their research to the separation efficiency of impacting T-junctions. They did not test the phase distribution over the whole range of mass split ratios.

In general, the separation efficiency of the vertical T-junction decreases with increasing mass flux or quality. In both cases, the liquid inertial force and vapour phase drag force become dominant over gravity. First of all, the higher liquid inertial force increases the energy of the liquid to go up against gravity. Normally, after impact with the junction, the inertial force would promote equal split. Also, due to the higher liquid velocity, the liquid layer will more likely break up in small droplets when impacting on the T-junction. When the vapour phase drag force is high, these droplets can be easily transported upwards in the upward branch. At low vapour velocities, the gravity is strong enough to separate the liquid drops. This explains why this T-junction has a good phase separation efficiency for a stratified flow.

Zheng *et al.* [32] compared experimentally the phase distribution of pure refrigerants with the one of zeotropic refrigerant mixtures. The zeotropic mixtures show less separation in a vertical T-junction than pure refrigerants. This trend does not fit logic reasoning because the separation efficiency should lower with decreasing density ratio according to the horizontal measurements.

Tuo *et al.* [12] investigated the influence of the tube diameter on the phase separation efficiency. It is beneficial for separation to increase the tube diameter of the branches. A larger branch tube reduces the impact on the junction's wall which limits the creation of liquid droplets which can be easily carried to the top outlet as explained before. Moreover, a larger diameter also reduces the velocities in the branches, reducing the inertial force and the vapour phase drag force compared to the gravitational force.

Besides the effect of branch diameter, Tuo *et al.* [12] also noticed that if the

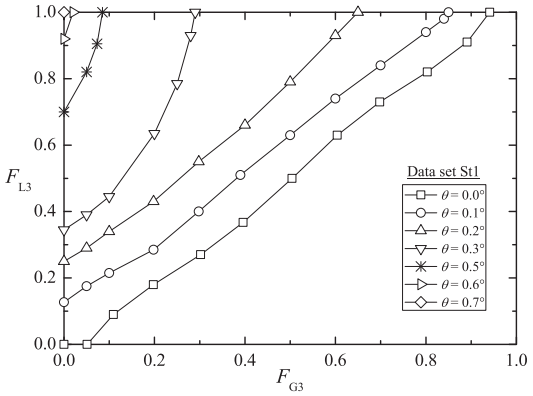

(a) $J_g = 2\,\mathrm{m/s} | J_l = 0.01\,\mathrm{m/s}$

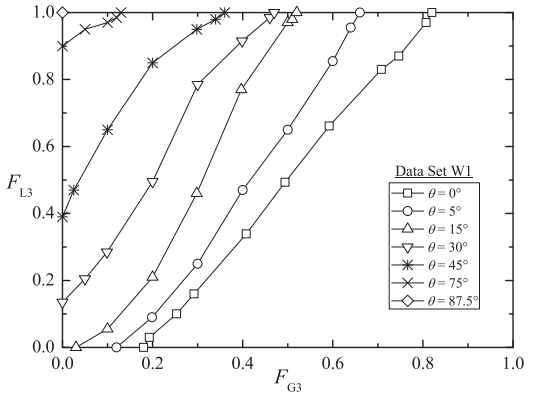

(b) $J_g = 10\,\mathrm{m/s} | J_l = 0.01\,\mathrm{m/s}$

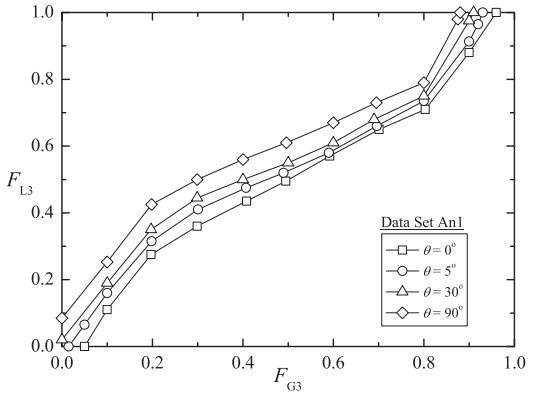

(c) $J_g = 40\,\mathrm{m/s} | J_l = 0.01\,\mathrm{m/s}$

Figure 2.9: $F_g - F_l$ graphs of water-air (23 °C — 150 kPa) phase distribution experiments [42], the experiments were conducted at different inlet conditions and at different branch inclination angles.

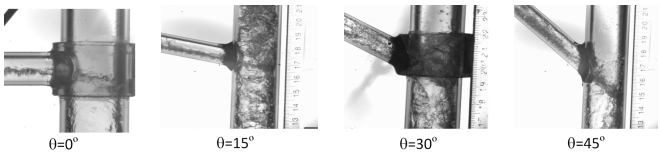

Figure 2.10: Flow separation at varied angles of inclination for in $\dot{m} = 30\,\mathrm{g/s}$ *and* $x = 15\,\%$ *[12].*

inlet is facing downward (see figure 2.10), the phase separation is improved up to a certain optimal angle. Due to the downward facing inlet, the impact on the branch wall is smaller, reducing the break up of the liquid flow in small droplets. Hence, enhancing the phase separation as explained above.

In 2014, Tuo *et al.* [39] compared his experimental data of R134a with that of R410a and observed only a very small difference in phase separation efficiency. The authors explained this by stating that both refrigerants have similar thermophysical properties.

Tuo *et al.* [12] compared the observed flow regimes with flow regime maps. Because their T-junction is installed directly after an expansion valve, their flow is not fully developed. Hence, the authors used a flow regime map for developing flows and observed a good compliance with their experimental observations.

Finally, Tuo *et al.* [39] proposed correlations which can be used to design an impacting T-junction separator. They noticed a strong drop in phase separation efficiency when churn flow instead of mist flow occurs in the top branch. Hence, a correlation which predicts the transition from mist to churn flow in the top branch was proposed. A churn flow only occurs in vertical tubes and is characterised by a very thick and unstable liquid film. This liquid film often oscillates up and down. Further, the liquid level in the bottom branch should be large enough to function as a barrier against bubble entrainment. Therefore, a correlation was proposed which predicts the bubble penetration depth in the bottom branch. This bubble penetration depth should be smaller than the liquid level to have a good separator.

2.3.3 Models available in the literature

Several authors tried to construct a model to predict the phase distribution in an impacting T-junction. Azzopardi *et al.* [57, 58] made the first model based on simple geometrical assumptions. They assume a fictitious barrier in the inlet tube which divides the tube in two areas, which are related to the mass flow division. Specifically, it is assumed that everything to the right of this boundary goes in the right branch. The authors only verified with their own data which was limited in range and only contained two flow regimes (churn and annular). Further, the T-junction used had a vertical inlet which is different from the subsequent models.

However, according to the authors, their model should also be valid for horizontal inlets.

The model of Hwang *et al.* [56] is based on the dividing stream concept. The idea is similar to the model of Azzopardi *et al.* [57, 58]. Based on the force equilibrium, a streamline for the liquid and vapour phase, respectively, is determined of which the end is perpendicular to the impacting T-junctions wall. All the liquid to the right of the liquid streamline, considering the spatial distribution of the phases, will exit through the right branch. Analogously, all the vapour to the right of the vapour streamline, will exit through the right branch. This model was verified with the data of Azzopardi *et al.* [57, 58] and their own data. Furthermore, this model takes the inlet flow regime (stratified and annular) into consideration. However, this model is difficult to extend to geometries with more than two outlets.

Ottens *et al.* [52] made the double stream model which uses a steady state macroscopic mechanical energy balance for both phases. His model is very sensitive to the energy loss coefficient of the junction, which is determined experimentally. This model was validated against their data of stratified-wavy air-water flow.

El-Shaboury *et al.*'s [47] model starts from the basic laws of mass, momentum and energy conservation of both phases, for a control volume which consists of the zone between the three branches. To be able to solve the set of equations, the author needs the deviation of the inlet flow and the friction force on the T-junction's wall. Both parameters are lumped in one parameter, for which a flow regime based empirical equation was fitted using the experimental data. This model is the most versatile one. Because it starts from the physical conservation laws, it can be easily adapted to other geometries and orientations. The model constructed in chapter 5 is based on this one.

Finally, several authors [33, 36, 53, 54] made empirical models which were fitted to their own data. These models are restricted to the flow regime for which the fit was made.

In 2014, Mohamed *et al.* [37] compared the models of El-Shaboury *et al.* [47], Hwang *et al.* [56] and Ottens *et al.* [52] with their experimental data. Both the model of Hwang *et al.* [56] and Ottens *et al.* [52] did not capture the influence of pressure on the phase distribution. The model of El-Shaboury *et al.* [47] under-predicted the effect for stratified flows but predicted rather well for the other flow regimes. The authors also investigated the sensitivity to channel diameter in the models. Here, only the model of Hwang *et al.* [56] could predict the influence of the channel diameter.

Finally, Chen *et al.* [35] noted that Azzopardi *et al.*'s [57, 58] model lacks a term to correct for a changing surface tension.

2.4 Impacting Y-junction

The literature for impacting Y-junctions is limited to the work of Murphy *et al.* [46] and Nagai *et al.* [61].

Murphy *et al.* [46] reported on the pressure drop of and the flow regimes in water-air two-phase flows through an impacting Y-junction (D_{in} = $0.0454\,\mathrm{m}$) with opening angles of $60°$, $90°$ and $120°$. For small opening angles the pressure loss is minimal and insensitive to the inlet flow rate. At the lowest flow rates, the authors reported a pressure gain due to the increase in flow area and the separation and reformation of liquid from the inlet to the outlet pipes. The flow regimes seen in the inlet branch comply with the flow pattern map for straight tubes. In contrast, the flow regimes in the outlet branches transition faster to higher turbulent flow patterns.

Nagai *et al.* [61] analysed the pressure loss, gas phase velocity and the void fraction in the branches of an impacting Y-junction of an air-water mixture. The T-junction has an opening angle of $60°$ and lies in the horizontal plane. The inlet tube is a rectangular tube of $2.5\,\mathrm{mm}$ by $4.6\,\mathrm{mm}$ and the outlet branches are rectangular tubes of $2.5\,\mathrm{mm}$ by $2.36\,\mathrm{mm}$. The authors found an irreversible pressure loss-coefficient of 0.3 independent of the inlet conditions. Additionally, a correlation was made to predict the gas phase velocity and the void fraction.

2.5 Conclusion

Generally, there is a consensus in the literature on the influence of the inlet superficial velocities on the phase distribution over an impacting T-junction. They all agree that the liquid phase has an increasing preference flowing to the branch with the lowest mass flow rate with decreasing inlet superficial vapour velocity and vice versa. However, El-Shaboury *et al.* [47] and Elazhary *et al.* [40, 41] found an inconsistency in the trends when there is a transition to another flow regime. This inconsistency is not yet well understood. Hence, chapter 4 will investigate the influence of inlet superficial velocities in the vicinity of flow regime transitions.

The available literature that studied the influence of fluid properties on phase distribution is rather limited. Furthermore, the most elaborated studies were conducted on micro-channel T-junctions. The physics occurring in micro-channels are significantly different. Hence, the influence of the fluid properties will be investigated in chapter 4.

The literature that investigated the influence of the inclination angle on the phase distributions focused on inclination angles where full separation of the phases occurs. These inclination angles are generally large. Most data is also limited to one fluid. In chapter 4 the influence of smaller inclination angles on the phase distribution and their combined influence with fluid properties will be studied. To summarize, all the influences studied experimentally in the literature are summarised in table 2.2.

$J_g \uparrow$	$F_g - F_l$-graph rotates counter-clockwise[a]
$J_l \uparrow$	$F_g - F_l$-graph rotates clockwise[a]
$D \downarrow$	maldistribution decreases[b]
$P \uparrow$	$F_g - F_l$-graph rotates counter-clockwise[b]
$\frac{\rho_g}{\rho_l} \uparrow$	$F_g - F_l$-graph rotates counter-clockwise
$\sigma \downarrow$	A: $F_g - F_l$-graph rotates clockwise[c]
	SL: $F_g - F_l$-graph rotates counter-clockwise[c]
$\theta \uparrow$	$F_g - F_l$-graph shifts towards the upper left corner for the down-facing outlet

[a] Influence smaller for microchannels; [b] Influence decreases with increasing inlet superficial velocities; [c] Only microchannel data available

Table 2.2: Summary of the influences studied in the literature.

Finally, Mohamed *et al.* [37] tested some of the phase distribution models available in the literature and concluded that most of them do not capture all the physics. For example, most models did not account for the interfacial mass transfer or the influence of fluid properties. This work will address this by proposing a new phase distribution model in chapter 5.

3
Experimental setup

This chapter describes the experimental setup used for this work. The experimental setup consists of two main parts: a two-phase flow conditioner and a test section. The original two-phase flow conditioner was designed and built during the PhD research of Canière [22] and further used in the PhD research of De Kerpel [21]. During this work, the flow conditioner was refurbished and a new test section was built. The first section will discuss the two-phase flow conditioner, the second section will describe the new test section and finally the last section will specify the test methodology.

3.1 Two-phase flow conditioner

This part of the experimental setup, called the two-phase flow conditioner, produces a refrigerant flow with a certain mass flux, vapour quality and saturation temperature. This conditioned refrigerant flow is then fed to the test section.

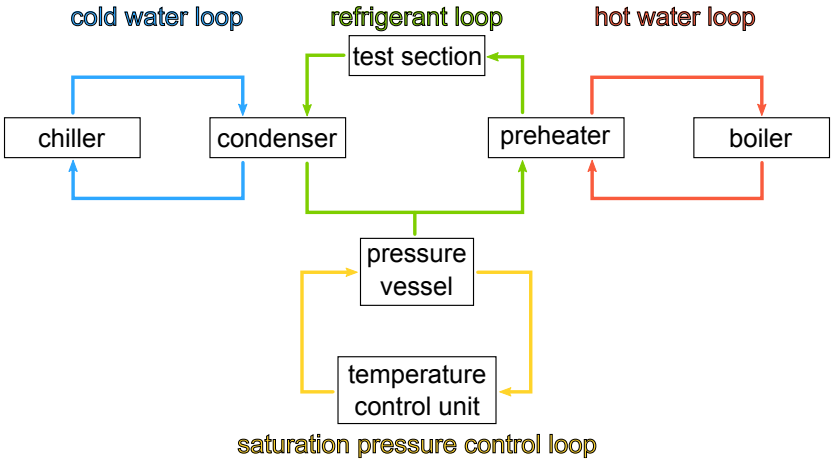

Figure 3.1: Schematic overview of the two-phase flow conditioner. The conditioner consists of 4 main loops: a refrigerant loop, a cold water loop, a hot water loop and a saturation pressure control loop.

This two-phase flow conditioner consists of 4 loops as shown in figure 3.1: a refrigerant loop, a cold water loop, a hot water loop and a saturation pressure control loop. In the following subsections, each loop will be discussed in detail to understand its working principle. The specifications of each component are not given here but are tabulated in appendix A. The appendix also contains the piping and instrumentation diagrams.

3.1.1 Refrigerant loop

Figure 3.2 displays the refrigerant loop. The refrigerant loop is completely made of standard $^3/_8\,\mathrm{inch}$ copper refrigerant tubing. First, the liquid refrigerant is pumped from the condenser to the preheater. The magnetically driven gear pump (Micropump GC M25) compensates for the pressure drop in the whole circuit. A magnetically driven pump is chosen to avoid the presence of oil in the refrigerant, which can significantly affect the results of the experiments [62]. This pump is also frequency-controlled in order to maintain the required mass flux. After the pump, the sub-cooled liquid refrigerant passes through a Coriolis-type mass flow meter (Bronkhorst cori-flow M55[1]), which is used to measure the mass flow rate.

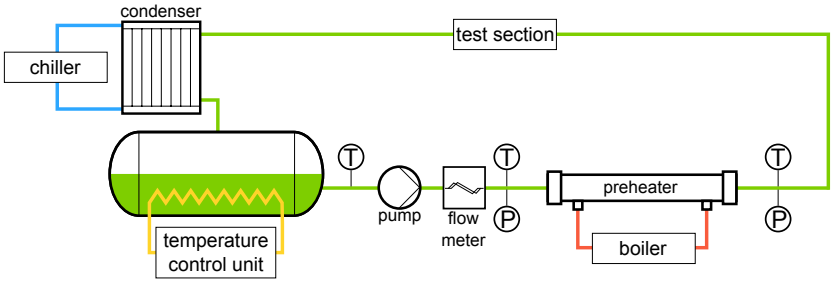

Figure 3.2: Schematic overview of the refrigerant loop. The liquid refrigerant is pumped out the buffer vessel through a mass flow meter, a preheater, a test section and a condensor.

The liquid refrigerant then enters the preheater which is a tube-in-tube heat exchanger. This preheater is heated with the hot water from the hot water loop which will be discussed later on. By controlling the heat exchanged in the evaporator, the vapour quality of the refrigerant flow can be set. The pressure and temperature of the refrigerant is measured just before and after the preheater. If in addition the heat transferred in the preheater is known, the vapour quality at the outlet of the preheater can be calculated by applying the first law of thermodynamics. More details on the calculation method and its accompanying uncertainty analysis can be found in appendix A.

The conditioned refrigerant flow then enters the test section. Finally, after the test section, the refrigerant flow is condensed in a plate heat exchanger. This condenser is cooled by the cold water loop which will be discussed in the following subsection.

[1] More information can be found in appendix A.

3.1.2 Cold water loop

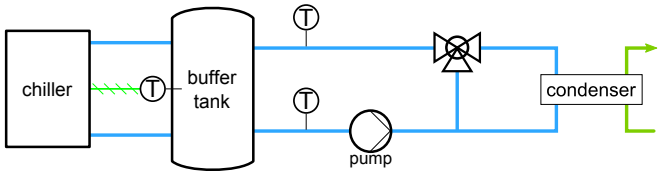

Figure 3.3: Schematic overview of the cold water loop. A chiller provides a chilled water-glycol mixture for the condenser in the refrigerant loop.

The cold water loop is illustrated in figure 3.3. A chiller (Daikin EUWAP16KAZW1[2]) provides a chilled water-glycol mixture (30 vol% of glycol) to a buffer tank of 900 litre. The chiller adjusts the temperature of this buffer tank to a set temperature. A fixed-speed centrifugal pump is used to pump the water-glycol mixture through the condenser. The flow rate through the condenser is controlled by a three-way valve (Danfoss VRB3) in order to control the sub-cooling of the refrigerant entering the buffer vessel.

3.1.3 Hot water loop

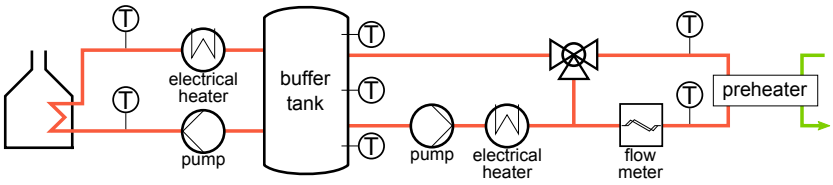

Figure 3.4: Schematic overview of the hot water loop. The hot water loop provides hot water for the preheater in the refrigerant loop.

A schematic of the hot water loop is shown in figure 3.4. A gas boiler of 55 kW is used to produce hot water which is stored in an insulated buffer tank of 2000 litre. The temperature of the water in the buffer tank is monitored by three K-type thermocouples. During the measurements, the gas boiler is switched off to avoid temperature oscillations. To minimise the temperature decrease of the water in the buffer tank during the experiments, a PID-controlled electrical heater (3 kW) is placed inline with the fixed-speed pump. This pump is used to pump the hot water through the preheater which evaporates the refrigerant to a set vapour quality.

The preheater consists of 6 tube-in-tube heat exchangers connected in series. Each tube-in-tube heat exchanger is a counterflow single pass heat exchanger. The

[2] temperature range: −10 °C – 20 °C; nominal power: 37 kW

inner tube is a $^3/_8$ inch copper tube (D_i = 8 mm; D_o = 9.5 mm) and the outer tube is a copper tube (D_i = 20 mm; D_o = 22 mm). The hot water flows through the annulus of the tube-in-tube heat exchanger.

To achieve a good control of the heat transferred in the preheater, it is possible to bypass one or more heat exchangers. This allows the total heat exchanger length to vary between 1 m and 15 m in steps of 1 m. Furthermore, the flow rate of the hot water through the preheater is regulated using a three-way valve (Danfoss VRB3). The water flow rate is measured using a coriolis-type flow meter (Bronkhorst cori-flow M55[3]). Further, at the in- and outlet of each tube-in-tube heat exchanger, the temperature is measured using a K-type thermocouple. By applying the first law of thermodynamics, the heat transferred in the preheater can then be calculated. More details on the calculation method and its accompanying uncertainty analysis can be found in appendix A.

Based on the uncertainty analysis, a large temperature difference and lower flow rate are preferable to have an accurate measurement of the heat transferred. The temperature difference should be large because the accuracy of a thermocouple is relatively large compared to real temperature differences. However, the flow rate cannot be too low because the flow has to be turbulent to avoid temperature stratification of the flow.

3.1.4 Saturation pressure control loop

To control the saturation pressure of the test section, the amount of refrigerant in the circuit has to be controlled. This is done by a temperature controlled buffer vessel (figure 3.2). This buffer vessel can contain more or less refrigerant depending on its temperature. The temperature of the buffer vessel is regulated using a precision *Refrigerated Heating Circulator Bath* (Huber CC-415). This machine controls a thermal oil to a certain temperature. This thermal oil is then pumped through 2 hair-pin tubes inside the buffer vessel. The temperature of the *Refrigerated Heating Circulator Bath* is controlled by the computer.

[3] More information can be found in appendix A.

3.2 Test Section

3.2.1 Overview of the test section

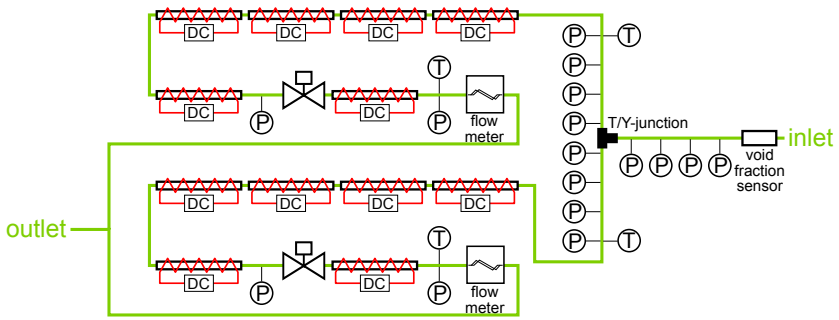

Figure 3.5: Schematic overview of the test section.

Figure 3.5 shows a schematic representation of the test section. First, the conditioned two-phase refrigerant flow flows through an in-house made capacitive void fraction sensor, which will be discussed later on. Then the refrigerant flow enters the T-junction under test. After the junction, the flow is split into two identical circuits which recombine at the end of the test section. In each parallel circuit the flow passes sequentially through an evaporator (5 electrical heated tubes of 600 W each), a valve, a superheater (1 electrical heated tube of 600 W) and a Coriolis-type mass flow meter (Krohne Optimass 6000 S10). Further, the pressure gradient over the junction is measured using a multiplexed differential pressure transducer (Endress+Hauser Deltabar S PMD75). This pressure gradient measurement will be elaborated on in the next subsection. Finally, the pressure and temperature is measured before the junction and at the end of each parallel circuit. Hence, the vapour quality at the inlet of each parallel circuit can be obtained by applying the first law of thermodynamics over each parallel circuit. More details on the calculation method and its accompanying uncertainty analysis can be found in appendix A.

3.2.2 Pressure gradient measurement

In order to measure the pressure gradient over the junction, the pressure is measured at several locations before and after the junction. The exact locations are shown in figure 3.6. To avoid the occurrence of vortices in the flow, which could disturb the pressure measurement, the pressure tap should be as small as possible and burr-free [63]. Hence, the holes for the pressure taps (D = 0.5 mm) were made using die-sink electrical discharge machining. The pressure taps are connected through capillary tubes to a multiplexer made of an array of solenoid valves. This

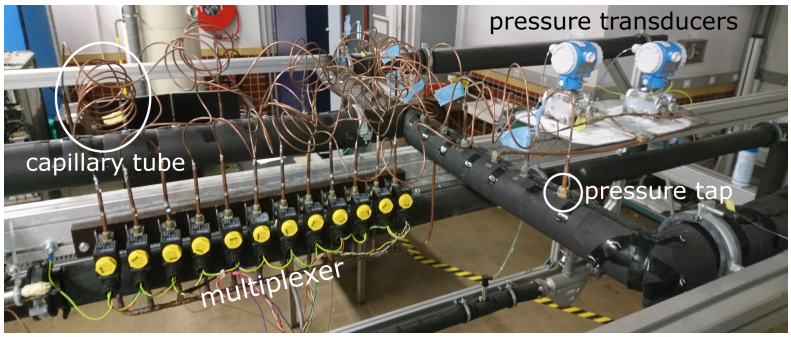

Figure 3.7: Picture of the pressure gradient measuring equipment

multiplexer connects a pressure tap and a reference pressure tap to two differential pressure transducers. The first transducer has a range of $1\,\mathrm{kPa}\pm0.75\,\mathrm{Pa}$ and the second one has a range of $10\,\mathrm{kPa}\pm7.5\,\mathrm{Pa}$. Figure 3.7 shows the pressure taps, capillary tubes, multiplexer and pressure transducers.

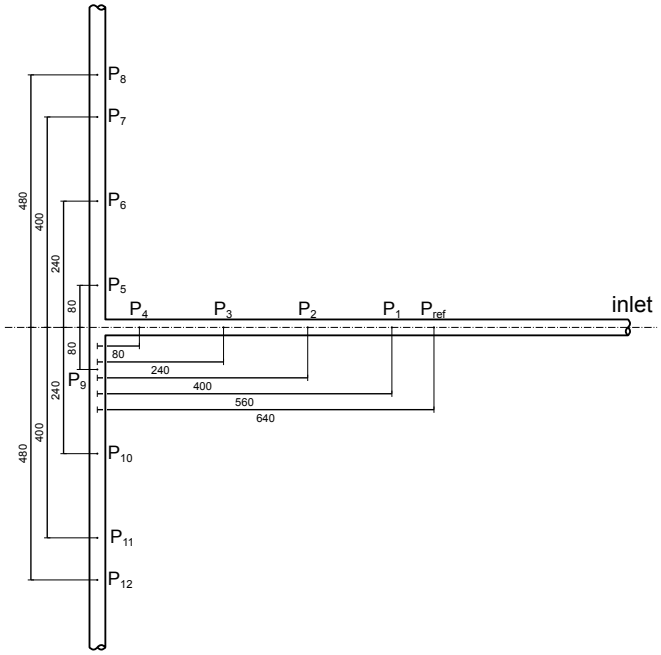

Figure 3.6: Positioning of the pressure tabs at the test section

3.2.3 Void fraction sensor

Before the junction, the void fraction is measured using an in-house made capacitive void fraction sensor. The temporal data of the void fraction is used to determine the flow regime. The void fraction sensor and the dataprocessing method was developed in the PhD of De Kerpel [21, 64, 65]. For the sake of completeness, the working principle of the sensor will be explained below.

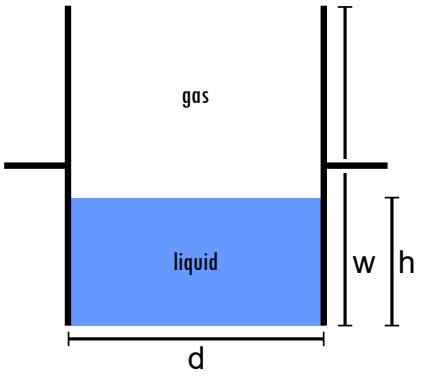

Figure 3.8: Schematic representation of a simplified void fraction sensor.

Figure 3.8 is a simplified model of the sensor. The sensor is in essence a simple parallel plate capacitor with a surface area A separated by a distance d. The capacity C of this capacitor is given by equation 3.1 with ϵ_0 being equal to $8.854 \times 10^{-12}\,\mathrm{F/m}$, the absolute permittivity of free space. ϵ_r is the dielectric constant of the medium between the capacitor plates.

$$C = \frac{\epsilon_0\,\epsilon_r\,A}{d} \quad [\mathrm{F}] \tag{3.1}$$

The dielectric constant k of the gas phase is different from the liquid phase. Hence, there exists a relation between the measured capacity of the capacitor and the spacial distribution of the two phases between the capacitor plates. For the simplified model depicted in figure 3.8 this yields:

$$C' = \frac{\epsilon_0\,\left(\epsilon_{r,l}\,h + \epsilon_{r,g}\,\left(w-h\right)\right)}{d} \quad [\mathrm{F/m}] \tag{3.2}$$

Further, the spacial distribution of the two phases fluctuates in time due to turbulence and surface waves. The nature of this temporal variation depends on the flow regime as seen in figure 3.9a. Hence, based on the frequency spectrum of this void fraction, the flow regime can be determined. A maximum overlap wavelet transform (MODWT) with the 8^{th} order Daubechies wavelet function is performed on the void fraction time signal and the wavelet variance is calculated

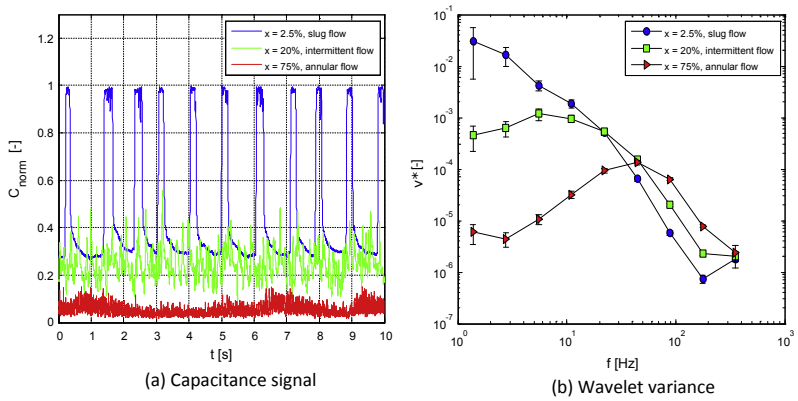

Figure 3.9: The relation between the void fraction time trace and the flow regime [64].

(figure 3.9b). The slope between the 3rd and 4th wavelet variance is used to classify the different flow regimes with a fuzzy clustering algorithm. More details about this classification method can be found in the PhD thesis of De Kerpel [21, 64].

When the flow regime is known, the real void fraction can be calculated by flow regime dependent calibration curves [21, 64]. In appendix B, the flow regime and void fraction measurements are used to verify correlations from literature.

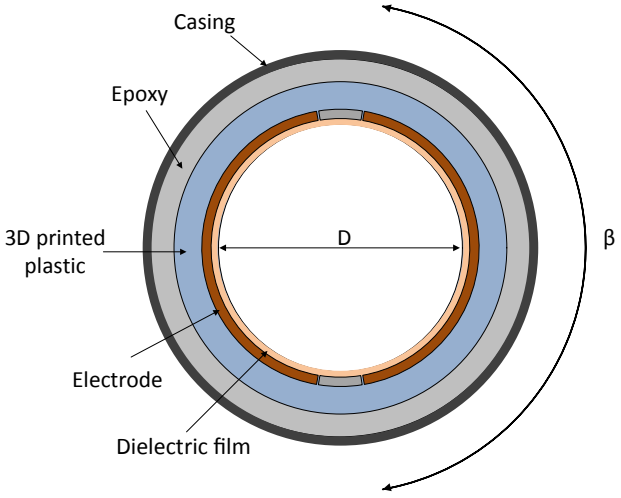

Figure 3.10: Cross section of the void fraction sensor [22].

In reality the sensor is not square. A schematic cross-sectional view of the sensor is given in figure 3.10. More constructional details about the sensor can be found in the PhD thesis of De Kerpel [21] and Canière [22].

3.3 Test methodology

Each measurement is uniquely determined by its inlet refrigerant flow and the mass split ratio over the junction. The inlet refrigerant flow is set by regulating the saturation pressure, the mass flux and the vapour quality in the two-phase flow conditioner. The mass split ratio is regulated using the valves in the parallel sections of the test section. By closing one of the valves, the back pressure of this branch will increase, decreasing the mass flow rate through this branch. An overview of the inlet conditions, with their range capable by the experimental setup, are given in table 3.1.

Parameter	Range	Uncertainty
G_1	100-600 $\mathrm{kg/(m^2{\cdot}s)}$	$2\,\%$
x_1	0-1	0.02
T_{sat}	10-20 °C	0.08 °C
D_{in}	$0.008\,\mathrm{m}$	$0.000\,05\,\mathrm{m}$
θ	0-90°	1°
$\frac{\dot{m}_2}{\dot{m}_1}$	0.2-0.8	0.01
fluids	R32, R134a, R1234ze, R125	

Table 3.1: The inlet parameters of the experimental setup with their range and uncertainty.

For each measurement, the power of the evaporators and superheaters in the test section is set such that a stable superheated refrigerant flow is obtained at the end of each parallel circuit. This superheat is necessary to measure the state of the refrigerant at the end of the test section. Moreover, a Coriolis-type mass flow meter cannot measure a two phase flow.

After a certain measurement condition is set, it typically takes 20 minutes to reach a steady state condition. When steady state is reached, during 10 minutes all sensor readings are recorded at a rate of $0.17\,\mathrm{Hz}$ and stored on a computer. For the void fraction measurement, only the last 5 seconds are recorded at $250\,\mathrm{Hz}$ in order to limit the amount of data. The pressure gradient is measured by sequentially measuring the pressure at the pressure taps. The multiplexer is used to connect the pressure taps one by one to the pressure transducer. After switching the multiplexer, 10 seconds is waited before the pressure is recorded during a period of 10 seconds. The measured data is considered valid if the energy balance closes within $5\,\%$. On average the energy balance closes within $2.2\,\%$.

The data collected during a test is post-processed to get the F_l and F_g values with their uncertainties. The F_l and F_g values can be calculated using equation 2.11 and 2.12. The mass flow rates in both equations are measured. However, the vapour qualities cannot be measured but are calculated by applying the conservation of energy over the two parallel circuits of the test section. On average

the absolute uncertainty on the vapour quality is 0.02 and 0.015 for the inlet and the outlets, respectively. The post-processing methods are described more detailed in appendix A.

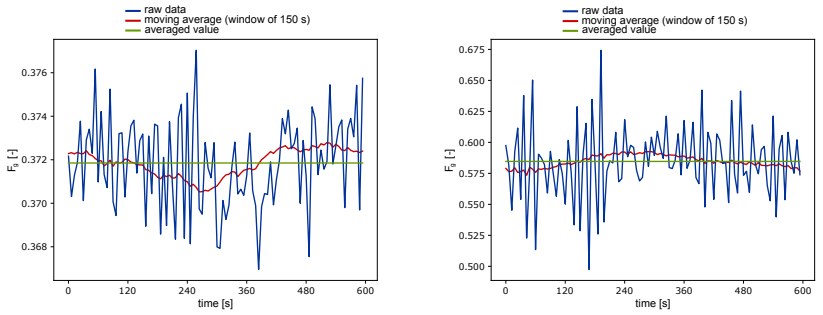

(a) Annular flow ($J_g = 4\,\mathrm{m/s}$; $J_l = 0.1\,\mathrm{m/s}$) *(b) Slug flow ($J_g = 1\,\mathrm{m/s}$; $J_l = 0.2\,\mathrm{m/s}$)*

Figure 3.11: The comparison of the variation of F_g-value in time during one experiment for different flow regimes.

Due to the unstable nature of two-phase flows (slugs, surface waves,...), the distribution in the T-junction is not steady over time. This is illustrated in figure 3.11. It shows the time variation of the F_g-value during one experiment. For the slug flow (figure 3.11b), large fluctuations can be observed compared to the annular flow (figure 3.11a). A slug flow consists of a periodic alternation between liquid slugs and elongated bubbles which have diameters similar in size to the channel diameter. This means that T-junction has to divide alternately an almost full liquid flow and an almost full vapour flow. Hence, phase distribution will change over time, however on average this flow is in steady state.

The post-processing method should be robust enough to deal with these fluctuations in time. To test the robustness, two extreme cases were compared. In the first case, all the measured values were first averaged and then post-processing method is applied. In the second case, the post-processing method is first applied to each set of measured values (unique timestamp) and the averaging is done at the end. The end result of both cases are within the uncertainty bounds. For the remaining tests the first post-processing method was used.

3.3.1 Verification of the experimental setup

First, the repeatability of the experimental setup was verified by repeating several experiments on a different day. The results of the repeated tests were within the uncertainty bounds of their original measurement.

Secondly, the conservation of energy over the preheater and the test section was checked using a single phase flow. The heat transferred in the preheater was

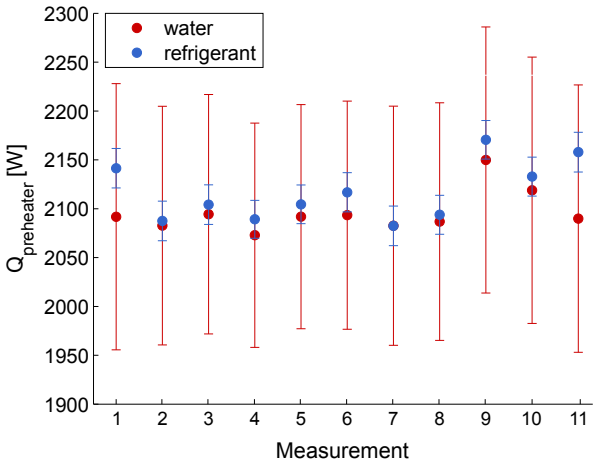

Figure 3.12: The conservation of energy over the preheater for a single phase R32.

verified by comparing the enthalpy change of the hot water over the preheater with the one of the refrigerant over the preheater. This comparison is shown in figure 3.12. By comparing the enthalpy change of the refrigerant over the test section with the heat generated by the electrical heaters, the conservation of energy over the test section was reviewed. The conservation of energy over the test section is illustrated in figure 3.13.

Finally, the pressure drop measurements were verified for a single phase flow. The Fanning friction factors f measured in the inlet and outlets of the T-junction are compared with the correlation of Gnielinski *et al.* [66]. This comparison is visualised in figure 3.14. Most of the experimental measurements are within the $20\,\%$ uncertainty bounds.

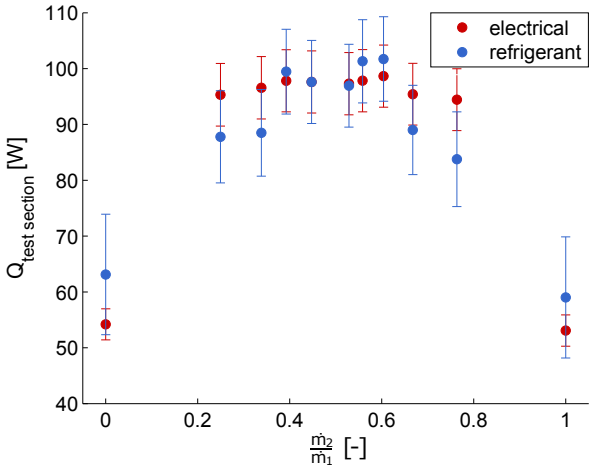

Figure 3.13: The conservation of energy over the test section for a single phase R32.

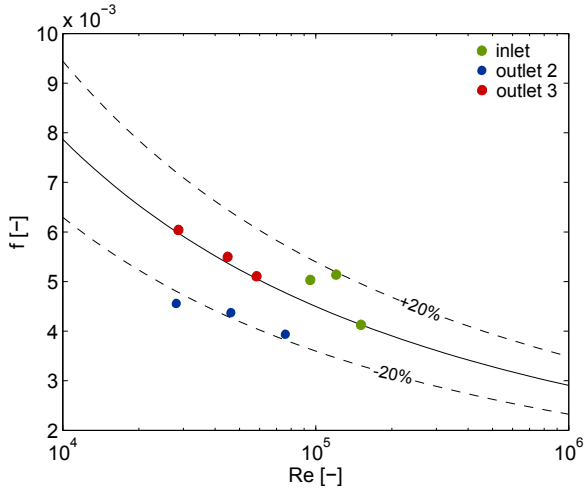

Figure 3.14: The Fanning friction factors f as function of the Reynolds number. The experimental values measured in the inlet and outlets of the T-junction are compared with the correlation of Gnielinski et al. *[66].*

4
Experimental results

This chapter will discuss the experimental results obtained during this work. A total of 60 inlet conditions were experimentally investigated All inlet conditions are listed in table C.1. For each inlet condition a $F_g - F_l$-graph was obtained experimentally, which means that in total 696 individual experiments were conducted.

The different parameters which affect the phase distribution over an impacting T-junction will be discussed in this chapter. The insights gained in this chapter will then be used to construct a new model in the next chapter. Before a parameter study can be conducted, first the 'performance' parameter used to compare the results has to be selected.

4.1 How to compare experimental results?

For each unique inlet condition (mass flux, vapour quality, saturation temperature and refrigerant) a F_g-F_l graph, such as figure 4.1, was generated. To measure the different points in the F_g-F_l graph, the back-pressure of one of the parallel channels was changed using a valve. By closing the valve in one channel, the total mass flow rate going to this channel can be regulated.

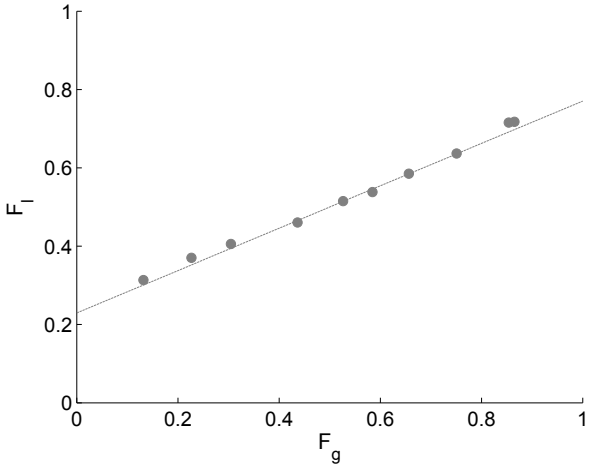

Figure 4.1: The liquid mass fraction F_l as function of the vapour mass fraction F_g of an R32 experiment (T_{sat} = 10 °C; J_g = 1 m/s; J_l = 0.2 m/s) with the fitted $F_g - F_l$ line.

It is difficult to compare the influence of the inlet conditions on the phase distribution using the F_l-F_g graph. This set of measurement per unique inlet condition has to be reduced to a single number. This is accomplished by reducing the measurements to the slope of the best fitting linear line (see figure 4.1).

A general expression of a linear line, with an intercept a and a slope b, is given in equation 4.1. In this work the straight line should pass through the point $(0.5; 0.5)$ as explained previously on page 16. This extra constraint leads to a relation between the intercept a and the slope b given in equation 4.2.

$$y = a + b \cdot x \tag{4.1}$$

$$a = \frac{1 - b}{2} \tag{4.2}$$

The regression line is fitted considering the uncertainties on the values of F_g and F_l. Based on the book of Bevington [67], the method of maximum likelihood is applied. The likelihood of the slope b is given by equation 4.3.

$$P[b] = \prod_{i=1}^{n} \left[\frac{1}{\sqrt{2\pi\bar{\sigma}_{x_i}^2}} \exp\left(-\frac{1}{2} \frac{\left(x_i - \bar{\mu}_{x_i}\right)^2}{\bar{\sigma}_{x_i}^2} \right) \right. \\ \left. \frac{1}{\sqrt{2\pi\bar{\sigma}_{y_i}^2}} \exp\left(-\frac{1}{2} \frac{\left(y_i - \frac{1-b}{2} - b\bar{\mu}_{x_i}\right)^2}{\bar{\sigma}_{y_i}^2} \right) \right] \tag{4.3}$$

There was assumed that the uncertainty on values F_g and F_l can be represented by a Gaussian distribution. x_i and y_i can respectively be replaced by the F_g value and the F_l value of the i^{th} measurement. $\bar{\sigma}_{x_i}$ and $\bar{\sigma}_{y_i}$ can respectively be replaced by the uncertainty of the F_g value and the uncertainty of the F_l value of the i^{th} measurement. $\bar{\mu}_{x_i}$ is the most likely value of F_g of the i^{th} measurement considering the linear regression.

The best fitting line maximises the likelihood $P[b]$. The design parameters of this maximisation function are the slope b and i most-likely values $\bar{\mu}_{x_i}$. Finding the maximum of the likelihood $P[b]$ is equivalent to finding the minimum of the sum in the exponential (Eq. (4.4)). The minimum is determined numerically.

$$\chi^2 = \sum_{i=1}^{n} \left[\frac{\left(x_i - \bar{\mu}_{x_i}\right)^2}{\bar{\sigma}_{x_i}^2} + \frac{\left(y_i - \frac{1-b}{2} - b\bar{\mu}_{x_i}\right)^2}{\bar{\sigma}_{y_i}^2} \right] \tag{4.4}$$

The likelihood function is a product of Gaussian probability density functions, thus itself is also a Gaussian probability density function [68]. The book of Bevington [67] states that the uncertainty on the parameter b is given by equation 4.5 if the likelihood function is Gaussian.

$$\bar{\sigma}_b = \sqrt{2\left(\frac{\partial^2\chi^2}{\partial b^2}\right)^{-1}} = \sqrt{2\left(\sum_{i=1}^{n}\left[\frac{2}{\bar{\sigma}_{y_i}^2}\left(\bar{\mu}_{x_i}^2 - \bar{\mu}_{x_i} + \frac{1}{4}\right)\right]\right)^{-1}} \tag{4.5}$$

As verification, the b-values obtained with this analytical solution were compared with the ones found using the Monte Carlo method. With a Monte Carlo simulation, a large amount ($n = 5\,000\,000$) of fictitious sets of measurements are generated based on the probability distribution of the real measurements. For each fictitious set of measurements a linear regression is performed. Assuming the the slope b has a Gaussian distribution, the best fitting slope b and its uncertainty is respectively given by the mean and the standard deviation of all the slopes b obtained during the simulations. The assumption of the slope b having a Gaussian distribution was verified by plotting the histogram against a Gaussian probability density function. As an example, two of these histograms are shown in figure 4.2. The deviation between the analytical method and the Monte Carlo simulations was negligible.

Note that the above method is only valid for the horizontal experiments. The experiments with a tilted outlet branch will in most cases not go through the

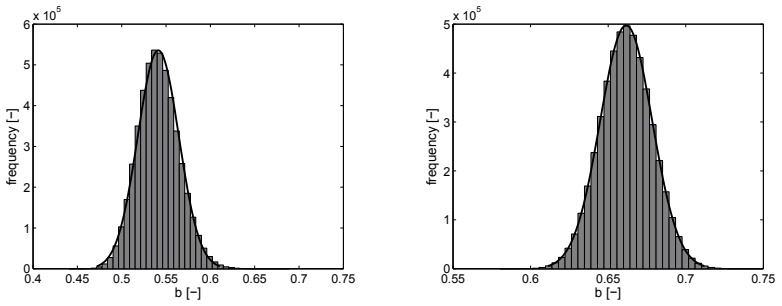

(a) R32; T_{sat} = 10 °C*;* J_g = 1 m/s*;* J_l = 0.2 m/s

(b) R32; T_{sat} = 10 °C*;* J_g = 6 m/s*;* J_l = 0.1 m/s

Figure 4.2: The histogram of the slope b obtained by the Monte-Carlo method compared with the Gaussian probability density function.

center point. The influence of the inclination of the T-junction will be investigated graphically.

4.2 Parameters influencing the phase distribution

4.2.1 Influence of the superficial liquid velocity J_l and the superficial vapour velocity J_g

The influence of the two inlet superficial velocities was investigated using the refrigerant R32 at a saturation temperature of $10\,°\mathrm{C}$. Later, a few selected experiments with other refrigerants and at different saturation temperatures were conducted to verify the trends found with R32.

In a typical domestic heat pump, the flow enters the distributor with a mass flux of $150\,\mathrm{kg/(m^2{\cdot}s)}$ to $600\,\mathrm{kg/(m^2{\cdot}s)}$ and a vapour quality between $5\,\%$ and $40\,\%$ [44]. Hence, the experiments conducted in this work will be focused on this region keeping the limitation of the experimental setup in mind. Figure 4.3 shows experimental matrix for R32 displayed in the flow regime map of of Wojtan *et al.* [28]. Due to region of interest, most experiments were conducted in the annular and intermittent flow.

In the literature, the inlet conditions are often represented as superficial velocities. Furthermore, this work will also use the superficial velocities to describe the inlet condition. Hence, figure 4.3 can be transformed to figure 4.4, which shows the flow regime map in function of the superficial velocities.

Figure 4.5 shows the slope b as a function of the inlet superficial vapour velocity for different inlet superficial liquid velocities. First, a discontinuity can be noticed when there is a flow regime transition. Within a flow regime the trend of the inlet superficial vapour velocity remains the same. This discontinuity

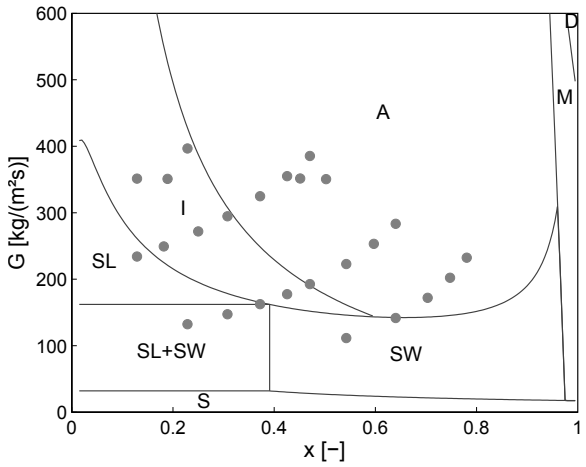

Figure 4.3: Inlet conditions (vapour quality and mass flux) of the experiments of R32 at a saturation temperature of $10\,°\mathrm{C}$ *displayed in a flow regime map of Wojtan* et al. *[28] extended by Barbieri* et al. *[29] (S: Stratified; SW: Stratified-Wavy; I: Intermittent; A: Annular; SL: Slug; M: Mist; D: Dry-out)*

confirms the importance of the flow regime's influence on the phase distribution over an impacting T-junction. In the literature [41, 47], this discontinuity was also observed. Figure 4.6 shows the results of El-Shaboury *et al.* [47]. The F_g – F_l-graph rotates anti-clockwise with increasing inlet superficial vapour velocity except when the flow regime changes from wavy to annular. However, due to the lack of data, the authors could not determine whether the influence of the inlet superficial vapour velocity reversed for an annular flow or whether there is just a discontinuity in the results.

Second, for an inlet superficial liquid velocity equal or higher than $0.2\,\mathrm{m/s}$, the slope b increases with increasing inlet superficial vapour velocity. An increasing slope b is equivalent to an anti-clockwise rotation of the F_g – F_l-graph. In other words, the liquid has a decreasing preference of flowing to the branch with the lowest mass flow rate with increasing inlet superficial vapour velocity. This trend of the inlet superficial vapour velocity is consistent with the literature [40–42, 47].

For an inlet superficial liquid velocity equal or lower than $0.1\,\mathrm{m/s}$, the slope b decreases with increasing inlet superficial vapour velocity within the same flow regime. A decreasing slope b is equivalent to a clockwise rotation of the F_g – F_l-graph. Hence, the liquid has an increasing preference of flowing to the branch with the lowest mass flow rate with increasing inlet superficial vapour velocity.

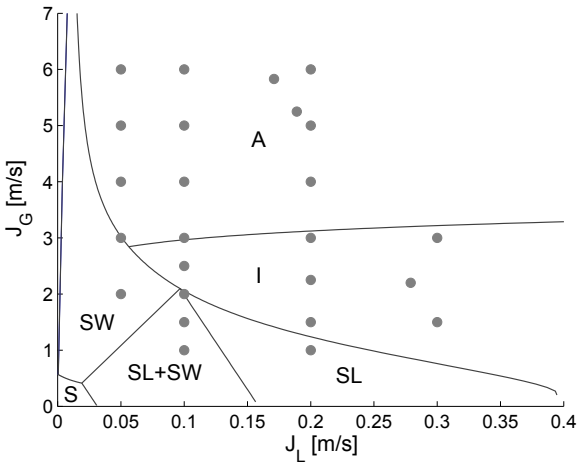

Figure 4.4: Inlet superficial velocities of the experiments of R32 at a saturation temperature of $10\,°\mathrm{C}$ *displayed in a flow regime map of Wojtan* et al. *[28] extended by Barbieri* et al. *[29] (S: Stratified; SW: Stratified-Wavy; I: Intermittent; A: Annular; SL: Slug)*

This trend is opposite to the trend observed for higher inlet superficial liquid velocities. Furthermore, this trend does not comply with the data found in the literature.

This behaviour can be explained by the liquid droplets entrained in the vapour flow. First of all, for increasing liquid velocities, entrainment of liquid as droplets in the vapour flow will increase [69]. This amount of entrained liquid increases also slightly with increasing inlet vapour velocities. Furthermore, with increasing momentum of the liquid phase, more liquid will be dispersed as droplets after impacting at the T-junction [12]. Hence for high superficial liquid velocities, more liquid is dispersed as droplets than for low superficial liquid velocities. Furthermore, the mean droplet diameter decreases for increasing vapour velocities [70]. Smaller droplets are more easily entrained in the vapour flow. An increasing superficial vapour velocity leads to more momentum to entrain the liquid droplets and thus creating a more uniform distribution. Thus, this explains the increasing slope b with increasing superficial vapour velocity for an inlet superficial liquid velocity equal or higher than $0.2\,\mathrm{m/s}$. The relation between the occurrence of entrained droplets and the phase distribution was already found by *Tuo et al.* [12] for vertical impacting T-junctions.

For an inlet superficial liquid velocity equal or lower than $0.1\,\mathrm{m/s}$, this mechanism of droplet entrainment, which tends to homogenise the flow, does not have a significant influence due to a smaller amount of droplets.

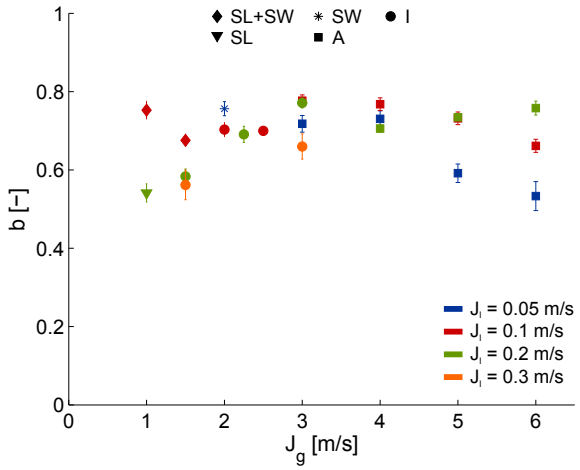

Figure 4.5: Slope b as function of the inlet superficial vapour velocity for different inlet superficial liquid velocities (R32; T_{sat} = 10 °C).

To verify the trends described above, the influence of the inlet superficial vapour velocity was investigated for three other refrigerants (R134a, R125 and R1234ze) and at a different saturation temperature. Figure 4.7 displays the influence of the inlet superficial vapour velocity for R32 at a saturation temperature of 20 °C. The qualitative trends observed at the higher saturation temperature are the same as at the low saturation temperature.

Figure 4.8 displays the influence of the inlet superficial vapour velocity for three other refrigerants. For the different refrigerants, the qualitative trends observed are equal to the ones of R32 at both the low and high inlet superficial liquid velocities. This confirms that the trends observed are purely related to the inlet superficial velocities.

4.2.2 Influence of the fluid properties

The influence of the fluid properties was investigated by varying the saturation temperature and by changing the refrigerant being tested. This way of working has one major drawback. By changing the fluid or varying the saturation temperature, multiple properties are changed simultaneously and therefore their individual influence on the phase distribution cannot be isolated easily. Based on the governing physical laws, three fluid properties were selected to be investigated: density, dynamic viscosity and surface tension.

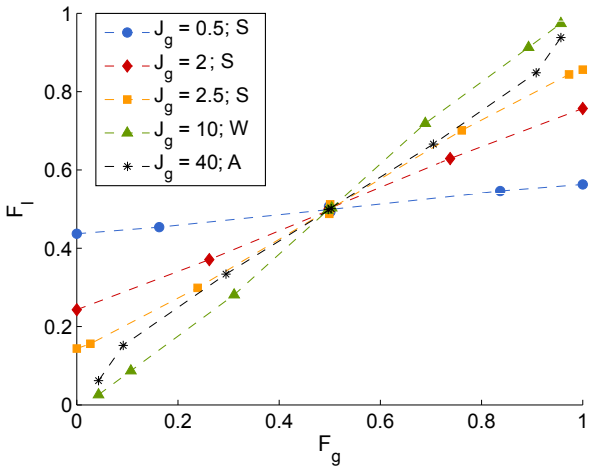

Figure 4.6: The liquid mass fraction F_l as function of the vapour mass fraction F_g for different superficial vapour velocities J_g and a superficial liquid velocity of $0.01\,\mathrm{m/s}$ *[47].*

J_l [m/s]	J_g [m/s]	ρ_g/ρ_l [-]	μ_g/μ_l [-]	σ [N/m]	b [-]
0.2	1.5	0.0018	0.018	0.073	0.28
0.2	3	0.0018	0.018	0.073	0.17
0.3	1.5	0.0018	0.018	0.073	0.31
0.3	3	0.0018	0.018	0.073	0.16

Table 4.1: The properties and the slope b determined using the model of El-Shaboury et al. *[47] for a water-air mixture (T = 20 °C; $P = 1.5 \times 10^5$ Pa).*

Density The influence of the vapour-liquid density ratio $\frac{\rho_g}{\rho_l}$ on the phase distribution is shown in figure 4.9. Note that the measurements of R1234ze should have a slightly higher slope b due to the fact that the superficial liquid velocity is $0.225\,\mathrm{m/s}$ instead of $0.2\,\mathrm{m/s}$ (see section 4.2.1). First of all, a strong influence of the fluid itself can be observed. Furthermore, the saturation temperature shows no significant influence on the phase distribution if the superficial vapour velocity is equal to $3\,\mathrm{m/s}$. For a superficial vapour velocity equal to $1.5\,\mathrm{m/s}$, the slope b increases and decreases for R32 and R125 respectively with increasing saturation temperature.

On average, the slope b increases with increasing density ratio. Hence, the phases are distributed more homogeneously with increasing density ratio. The small deviations of the general trend can be attributed to other fluid properties. The general trend of the density ratio can further be acknowledged by comparing the refrigerants with water-air mixtures. Table 4.1 contains the properties and the

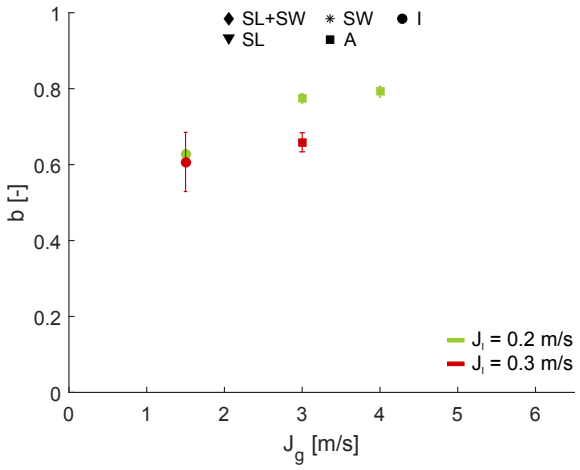

Figure 4.7: Slope b as function of the inlet superficial vapour velocity for different inlet superficial liquid velocities (R32; T_{sat} = 20 °C).

slope b of a water-air mixture with the same inlet conditions as the refrigerants. The slope b was determined using the phase distribution model of El-Shaboury *et al.* [47]. If the air-water data in table 4.1 is compared with the refrigerant results in figure 4.9, a continuation of the the trend can be observed.

This increasing slope b with increasing density ratio can be explained rationally: If the density ratio is almost equal to 1, there is almost no difference in density and the two-phase mixture will react as if it were a single phase. For a homogeneous distribution, the slope b is 1. Therefore the slope b should increase with increasing density ratio until it reaches a value of 1.

Additionally, the density ratio is closely related to the momentum ratio $\dot{m}_{1,g} \cdot v_{1,g} / \dot{m}_{1,l} \cdot v_{1,l}$. If the density of the vapour phase decreases, the velocity of the vapour phase should increase to keep a constant mass flow rate through a channel. Hence, the momentum ratio increases with increasing density ratio. The influence of the momentum ratio on the phase distribution is shown in figure 4.10. The slope b increases with increasing momentum ratio which can be explained by the increasing ability of the vapour flow to entrain liquid droplets. This influence of the momentum ratio on the phase distribution was already mentioned by Mohamed *et al.* [37].

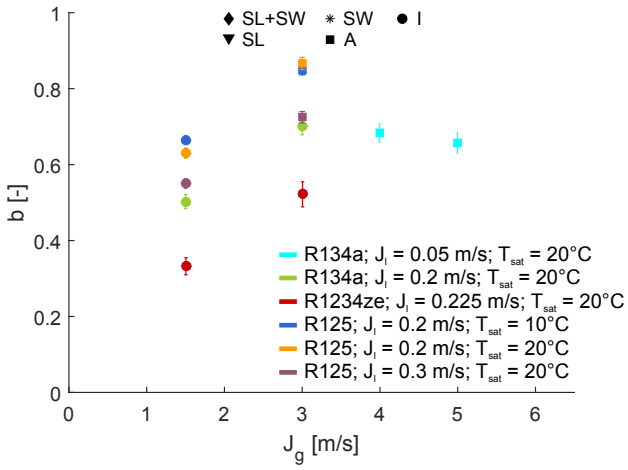

Figure 4.8: Slope b as function of the inlet superficial vapour velocity for different inlet superficial liquid velocities and different refrigerants.

Dynamic viscosity The influence of the vapour-liquid viscosity ratio $\frac{\mu_g}{\mu_l}$ on the phase distribution is shown in figure 4.11. No clear trend of the slope b as a function of the viscosity ratio can be found. Based on the experimental results, one can conclude that the viscosity ratio has no significant influence on the phase distribution.

Surface tension The influence of the surface tension σ on the phase distribution is displayed in figure 4.12. On average, the slope b decreases with increasing surface tension. Hence, more maldistribution of the phases occurs with increasing surface tension. If the experimental data in figure 4.12 is extended with the water-air data given in table 4.1, it is clear that the trend continues.

The influence of the surface tension can be explained by the droplet entrainment mechanism. First of all, the mean droplet size decreases with decreasing surface tension [70]. Smaller droplets are more easily transported by the vapour phase, leading to a more homogeneous distribution of the phases. Furthermore, a lower surface tension promotes the entrainment of the liquid as droplets in the vapour flow [71]. Hence, there are more droplets carried by the vapour phase.

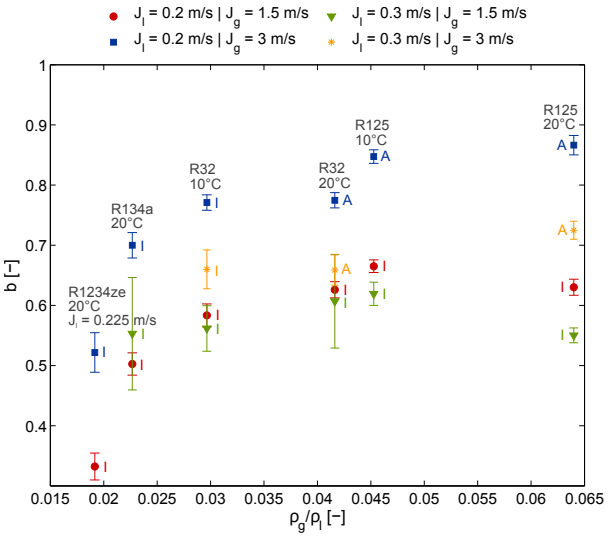

Figure 4.9: Slope b as function of the density ratio $\frac{\rho_g}{\rho_l}$ for different inlet superficial liquid velocities, saturation temperatures and refrigerants.

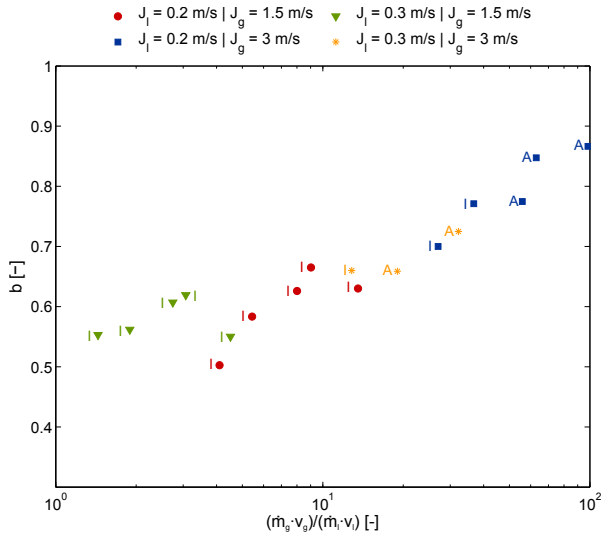

Figure 4.10: Slope b as function of the momentum ratio of the inlet $\frac{\dot{m}_{1,g} \cdot v_{1,g}}{\dot{m}_{1,l} \cdot v_{1,l}}$ for different inlet superficial liquid velocities, saturation temperatures and refrigerants.

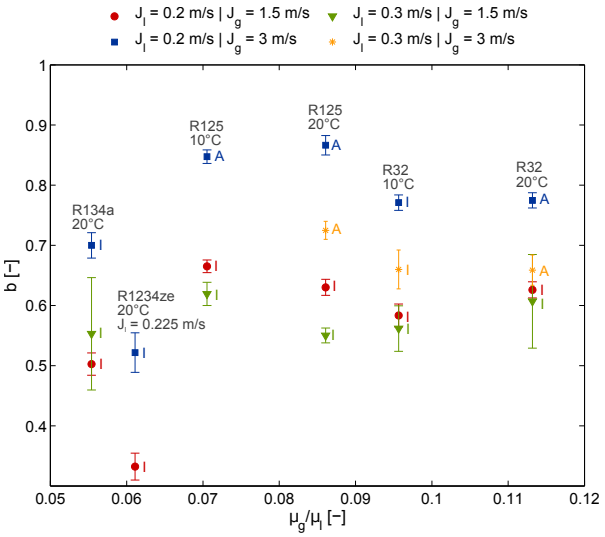

Figure 4.11: Slope b as function of the vapour-liquid viscosity ratio $\frac{\mu_g}{\mu_l}$ for different inlet superficial liquid velocities, saturation temperatures and refrigerants.

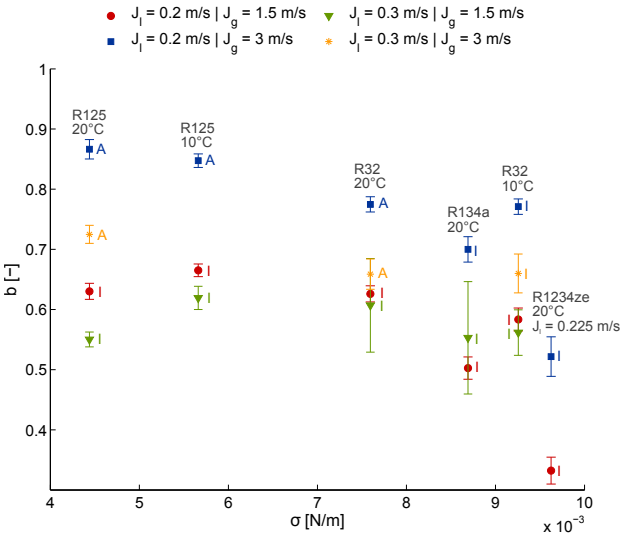

Figure 4.12: Slope b as function of the surface tension for different inlet superficial liquid velocities, saturation temperatures and refrigerants.

4.2.3 Influence of the inclination angle

The influence of the T-junction's inclination θ on the phase distribution was investigated by performing experiments for three inclination angles: $0°$, $22.5°$ and $45°$. Figure 4.13 illustrates the influence of the T-junction's inclination θ for R32 at different inlet conditions. Similar experiments were conducted for R125 and are shown in figure 4.14. By increasing the inclination, the F_g – F_l-graph for the downwards facing outlet shifts towards the upper left corner. Hence, the liquid phase has an increasing preference of flowing towards the downward facing outlet. This trend is explained by the fact that the gravity force has the largest influence on the liquid phase, being the one with the highest density.

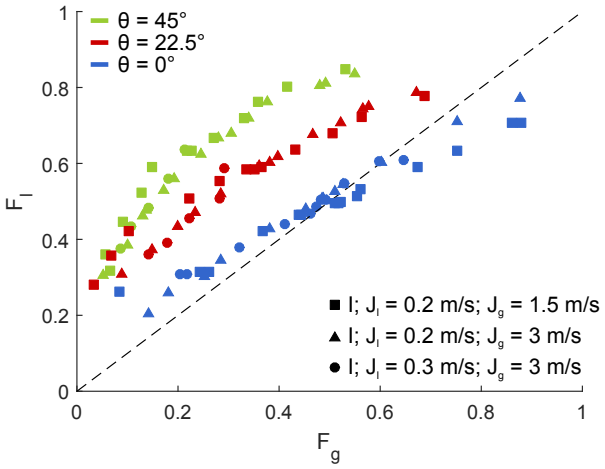

Figure 4.13: The liquid mass fraction towards the downward-facing outlet as function of the vapour mass fraction towards the same outlet for different T-junction inclination angles θ (R32; T_{sat} = 10 °C).

Figure 4.14 shows that the influence of the inlet superficial vapour velocity remains the same: The F_g – F_l-graph rotates counter clockwise with increasing inlet superficial vapour velocity.

In figure 4.14 it appears that there is no significant combined effect of the flow regime. The shift of the graphs is equal for the intermittent and annular flow. However, this does not exclude the possible influence of the flow regime because both flow regimes have a rather similar spatial distribution of the two phases in the tube's cross-section.

If the experimental trends are compared to the literature (figure 2.9), the trends found for annular water-air mixtures show less influence of the inclination. This trend is opposite of the one expected. First of all, the smaller density ratio of the water-air mixture leads to a large difference of the gravity force, forcing the

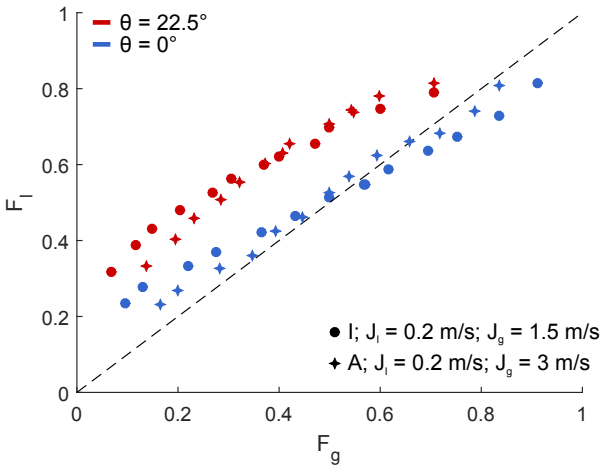

Figure 4.14: The liquid mass fraction towards the downward-facing outlet as function of the vapour mass fraction towards the same outlet for different T-junction inclination angles θ (R125; T_{sat} = 10 °C).

water-air mixture to separate. Further, the larger surface tension of the water-air mixture leads to larger droplets which are less likely to be entrained by the vapour phase. However, the larger surface tension also means a stronger wetting of the tube's wall. This could explain the observed trends. Due to the larger surface tension, the liquid has the tendency to move along the junction's wall, leading to a more equal splitting. In the literature, this phenomena is also observed for micro-tubes, where this capillary effect is even more pronounced [12, 31].

4.3 Pressure drop over an impacting T-junction

The pressure drop over the T-junction was determined using a similar method adopted by previous works [47, 55]. The pressure was measured at several locations just upstream and downstream of the T-junction (see section 3.2.1) where there is no disturbance of the T-junction. This results in a graph like figure 4.15. For both outlets and the inlet, a best fitting straight line through the measurements is constructed. Assuming the pressure measurements are not influenced by the junction, the slope of this line is the pressure gradient of a undisturbed tube section. This pressure gradient is used to extrapolate the pressure at the junction of the inlet and both outlets. The pressure drop over the junction from inlet to the i-th outlet (ΔP_{1i}) is then given by the difference in the extrapolated pressures.

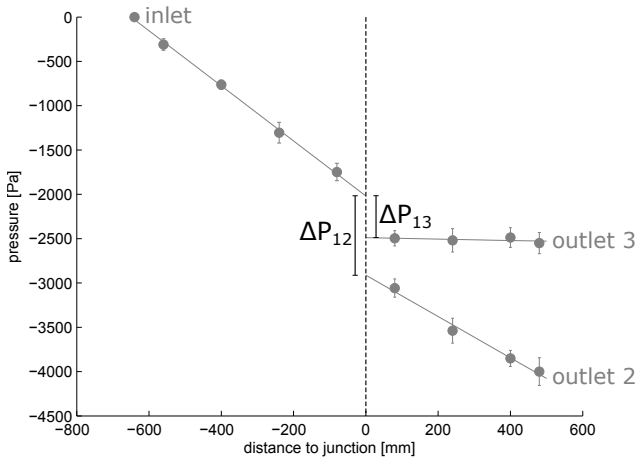

Figure 4.15: Method for determining the pressure drop over a T-junction. The experimental data is used to extrapolate at the junction.

The method as described above assumes that the pressure drop measurements are not disturbed by the T-junction. To verify this assumption, the calculated pressure gradient is compared with the one measured over a longer tube section. First, the pressure difference between the absolute pressure measurement at the outlet of the flow conditioner and the absolute pressure measurement just before the first evaporator heater of outlet 2 was determined. In figure 4.16, this pressure difference is compared with the pressure difference calculated using the pressure gradient determined near the T-junction. The absolute pressure difference is in good agreement with the calculated value (MAE = $11\,\%$), confirming there is no influence of the T-junction.

Ito and Imai [72] developed an empirical correlation for single phase pressure

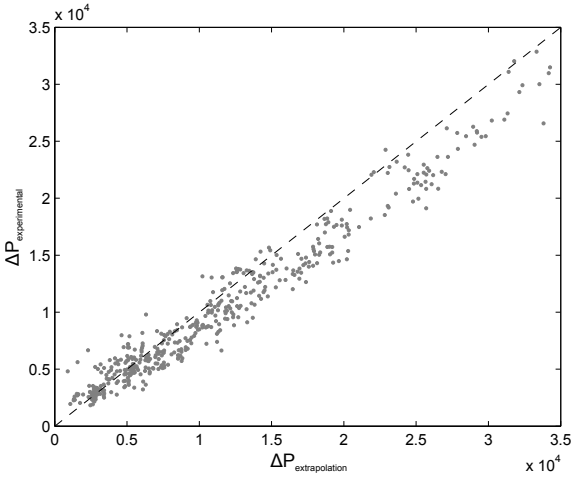

Figure 4.16: The pressure difference measured between the inlet of the test section and just before the first evaporator heater of outlet 2 as function of the pressure difference determined using extrapolation.

drop over an impacting T-junction. The model is described by equation 4.6 and 4.7. Equation 4.6 starts from the Bernoulli equation and the irreversible term is replaced by a constant K_{1i} times the inlet kinetic energy. This constant K_{1i} is a function of the mass fraction going to the outlet.

$$\begin{aligned} \Delta P_{1i} &= \rho\left(\frac{v_i^2}{2} - \frac{v_1^2}{2}\right) + \left(P_1 - P_i\right)_{irr.} \\ &= \rho\left(\frac{v_i^2}{2} - \frac{v_1^2}{2}\right) + K_{1i}\rho\frac{v_1^2}{2} \end{aligned} \tag{4.6}$$

$$K_{1i} = 0.59 + 1.18\left(\frac{\dot{m}_i}{\dot{m}_1}\right) - 0.68\left(\frac{\dot{m}_i}{\dot{m}_1}\right)^2 \tag{4.7}$$

Based on this single phase model, a two phase model will be developed. By assuming that the flow is homogeneous, the two phase mixture can be treated as if it were one phase. Hence, equation 4.6 can be rewritten to equation 4.8. $\hat{\rho}$ is the homogeneous inlet density defined by equation 4.9 and $\hat{v}$ is the homogeneous velocity defined by equation 4.10. The liquid and vapour density was assumed to remain constant over the T-junction even though it is related to the change in saturation pressure.

$$\Delta P_{1i} = \hat{\rho}_1\left(\frac{\hat{v}_2^2}{2} - \frac{\hat{v}_1^2}{2}\right) + K_{1i}\hat{\rho}_1\frac{\hat{v}_1^2}{2} \tag{4.8}$$

$$\hat{\rho}_i = \left(\frac{x_i}{\rho_g} + \frac{1 - x_i}{\rho_l} \right)^{-1} \tag{4.9}$$

$$\hat{v}_i = \frac{G_i}{\hat{\rho}_i} \tag{4.10}$$

Equation 4.8 was used to determine the constant K_{1i} for all experimental data (i.e. different refrigerants and both outlets). Figure 4.17 shows the obtained K_{1i}-values as a function of the mass fraction flowing towards the outlet for different inlet flow regimes. A clear linear trend can be observed. Hence, K_{1i} can be described by equation 4.11 with flow regime dependent coefficients (a and b) given in table 4.2.

$$K_{1i} = a + b \cdot \frac{\dot{m}_i}{\dot{m}_1} \tag{4.11}$$

	a	b
A	1.33±0.06	1.27±0.12
I	1.31±0.06	1.37±0.12
SL	1.44±0.36	0.96±0.7
SW	1.11±0.25	1.30±0.47
SL+SW	1.19±0.17	0.82±0.32

Table 4.2: Flow regime dependent coefficients of the K_{1i}-model with its 95 % confidence intervals.

Figure 4.18 compares the pressure drop measured with the pressure drop calculated using the new model (i.e. all refrigerants and both outlets). The model predicts rather well, especially at the higher pressure drops. 97 % of the data is predicted within the experimental uncertainty. The mean relative error (MRE) and the mean absolute error (MAE) of the model were calculated using equations 4.12 and 4.13.

$$\text{MRE} = \frac{1}{n} \sum_{i=1}^{n} \left(\frac{y_{pred,i} - y_{exp,i}}{y_{exp,i}} \right) \tag{4.12}$$

$$\text{MAE} = \frac{1}{n} \sum_{i=1}^{n} \left| \frac{y_{pred,i} - y_{exp,i}}{y_{exp,i}} \right| \tag{4.13}$$

The MRE and the MAE of the model is respectively $-4\,\%$ and $17\,\%$. The mean absolute error (MAE) is rather large, however the median of the absolute error is only $11\,\%$. This together with the better fit at larger pressure drops are explained by the large relative uncertainty on the low pressure drop measurements.

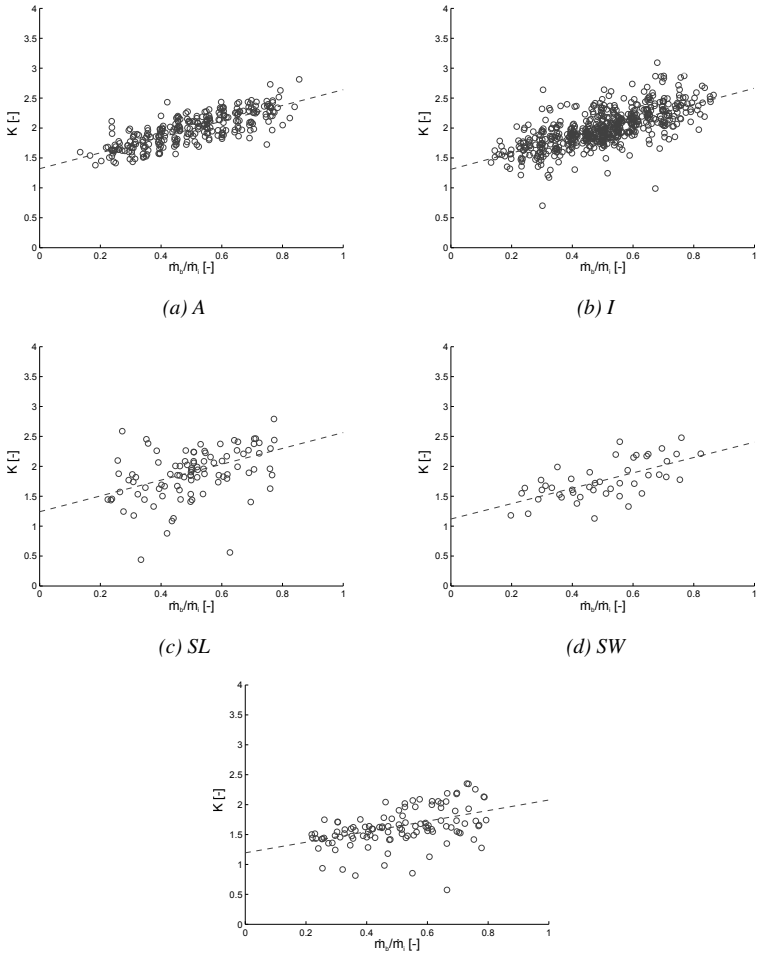

(a) A *(b) I*

(c) SL *(d) SW*

(e) SL+SW

Figure 4.17: Experimentally obtained K_{1i}-values (all refrigerants tested) as function of the mass fraction flowing towards the outlet grouped by the flow regimes.

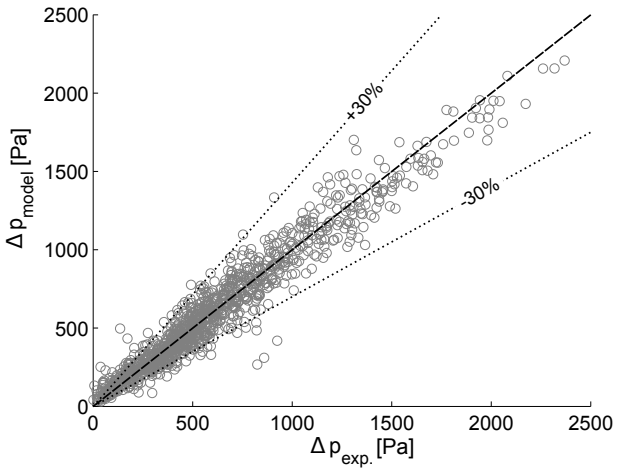

Figure 4.18: The pressure drop determined using the model as a function of the experimentally determined pressure drop.

4.4 Conclusion

To conclude, this chapter presented new phase distribution data. First, a suitable method to compare the results was proposed. Then, the different parameters influencing the phase distribution were discussed:

- A flow regime transition results in a strong change in phase distribution.
- The liquid has a decreasing preference of flowing to the branch with the lowest mass flow rate with increasing inlet superficial vapour velocity for an inlet superficial liquid velocity equal or higher than $0.2\,\mathrm{m/s}$.
- The liquid has an increasing preference of flowing to the branch with the lowest mass flow rate with increasing inlet superficial vapour velocity for an inlet superficial liquid velocity equal or lower than $0.1\,\mathrm{m/s}$.
- The phases are distributed more homogeneously with increasing density ratio.
- No influence of the liquid-vapour viscosity ratio on the phase distribution was observed.
- The maldistribution of the phases increases with increasing surface tension.
- The liquid phase has an increasing preference of flowing to the downward facing outlet due to gravity.

Finally, a model which predicts the pressure drops over the T-junction was proposed. Compared to the pressure drop model of El-Shaboury *et al.* [47], this new model is more accurate for this work's data and expands the prediction capabilities to other flow regimes. Using the insight obtained in this chapter, a new phase distribution model will be proposed in the next chapter.

5
Phase distribution model

This chapter initially evaluates the existing phase distribution models for the data included in this work. Then, in the next section, a new model is proposed which tries to mitigate the shortcomings of the existing models. The derivation of this new model is then discussed thoroughly. Finally, the new model is evaluated using the data gathered in this work and the data found in the literature.

5.1 Evaluation of the existing models

Before proposing a new model, it is necessary to test if the existing models can give decent results. In that case there is no need to propose a new one.

	mixture	**input**	**output**
Azzopardi *et al.* [57]	water-air	F_l	F_g
Azzopardi *et al.* [58]	water-air	F_g, E[1], orientation	F_l
Chien and Rubel [54, 73]	water-steam	F_g, x_1	F_l
Hong and Christon [53]	water-steam	$\dot{m}_1$, x_1, D, F_g, fluid properties	F_l
Ottens *et al.* [52] (ADS)	water-air	J_l, J_g, D, F_g, fluid properties	F_l
El-Shaboury *et al.* [47]	water-air	$\dot{m}_1$, x_1, $\dot{m}_3$, D, fluid properties, flowregime	F_l, F_g

Table 5.1: The existing models which were evaluated with their design mixture and their input and output parameters.

Table 5.1 displays the existing models which were evaluated together with their input and output parameters. Also, the mixture used to construct the model is given in the table. Note that the model of Hwang [56] was not included due to inability to converge for most inlet conditions. Furthermore, only the advanced double stream (ADS) model of Ottens *et al.* [52] is included in the table. The advanced double stream model is an extension of the original double stream model of Ottens *et al.* [52] with a reduced number of assumptions.

To evaluate the different models, an evaluation criterion has to be chosen. In this work the mean absolute deviation MAD and the mean deviation MD of the output parameter of the model are used:

$$\text{MD} = \frac{1}{n}\sum_{i=1}^{n}\left(y_{pred,i} - y_{exp,i}\right) \tag{5.1}$$

$$\text{MAD} = \frac{1}{n}\sum_{i=1}^{n}\left|y_{pred,i} - y_{exp,i}\right| \tag{5.2}$$

The output parameter of the existing models is either the liquid distribution F_l or the vapour distribution F_g. These parameters are always between 0 and 1. Furthermore, the measurement uncertainty of these parameters is constant and does not scale with their value. Hence, the MAD and MD was chosen over the

[1]The amount of liquid entrained in the vapour core as droplets. Has almost no influence on the model's outcome and was kept constant on 0.1.

more common MRE and MAE (equation 4.13 and 4.12) to avoid skewing of the results. For example, the MAD and MD of a low liquid distribution F_l value would be very large compared to a large one, even though the predictive quality is the same.

5.1.1 Evaluation using the data available in literature

First, the models found in the literature are evaluated using the water-air and the water-steam data found in the literature. In the following paragraph only the main conclusions of this evaluation will be given, the extended discussion can be found in appendix D.

In general, the largest prediction capability of the models is for the authors' own data. This is illustrated with table 5.2. The model of Chien and Rubel [54, 73] gives the best results for the data of Chien and Rubel [54, 73]. This is expected as the data was used to fit the model.

dataset		**# points**	**MD**	**MAD**	**MAD <0.05**
El-Shaboury *et al.* [47]	A	10	0.034	0.077	50 %
	SW	26	0.086	0.105	46 %
	S	15	−0.101	0.111	60 %
	All	51	0.020	0.102	51 %
Ottens *et al.* [52]	SW	35	0.043	0.106	49 %
	All	35	0.043	0.106	49 %
Chien and Rubel [54, 73]	A	136	−0.004	0.028	84 %
	All	136	−0.004	0.028	84 %
Hong and Christon [53]	A	16	0.000	0.078	38 %
	I	4	0.000	0.033	50 %
	SW	8	0.000	0.079	25 %
	SL+SW	10	0.000	0.028	80 %
	All	38	0.000	0.060	47 %
Mohamed *et al.* [37]	A	32	0.000	0.092	38 %
	SW	42	0.002	0.084	45 %
	S	21	0.000	0.090	33 %
	All	95	0.001	0.088	40 %
Mohamed *et al.* [42]	A	39	0.003	0.078	36 %
	SW	35	0.003	0.064	63 %
	S	22	0.000	0.065	45 %
	All	96	0.002	0.070	48 %
water-air data		277	0.010	0.087	46 %
water-steam data		174	−0.003	0.035	76 %
all data		451	0.005	0.067	57 %

Table 5.2: The prediction capabilities of the model of Chien and Rubel [54, 73] for the data found in the literature.

Secondly, most models have the best prediction capability for the two-phase mixture for which the model was designed, e.g. the water-steam models perform well for the water-steam data but fail to predict the water-air data. This can be observed if table 5.3 is compared with table 5.4. Hence, it appears that none of the models incorporates the influence of the fluid properties on the phase distribution.

Finally, based on the performed evaluation (see table 5.3), the model of El-Shaboury *et al.* [47] is recommended for water-air mixtures. For water-steam mixtures (see table 5.4), both the model of Chien and Rubel [54,73] and Azzopardi *et al.* [58] work well. Both models also give the best overall performance i.e. the water-air data and the water-steam data combined.

model	**MD**	**MAD**	**MAD <0.05**
Azzopardi *et al.* [57]	−0.013	0.081	51 %
Azzopardi *et al.* [58]	0.010	0.084	42 %
Ottens *et al.* [52] (ADS)	0.020	0.099	48 %
Hong and Christon [53] †	−0.006	0.125	22 %
Chien and Rubel [54, 73] †	0.010	0.087	46 %
El-Shaboury *et al.* [47] ⋆	0.026	0.059	74 %

†: model developed using water-steam data.
⋆: only the F_l values are considered.

Table 5.3: The predictive capabilities of existing phase distribution models for water-air mixtures (277 datapoints).

model	**MD**	**MAD**	**MAD <0.05**
Azzopardi *et al.* [57]	−0.016	0.068	40 %
Azzopardi *et al.* [58]	−0.014	0.038	73 %
Ottens *et al.* [52] (ADS)	0.136	0.240	18 %
Hong and Christon [53] †	0.035	0.068	41 %
Chien and Rubel [54, 73] †	−0.003	0.035	76 %
El-Shaboury *et al.* [47]	−0.143	0.323	0 %

†: model developed using water-steam data.
⋆: only the F_l values are considered.

Table 5.4: The predictive capabilities of existing phase distribution models for water-steam mixtures (174 datapoints).

5.1.2 Evaluation using the experimental data

To confirm the need for a new model, the models found in the literature are also evaluated using the data gathered in this work. The results of this evaluation are given in table 5.5 and 5.6 respectively grouped per refrigerant or flow regime.

According to table 5.5, the two models which had the best overall performance for the literature data (Azzopardi *et al.* [58] and Chien and Rubel [54, 73]), also

model	fluid	# datapoints	MD	MAD	MAD <0.05
Azzopardi *et al.* [57]	R32	394	0.028	0.059	45 %
	R134a	55	0.045	0.055	58 %
	R1234ZE	39	0.050	0.066	54 %
	R125	88	0.028	0.060	47 %
	All	576	0.031	0.060	47 %
Azzopardi *et al.* [58]	R32	394	−0.021	0.027	86 %
	R134a	55	−0.030	0.041	73 %
	R1234ZE	39	−0.036	0.068	49 %
	R125	88	−0.017	0.031	81 %
	All	576	−0.022	0.032	82 %
Chien and Rubel [54, 73]	R32	394	−0.019	0.027	85 %
	R134a	55	−0.030	0.036	84 %
	R1234ZE	39	−0.029	0.056	64 %
	R125	88	−0.018	0.029	76 %
	All	576	−0.020	0.030	82 %
Hong and Christon [53]	R32	394	−0.011	0.056	52 %
	R134a	55	−0.015	0.075	35 %
	R1234ZE	39	−0.004	0.046	72 %
	R125	88	−0.016	0.107	17 %
	All	576	−0.011	0.065	46 %
Ottens *et al.* [52] (ADS)	R32	394	−0.030	0.082	45 %
	R134a	55	−0.039	0.082	47 %
	R1234ZE	39	−0.019	0.058	62 %
	R125	88	−0.030	0.086	31 %
	All	576	−0.030	0.081	44 %
El-Shaboury *et al.* [47]	R32	123	−0.014	0.026	89 %
	R134a	5	−0.022	0.022	100 %
	R125	37	0.008	0.182	19 %
	All	165	−0.009	0.061	73 %

Table 5.5: The predictive capabilities of existing phase distribution models for the experimental data grouped by refrigerant.

give the best overall performance for the data of this work. Also the model of El-Shaboury *et al.* [47] performs rather well for R134a and R32 but fails to predict the R125 data. The reader should be aware of the fact that the model of El-Shaboury *et al.* [47] is limited to annular, stratified and stratified-wavy flows. Due to the absence of calibration coefficients, the model cannot be used for the other flow regimes. This inability of solving for certain flow regimes can lead to misleading results and conclusions, e.g. there is no data for R1234ze. Almost all the models are under-predicting the liquid phase distribution F_l by a small amount. Overall, the conclusion is that none of the models works well for all refrigerants. This is an indication that fluid property dependency is missing in the models.

Model	flow pattern	# datapoints	MD	MAD	MAD <0.05
Azzopardi *et al.* [57]	A	142	0.043	0.074	28 %
	I	304	0.032	0.056	51 %
	SL	52	0.022	0.048	73 %
	SW	23	0.014	0.061	43 %
	SL+SW	55	0.014	0.054	47 %
	All	576	0.031	0.060	47 %
Azzopardi *et al.* [58]	A	142	−0.026	0.029	89 %
	I	304	−0.024	0.031	82 %
	SL	52	−0.014	0.065	44 %
	SW	23	−0.013	0.017	96 %
	SL+SW	55	−0.013	0.020	93 %
	All	576	−0.022	0.032	82 %
Chien and Rubel [54, 73]	A	142	−0.026	0.032	80 %
	I	304	−0.022	0.028	83 %
	SL	52	−0.011	0.051	63 %
	SW	23	−0.011	0.021	96 %
	SL+SW	55	−0.012	0.019	98 %
	All	576	−0.020	0.030	82 %
Hong and Christon [53]	A	142	−0.025	0.071	33 %
	I	304	−0.007	0.070	43 %
	SL	52	0.000	0.071	46 %
	SW	23	−0.016	0.049	43 %
	SL+SW	55	−0.010	0.024	95 %
	All	576	−0.011	0.065	46 %
Ottens *et al.* [52] (ADS)	A	142	−0.048	0.101	35 %
	I	304	−0.020	0.076	46 %
	SL	52	−0.012	0.053	60 %
	SW	23	0.005	0.042	70 %
	SL+SW	55	−0.078	0.098	38 %
	All	576	−0.030	0.081	44 %
El-Shaboury *et al.* [47]	A	142	−0.010	0.065	73 %
	SW	23	−0.006	0.038	78 %
	All	165	−0.009	0.061	73 %

Table 5.6: The predictive capabilities of existing phase distribution models for the experimental data grouped by inlet flow regime.

Table 5.6 can be used to check if the models incorporate the influence of flow regimes. Most of the models works well for specific flow regimes but fail for other ones. Hence, most models do not incorporate the influence of the flow regime explicitly except for the model of El-Shaboury *et al.* [47]. Most models work best for the flow regime which was used for designing the models. For example, the model of Ottens *et al.* [52] works best for stratified-wavy flow, which was also the flow regime of their dataset.

5.2 Description of a new phase distribution model for horizontal impacting T-junctions

The new model will be based on three fundamental laws: conservation of mass, momentum and energy. In the following sections, these conservation laws will be applied to the control volume given in figure 5.1. By extending the control volume slightly into the branches of the T-junction, it is possible to assume the flow to be developed at the control volume boundaries.

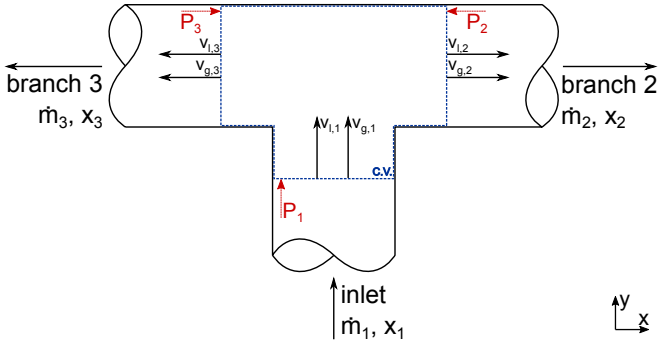

Figure 5.1: Control volume of the phase distribution model.

5.2.1 Conservation of mass

The conservation of mass is given by equation 5.3.

$$\cancel{\frac{\partial}{\partial t}\iiint_{c.v.} \rho \, dV} + \iint_{c.s.} \rho \left(\vec{v} \cdot \vec{n} \right) dA = 0 \tag{5.3}$$

The first term of this equation is the mass change of the control volume over time. This first term can be omitted because the model is a steady state model. The second term expresses the mass exchange through the control volume boundaries. Equation 5.3 can be rewritten for our control volume (figure 5.1) considering two separated phases to equation 5.4.

$$-\dot{m}_{l,1} - \dot{m}_{g,1} + \dot{m}_{l,2} + \dot{m}_{l,3} + \dot{m}_{g,2} + \dot{m}_{g,3} = 0 \tag{5.4}$$

The subscript l and g respectively refers to the liquid and vapour phase. Equation 5.4 can also be rewritten as equation 5.5.

$$-\dot{m}_1 + \dot{m}_2 + \dot{m}_3 = 0 \tag{5.5}$$

5.2.2 Conservation of momentum

The general expression for the conservation of momentum is given in equation 5.6.

$$\cancel{\frac{\partial}{\partial t} \iiint_{c.v.} \rho \vec{v} \, dV} + \iint_{c.s.} \vec{v} \, \rho \left(\vec{v} \cdot \vec{n} \right) dA = \sum \vec{F} \tag{5.6}$$

The first term in this equation is the change in momentum of the control volume over time. Hence, the first term can again be omitted because our model is a steady state model. The second term in equation 5.6 is the change in momentum through the control volume boundaries. The term on the right-hand side of the equation is the sum of all forces acting on the control volume. For the x-axis (figure 5.1), the acting forces are: the pressure force, the gravity force, the friction force on the wall and the surface tension on the wall. This model will be designed for macroscale tubes. According to several authors [31, 35, 36], the surface tension forces are negligible compared to the frictional, inertial and gravity forces for macroscale tubes. Hence, the surface tension force will be neglected. Furthermore, due to the small size of the control volume, it is assumed that the friction force is negligible. Considering the assumptions described above, equation 5.6, applied to the x-axis of the control volume (figure 5.1), results in the equation 5.7.

$$\begin{aligned} \dot{m}_{l,2} \, v_{l,2} + \dot{m}_{g,2} \, v_{g,2} - \dot{m}_{l,3} \, v_{l,3} - \dot{m}_{g,3} \, v_{g,3} = \\ \underbrace{(P_3 - P_2)}_{①} \, A_c + \cancel{\sin(\theta) \, g \, \rho \, \xi_{c.v.}} \end{aligned} \tag{5.7}$$

In this equation, v is the real velocity of the phase, A_c is the cross-sectional area of the tube, θ is the inclination of the T-junction (see figure 2.5), g is the standard gravity and $\xi_{c.v.}$ is the volume of the control volume. The real liquid and vapour velocity of branch i is respectively calculated using equation 5.8 and 5.9.

$$v_{l,i} = \frac{\dot{m}_{l,i}}{\rho_l \, A_c \, (1 - \epsilon)} \tag{5.8}$$

$$v_{g,i} = \frac{\dot{m}_{g,i}}{\rho_g \, A_c \, \epsilon} \tag{5.9}$$

The void fraction ϵ is calculated using the drift-flux model of Rouhani-Axelsson [25] given in equation 2.7.

In the first instance, the gravity term can be omitted because the model will be developed for a horizontal T-junction. In section 5.4 the model will be extended to an inclined T-junction.

The pressure difference over the T-junction, indicated as ①, cannot be determined directly from the flow and has to be modelled. This term will be used to fit the model to the experimental data.

Pressure difference term As discussed in chapter 4.3, the pressure drop over a junction for a homogeneous flow can be described using the Bernoulli equation with an irreversible term. This irreversible term is often represented as a constant K times the inlet kinetic energy. Hence, the pressure drop over the junction from inlet to outlet i can be written as:

$$\Delta P_{1i} = \hat{\rho}_1 \left(\frac{\hat{v}_2^2}{2} - \frac{\hat{v}_1^2}{2} \right) + K_{1i} \hat{\rho}_1 \frac{\hat{v}_1^2}{2} \tag{5.10}$$

$\hat{\rho}$ is the homogeneous inlet density defined by equation 4.9 and $\hat{v}$ is the homogeneous velocity defined by equation 4.10. As discussed in chapter 4.3, the constant K_{1i} is related to the total mass fraction ratio to outlet i and is the same for both outlets:

$$K_{1i} = a_1 \frac{\dot{m}_i}{\dot{m}_1} + a_2 \tag{5.11}$$

The terms a are constants which have to be fitted.

The term ① can thus be rewritten as equation 5.12 with a_1 being a fitting constant.

$$\begin{aligned} ① &= P_3 - P_2 \\ &= (P_1 - \Delta P_{13}) - (P_1 - \Delta P_{12}) \\ &= \Delta P_{12} - \Delta P_{13} \\ &= \hat{\rho}_1 \left(\frac{\hat{v}_2^2}{2} - \frac{\hat{v}_3^2}{2} \right) + (K_{12} - K_{13}) \hat{\rho}_1 \frac{\hat{v}_1^2}{2} \\ &= \hat{\rho}_1 \left(\frac{\hat{v}_2^2}{2} - \frac{\hat{v}_3^2}{2} \right) + \left(a_1 \frac{\dot{m}_2 - \dot{m}_3}{\dot{m}_1} \right) \hat{\rho}_1 \frac{\hat{v}_1^2}{2} \end{aligned} \tag{5.12}$$

In equation 5.12, it is assumed that the flow is homogeneous which is often not the reality. Furthermore, in the experiments, an effect of droplet entrainment was observed. Hence, a correction term is added to the expression of the pressure difference $P_3 - P_2$:

$$\begin{aligned} P_3 - P_2 = \hat{\rho}_1 \left(\frac{\hat{v}_2^2}{2} - \frac{\hat{v}_3^2}{2} \right) + \left(a_1 \frac{\dot{m}_2 - \dot{m}_3}{\dot{m}_1} \right) \hat{\rho}_1 \frac{\hat{v}_1^2}{2} \\ + a_2 \left(v_{g,2} - v_{g,3} \right) \dot{m}_{l,1} We_l \end{aligned} \tag{5.13}$$

The amount and the direction of the droplet entrainment is mainly affected by the vapour velocity difference $v_{g,2} - v_{g,3}$. The size of the droplets and the formation of droplets is linked with the Weber number. The liquid Weber number We_l is defined as:

$$We_l = \frac{\rho_l \left(v_{l,2} - v_{l,3} \right)^2 \bar{D}_{droplet}}{\sigma} \tag{5.14}$$

With $\bar{D}_{droplet}$ being the mean droplet diameter. This diameter is not known and is thereby assumed to be constant. Hence, it will combined with the fitting constant a_2.

In the literature [56] and also in the experimental results, it was noted that the phases are only distributed evenly over the branches of a horizontal impacting T-junction when the total mass flow rate is split evenly over its outlets. If an equal total mass flow split and equal phase split over the two outlets is entered in equation 5.7, the equation equals to zero. Hence, the current form of the conservation of momentum obeys the observed experimental behaviour.

Finally, the constants a_1 and a_2 were fitted using the experimental data of all the refrigerants. As seen in chapter 4, the phase distribution is influenced strongly by the inlet flow regime. Hence, the constants a_1 and a_2 are flow regime dependant and are given in table 5.7. Figure 5.2 shows the calculated values of the term ① as a function of their experimental obtained counterpart.

	a_1	a_2
A	2.70 ± 0.03	-0.003 ± 0.003
I	2.62 ± 0.02	-0.009 ± 0.002
SL	2.72 ± 0.09	0.03 ± 0.02
SW	2.84 ± 0.05	0.10 ± 0.07
SL+SW	2.66 ± 0.04	0.05 ± 0.02

Table 5.7: Fitting constants of the momentum equation.

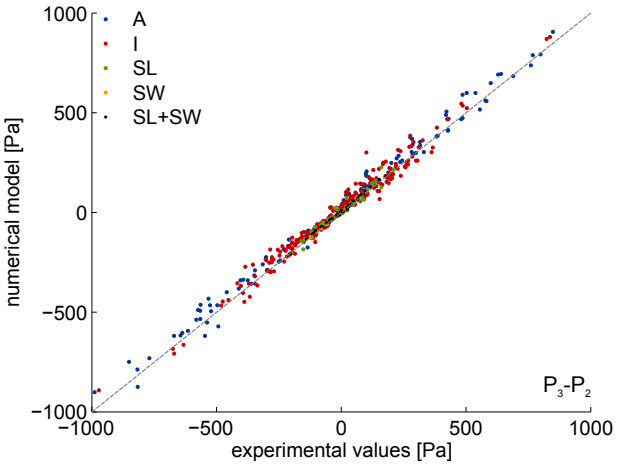

Figure 5.2: The model's values of the term ① as function of the experimental values for all refrigerants.

5.2.3 Conservation of energy

The general expression for the conservation of energy is given in equation 5.15.

$$\cancel{\frac{\partial}{\partial t}\iiint_{c.v.}\left(\cancel{gy}+\frac{v^2}{2}+u\right)\rho\,dV} + \iint_{c.s.}\left(\cancel{gy}+\frac{v^2}{2}+u+\frac{P}{\rho}\right)\rho\left(\vec{v}\cdot\vec{n}\right)dA = \cancel{\frac{\delta Q}{dt}}-\cancel{\frac{\delta W_s}{dt}}-\cancel{\frac{\delta W_\mu}{dt}} \tag{5.15}$$

The first term in equation 5.15 is the change of energy over time. Again, this term can be omitted because this model is a steady state model. The second term is the energy transfer through the control volume boundaries. It is assumed that the change in height of a phase within the tube is negligible compared to the change in kinetic energy and internal energy. This means that the term of potential energy is omitted from the second term. The first term at the right-hand side of the equation $\frac{\delta Q}{dt}$ is the heat transferred from the environment to the control volume. This term can be omitted because it is assumed that the T-junction is perfectly insulated and thus adiabatic. The second term at the right-hand side of the equation $\frac{\delta W_s}{dt}$ is the shaft work. Due to the absence of shaft work, this term can also be omitted. The last term $\frac{\delta W_\mu}{dt}$ is the viscous work. Because the friction force is neglected in the momentum equation, this work is assumed to be equal to zero.

When applied to the control volume (figure 5.1), it results in equation 5.16. In equation 5.16, H is the enthalpy.

$$\begin{aligned}&\dot{m}_{l,1}\left(H_{l,1}+\frac{v_{l,1}^2}{2}\right)-\dot{m}_{l,2}\left(H_{l,2}+\frac{v_{l,2}^2}{2}\right)-\dot{m}_{l,3}\left(H_{l,3}+\frac{v_{l,3}^2}{2}\right)\\&+\dot{m}_{g,1}\left(H_{g,1}+\frac{v_{g,1}^2}{2}\right)-\dot{m}_{g,2}\left(H_{g,2}+\frac{v_{g,2}^2}{2}\right)-\dot{m}_{g,3}\left(H_{g,3}+\frac{v_{g,3}^2}{2}\right)=0\end{aligned} \tag{5.16}$$

5.2.4 Model implementation

Previous paragraphs described the equations concerning the model. In this paragraph, the implementation of the model will be explained. First, the model takes as input parameters the inlet mass flow rate $\dot{m}_1$, the inlet vapour quality x_1, the inlet saturation temperature T_{sat}, the inlet flow regime, the tube diameter D and the mass flow rate in outlet 2 $\dot{m}_2$. The output parameters of the model are the mass flow rate in branch 3 $\dot{m}_3$ and the vapour qualities in branch 2 (x_2) and branch 3 (x_3). Finally, the solution strategy of the model is described in figure 5.3.

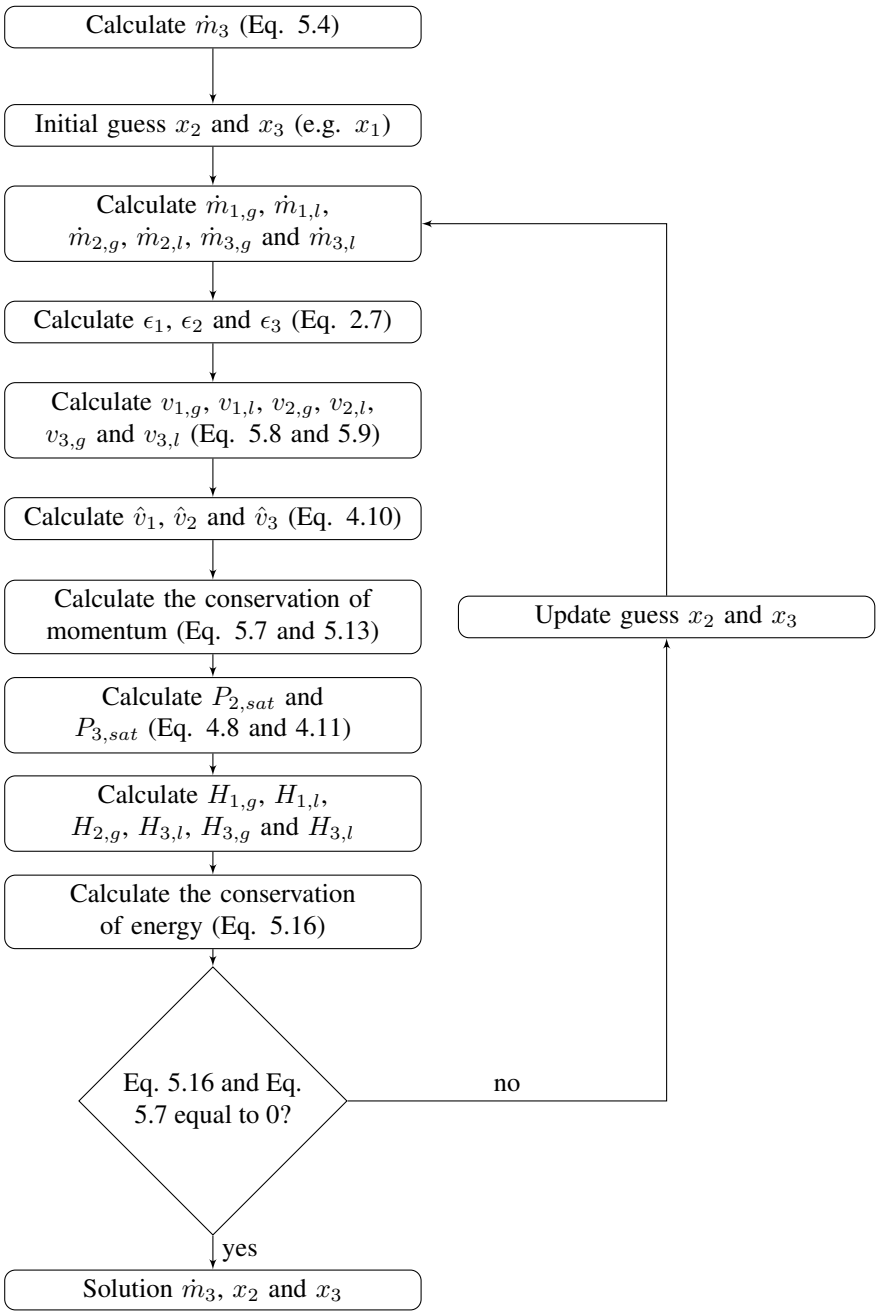

Figure 5.3: The solving algorithm of the model.

5.3 Validation of horizontal phase distribution model

To validate the new phase distribution model, the predictions of the model are compared with the experimental results. In table 5.8, the predicted liquid mass fraction F_l in outlet 2 is compared with its experimental value. The results are grouped per refrigerant.

fluid	**# datapoints**	**MD**	**MAD**	**MAD <0.05**
R32	394	0.010	0.017	94 %
R134a	55	0.011	0.016	96 %
R1234ze	39	0.008	0.009	100 %
R125	88	0.006	0.013	100 %
All	576	0.010	0.016	96 %

Table 5.8: The predictive capability of the new phase distribution model (F_l) for the data gathered in this work grouped by refrigerant.

According to the table, the new phase distribution model performs equally well for every refrigerant tested. Further, the average deviation (MAD) is of the order of 0.02 which equals to the experimental uncertainty on the liquid mass fraction F_l measurements. However, on average, the model overpredicts the liquid mass fraction F_l for all refrigerants.

flow regime	**# datapoints**	**MD**	**MAD**	**MAD <0.05**
A	142	0.018	0.023	91 %
I	304	0.008	0.013	98 %
SL	52	0.003	0.006	100 %
SW	23	0.003	0.033	74 %
SL+SW	55	0.004	0.015	100 %
All	576	0.010	0.016	96 %

Table 5.9: The predictive capability of the new phase distribution model (F_l) for the experimental data grouped by inlet flow regime.

Table 5.9 and figure 5.4 compare the predicted liquid mass fraction F_l in outlet 2 to its experimental value but this time grouped per flow regime. According to the table, the new phase distribution model performs equally well for most flow regimes. It is clear that the model does not perform excellently for the stratified-wavy flows. First of all, the available data used to fit was fairly limited. Moreover, this flow regime is related to the stratified regime, which has significantly different spatial distribution of the phases than the other regimes tested.

In figure 5.4, some outliers can be identified. These outliers have larger experimental uncertainties than other measurements. Probably these experiments

are not accurate. When these points are excluded, it has little effect on the fitting constants of the model.

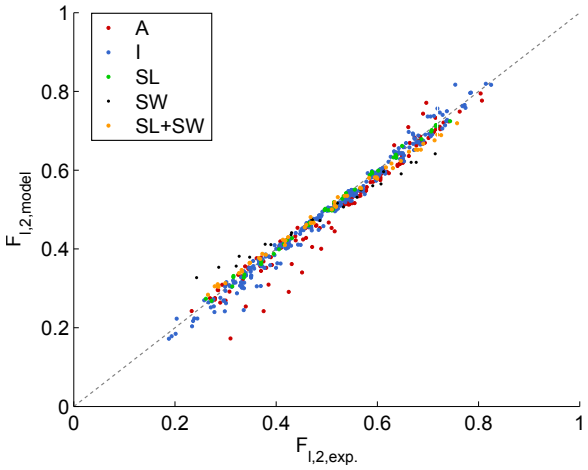

Figure 5.4: The predicted liquid fraction F_l as function of the experimental value for the data of this work.

For the sake of completeness, the predicted vapour mass fraction F_g in outlet 2 is also compared to its experimental value. These results can be found in figure 5.5.

fluid	**# datapoints**	**MD**	**MAD**	**MAD <0.05**
water-steam	174	0.037	0.064	55 %
water-air	184	−0.018	0.068	59 %

Table 5.10: The predictive capability of the new phase distribution model for the experimental data grouped by refrigerant.

The new model was also evaluated with the data found in the literature. Table 5.10 compares the predicted liquid mass fraction F_l in outlet 2 to its experimental value for the data found in the literature. The predicted liquid fraction F_l as function of the experimental value for the water-steam data [53,54,73] is also shown in figure 5.6.

The predictive power of the model for the water-steam and water-air data is still reasonable. However, the prediction is much worse than for the refrigerants. Furthermore, for 93 of the 277 inlet conditions of the water-air data, the model did not even give a result. Based on the evaluation of the different two phase mixtures, one can conclude that still some things are missing in the model.

Further, the model is very sensitive to the pressure drop model. Especially the conservation of momentum is very sensitive to the pressure drop model. On the

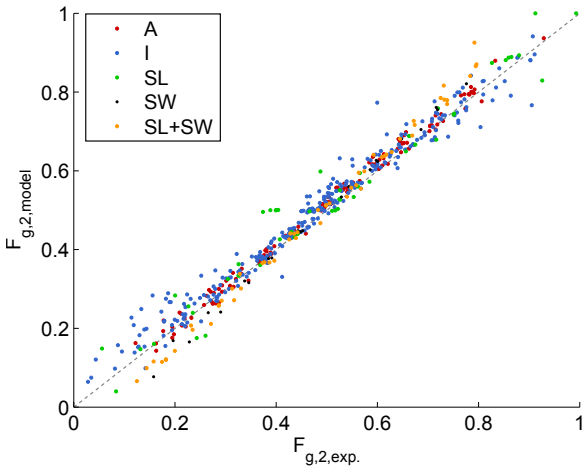

Figure 5.5: The predicted liquid fraction F_g as function of the experimental value for the data of this work.

other hand, the conservation of energy is not sensitive at all. If you consider that the current pressure drop model is a very basic model and was fitted using the data of this work, this model will not be very accurate for other two phase mixtures. For example, comparing the pressure drop model of this work to the limited pressure data of El-Shaboury *et al.* [47], shows deviations with an average factor of 1.7. This difference in pressure drop has already a huge impact on the outcome of the phase distribution model.

Finally, currently the average droplet diameter is assumed to be constant. In reality, this diameter will vary.

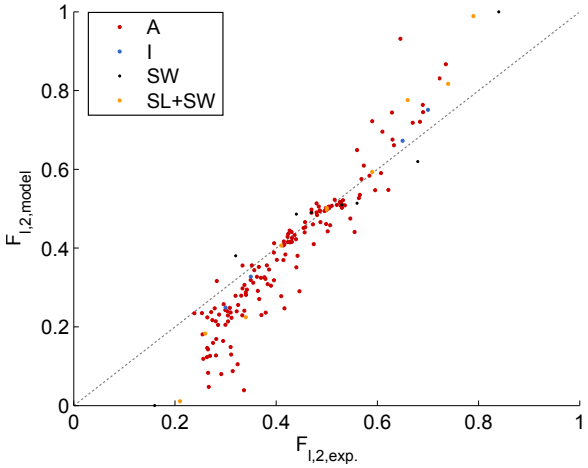

Figure 5.6: The predicted liquid fraction F_l as function of the experimental value for the water-steam data [53, 54, 73].

5.4 Extension to inclined T-junctions

In this section, the model described in section 5.2, which was designed for horizontal impacting T-junctions, will be extended to inclined impacting T-junctions. To extend the model, the gravity term in equation 5.7 will not be omitted.

First of all, the gravity has the largest influence on the liquid phase. Hence, only the gravity force on the liquid phase is kept. The volume of the junction is related to the third power of the diameter. From the experimental result also a dependency of the liquid Reynolds number of the inlet flow was observed. Finally, this term should equal zero if the inclination angle θ equals zero. Considering the assumption above, the gravity term can be rewritten to equation 5.17. The constants b_1 and b_2 are fitting parameters which were fitted using the experimental data. These constants b_1 and b_2 are equal to 151.3 ± 32 and 1.37 ± 0.09, respectively.

$$\begin{aligned} &\sin(\theta)\ g\ (\rho_l\,\xi_{junction,l} + \rho_g\,\xi_{junction,g}) \\ \approx &\sin(\theta)\ \left(b_1 - b_2\,\rho_l\,Re_{l,1}\,D^3\,g\right) \\ \approx &\sin(\theta)\ \left(151.3 - 1.37\,\rho_l\,Re_{l,1}\,D^3\,g\right) \end{aligned} \tag{5.17}$$

The liquid Reynolds number of the inlet is defined as:

$$Re_{l,1} = \frac{\rho_l\,v_{l,1}\,D}{\mu_l} \tag{5.18}$$

fluid / flow regime	**# datapoints**	**MD**	**MAD**	**MAD <0.05**
R32	81	−0.002	0.012	100 %
R125	39	0.000	0.011	100 %
A	13	0.005	0.017	100 %
I	83	−0.001	0.010	100 %
SL	24	−0.002	0.011	100 %
All	120	−0.001	0.011	100 %

Table 5.11: The predictive capability of the new phase distribution model (F_l) for this work's inclined data.

Table 5.11 and figure 5.7 compare the predicted liquid mass fraction F_l in outlet 2 to its experimental value for the inclined data of this work. The table contains both the grouping per refrigerant as per flow regime. Conversely, the predictive quality of the liquid mass fraction F_l is in the same order as the horizontal model. Hence, the additional step of adding the influence of the inclination is modelled correctly for the liquid mass fraction F_l. Contrary, the predictive quality of the vapour mass fraction F_g is less accurate as seen in figure 5.8. The MAD for the

vapour mass fraction F_g is 0.04 and only $68\,\%$ of the predictions have a MAD smaller than 0.05. The MAD of the inclined model is almost double of the one for the horizontal model (0.26).

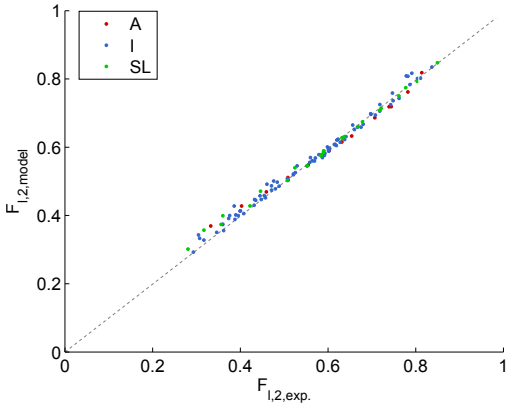

Figure 5.7: The predicted liquid fraction F_l as function of the experimental value for this work's inclined data.

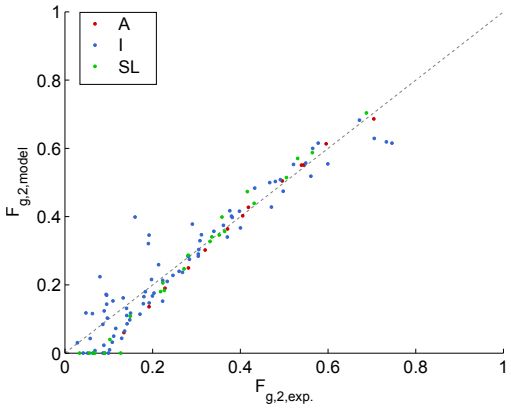

Figure 5.8: The predicted vapour fraction F_g as function of the experimental value for this work's inclined data.

5.5 Conclusions

This chapter first evaluated the existing phase distribution models. Currently, none of the models could predict the phase distribution perfectly. Most of them performed well for a specific flow regime and or specific two-phase mixture.

Based on the insights gained in the previous chapter, a new phase distribution model for refrigerants was proposed. This model is based on three basic laws: conservation of mass, momentum and energy. The new model is then evaluated using the data gathered in this work and the data from literature. The new model works well for the data of this work and acceptable for the water-steam and water-air data. Further, some shortcomings of the model are described.

Finally, the model is extended to inclined impacting T-junctions. The inclined model is able to predict the liquid mass fraction F_l correctly for the data of this work. However, the prediction of the vapour mass fraction F_g is less accurate. The MAD is almost double of the one of the horizontal model.

6 Conclusion

6.1 Conclusion

The main objective of this work is to get a better understanding of the phase maldistribution in tubular distributors. In first instance, the work is confined to the distribution over two parallel circuits. In this case the tubular distributor can be reduced to an impacting T-junction.

The main objective of this work can be split up in two parts: increase the understanding of the parameters influencing the phase distribution and develop a phase distribution model for refrigerants. Both objectives are supported by experimental measurements. Hence, a new test rig was designed and built to measure the phase distribution of refrigerants (R32, R125, R134a and R1234ze) over an impacting T-junction.

To increase the understanding of the parameters influencing the phase distribution, this work focused on filling the gaps in the literature. First of all, El-Shaboury *et al.* [47] and Elazhary *et al.* [40, 41] found an inconsistency in the trends in the vicinity of a flow regime transition. The influence of the inlet superficial velocities has a sudden jump at a flow regime transition. However, within all flow regimes the trend was equal. For example, the liquid phase has a decreasing preference of flowing to the branch with the lowest mass flow rate with increasing inlet superficial vapour velocity for an inlet superficial liquid velocity equal or higher than $0.2\,\mathrm{m/s}$ and for each flow regime. In contrast, for an inlet superficial liquid velocity equal or lower than $0.1\,\mathrm{m/s}$, the liquid has an increasing

preference of flowing to the branch with the lowest mass flow rate with increasing inlet superficial vapour velocity.

Secondly, the knowledge of the fluid properties' influence on the phase distribution over an impacting T-junction is rather limited. Most experimental work in literature is executed with a water-air mixture. Furthermore, if the influence of the fluid properties is elaborated upon, it was done in a micro-channel T-junction. The governing physics in micro-channels are different from the ones in macro-channels. The influence of three fluid properties was investigated in this work. The phases are distributed more homogeneously with increasing density ratio ρ_g/ρ_l. No influence of the vapour-liquid viscosity ratio μ_g/μ_l on the phase distribution was observed. The maldistribution of the phases increases with increasing surface tension. It is hypothesized that this is because a lower surface tension results in smaller droplets and more entrainment of liquid in the gas phase, which tends to homogenize the flow.

Finally, the influence of the inclination angle is only studied in the literature for water-air mixtures or when full separation occurs. This work generated new data and studied the interaction between the inclination angle and the fluid properties. Consistent with the literature, the liquid phase has an increasing preference of flowing to the downward facing outlet due to gravity. However, the quantitative results are significantly different from the ones of the water-air mixtures. For an annular flow, the influence of the inclination angle for a refrigerant flow is significantly larger than for a water-air flow.

The second objective is developing a phase distribution model for refrigerants. First the existing phase distribution models were evaluated. Most of them perform only well for a specific flow regime and/or a specific two-phase mixture. None of the models was able to predict the phase distribution of the dataset of this work perfectly.

Hence, based on the insights gained from the experimental data, a new phase distribution model for refrigerants was proposed. This model is based on three basic laws: conservation of mass, momentum and energy. These laws contain the pressure drop over the T-junction. Therefore a pressure drop correlation for the dataset of this work was made.

The new model is then evaluated using the data of this work and the data from the literature. The new model works well for the refrigerant data and acceptable for the water-steam and water-air data. Some of the shortcomings of this new model were described.

Finally, the phase distribution model is extended to inclined impacting T-junctions. The inclined model is able to predict the liquid mass fraction F_l correctly for this work's data but the prediction of the vapour mass fraction F_g is less accurate.

6.2 Future work

In chapter 4, the hypothesis of droplet entrainment is put forward in order to explain the experimental results. Currently, there is no hard evidence proving this hypothesis to be correct. This could be verified using a visual method e.g. film the flow in a transparent T-junction. Note, this is only possible if the liquid layer on the wall is not too thick. On top of this, the phase distribution model could be improved by using a mean droplet size model. By visualising the droplet, such a model could be made.

In the discussion of the evaluation of the new phase distribution model, it became apparent that the model is very sensitive to the pressure term. Moreover, the current pressure drop model could not predict the pressure drop of water-air mixtures correctly. To improve the current pressure drop model, more data for different mixtures, tube diameters,... is necessary.

Finally, to be more relevant to tubular distributors, this work should be expanded to impacting Y-junctions. This enables to investigate the influence of opening angle on the phase distribution.

A Uncertainty Analysis

This chapter first describes the accuracies of the measurement equipment. Then the uncertainty on the thermophysical properties obtained by CoolProp [74] is discussed. Further, the method used to post-process the raw data and the accompanying propagation of the uncertainty is described. The uncertainty analysis of this work is based on the book of Taylor [75]. Finally, at the end of this chapter, the P& ID of the experimental setup is included.

A.1 Measurements

A.1.1 Temperature measurement

The temperature measurements in the experimental setup are conducted using K-type thermocouples. The thermoelectric voltages of the thermocouples are read out by a precision data-acquisition unit (*Keithley 2700*).

Due to the dissimilarity in material of the thermocouple wires and the connections of the data-acquisition unit, an extra thermoelectric voltage is induced. This voltage depends on the varying ambient temperature. To eliminate this deviation on the measured thermoelectric voltage, a reference thermocouple at a stable and precisely known temperature is used to correct this error. This reference thermocouple is held at 0.01 ± 0.0005 °C using a Triple Point of Water Cell (TWC, *Fluke 5901B*). A TWC is a glass cell filled with a *Vienna Standard Mean Ocean Water* (VSMOW) under vacuum conditions. At the physical triple point of 0.01 °C, water can exist at three phases (liquid, gas and solid). As long as there are three

phases in the cell, the TWC is at his triple point. To keep the TWC at the triple point state for up to 6 hours, a maintenance apparatus (*Fluke 9210*) is used.

Each thermocouple can also have small differences in the metal composition due to production variability. To eliminate this error, each thermocouple is calibrated. During the calibration process, the thermocouples are placed in a dry-block calibrator (*Druck DBC 150*). To improve thermal contact between the thermocouples and the calibrator, water or methanol is used. Besides the thermocouples also an accurate Pt-100 thermometer (*Fluke 1523* with an absolute accuracy of $0.064\,°C$) is placed in the calibrator. When the temperature of the calibrator is stabilised (± 1 hour), 100 measurements are taken at a frequency of $1\,Hz$.

Using these 100 measurements, a 4^{th} order calibration curve (equation A.1) is made using least square polynomial regression. The standard error and prediction interval of a k^{th} order polynomial curve is respectively given in equation A.2 and A.3 [76]. The $t_{0.95,n-(k+1)}$ is the student's t-statistic for $n-(k+1)$-degrees of freedom and a probability of $95\,\%$.

$$T = a_4\Delta V^4 + a_3\Delta V^3 + a_2\Delta V^2 + a_1\Delta V + a_0 \tag{A.1}$$

$$SE = \sqrt{\frac{1}{n-(k+1)}\sum_{i=1}^{n}\left[y_i - \left(a_k x_i^k + a_{k-1}x_i^{k-1} + ... + a_1 x_i^1 + a_0\right)\right]^2} \tag{A.2}$$

$$PI = t_{0.95,n-(k+1)}\text{SE}\sqrt{1 + \frac{1}{n} + \frac{\left(\Delta V - \bar{\mu}_{\Delta V,curve}\right)^2}{(n-1)\,\bar{\sigma}^2_{\Delta V,curve}}} \tag{A.3}$$

$$\delta T = \sqrt{PI^2 + \delta^2_{Pt100}} \tag{A.4}$$

Combining all the uncertainties on the temperature measurement using equation A.4 results in an average and maximum uncertainty on the temperature of respectively $0.07\,°C$ and $0.09\,°C$.

A.1.2 Pressure measurement

The accuracy of a pressure sensor is often specified by three uncertainty values: accuracy, thermal stability and long-term stability. These uncertainties are typically expressed as a percentage of the measurement range. The accuracy of the pressure sensor incorporates the effects of non-linearity, hysteresis and repeatability under reference conditions. The uncertainty due to thermal effects is specified as a value for a certain temperature range. The long-term stability

is due to ageing of the sensor and is often given by the maximum drift per year. Because the pressure sensors are recalibrated every year, the drift is not taken into account.

P&ID	type	range	accuracy	thermal stability
2-02	GEMS 2200	-1 - 39 barg	0.25 %	1.5 %
2-17	GE DRUCK PMP 4070	0 - 40 bara	0.08 %	2 %
2-19	GEMS 2200	-1 - 39 barg	0.25 %	1.5 %
4-17	GE DRUCK PMP 5076	-0.1 - 1.9 bar	0.2 %	1.5 %
4-19	GE DRUCK PMP 4070	0 - 40 bara	0.08 %	2 %
4-21	GE DRUCK PMP 4070	0 - 40 bara	0.08 %	2 %
	E+H Deltabar S PMD75	0 - 1 kPa	0.09 %	0.36 %
	E+H Deltabar S PMD75	0 - 10 kPa	0.075 %	0.2 %

Table A.1: Uncertainty of Pressure Transducers

A.1.3 Flow measurement

Both the water mass flow meter and the refrigerant mass flow meter in the preheater is a Bronkhorst Cori-Flow M55 ABD-55-0. The refrigerant flow meter was calibrated for a range of 10-200 kg/h, the water flow meter for a range of 25-500 kg/h. The uncertainty of these meters is given by a zero stability of 0.1 kg/h plus 0.1 % of the measured mass flow rate.

The refrigerant mass flow rates of the two branches of the test section are each measured by a Krohne OPTIMASS 6400 S10. The uncertainty of the Krohne OPTIMASS 6400 S10 is given by a zero stability of 0.06 kg/h plus 0.35 % of the measured mass flow rate.

A.1.4 Electrical power measurements

The electrical power delivered to the electrical heaters is determined by measuring the current through and the voltage over the electrical heater. The voltage and current measurements are done by the electronic voltage source (Elektro-Automatik PSI 5200-10 A) powering the electrical heater. The uncertainty on the voltage and the current measurement is respectively 200 mV and 20 mA. Using equation A.5 and A.6, the power and its uncertainty can be determined based on the current and voltage measurement.

$$P_{\text{electr.}} = V \cdot I \tag{A.5}$$

$$\delta P_{\text{electr.}} = \sqrt{(\delta V \cdot I)^2 + (V \cdot \delta I)^2} \tag{A.6}$$

A.2 Thermophysical properties

All thermophysical properties are calculated using CoolProp [74]. CoolProp is an Open-Source Thermophysical Property Library written in C++. The uncertainty of the values given by CoolProp are found in the references of the formulas used in CoolProp. The uncertainty of the enthalpy value was never given, but it is customary to estimate the uncertainty of the enthalpy to be half of the one of the isobaric heat capacity [77]. The relative uncertainties used in this uncertainty analysis are tabulated in table A.2.

	$\delta\rho_l$	$\delta\rho_g$	$\delta C_{p,l}$	$\delta C_{p,g}$	δh
Water [78]	$0.001\,\%$	$0.05\,\%$	$0.1\,\%$	$0.2\,\%$	$0.05\,\%$
R32 [79]	$0.05\,\%$	$0.1\,\%$	$0.5\,\%$		$0.25\,\%$
R134a [80]	$0.06\,\%$	$0.05\,\%$	$1\,\%$		$0.5\,\%$
R410a [81, 82]	$0.2\,\%$	$0.1\,\%$	$1\,\%$		$0.5\,\%$
R1234yf [83]	$0.1\,\%$	$0.5\,\%$	$5\,\%$		$2.5\,\%$
R1234ze [84]	$0.1\,\%$	$0.1\,\%$	$5\,\%$		$2.5\,\%$
R125 [84]	$0.1\,\%$	$0.1\,\%$	$0.5\,\%$		$0.25\,\%$

Table A.2: The uncertainty of the thermophysical properties given by Coolprop for different fluids.

A.3 Processing raw data and its uncertainty

A.3.1 Mass flux

In the literature the mass flux G is often used instead of the mass flow rate. The mass flux can be determined by equation A.7 with $\dot{m}$ the mass flow rate of the refrigerant and d_i the inner diameter of the tube.

$$G = \frac{\dot{m}}{A} = \frac{4\,\dot{m}}{\pi\,D_i^2} \tag{A.7}$$

The uncertainty of the mass flux, which is given by equation A.8, depends on the mass flow rate and the tube diameter.

$$\delta G = \sqrt{\left(\frac{4}{\pi\,D_i^2}\,\delta\dot{m}\right)^2 + \left(\frac{-8\,\dot{m}}{\pi\,D_i^3}\,\delta D_i\right)^2} \tag{A.8}$$

In general, the relative uncertainty on the mass flux G is always below $2\,\%$.

A.3.2 Heat transferred to the refrigerant in the preheater

To determine the vapour quality after the preheater, the heat input to the refrigerant in the preheater has to be known. The preheater consists of multiple tube-in-tube heat exchangers which are placed in series. For each of these heat exchangers the heat transferred to the refrigerant is calculated using the method described below (eq. A.9 to A.28). Afterwards the total heat transferred is calculated using equations A.29 and A.30.

The heat transferred to the refrigerant in a tube-in-tube heat exchanger is given by the energy change of the hot water in the annulus minus the heat losses to the environment.

$$Q_{PH,i} = \dot{m}_w \cdot c_{p,w} \cdot (T_{w,in} - T_{w,out}) - Q_{loss} \tag{A.9}$$

The uncertainty of this amount of heat transferred is given by following equation.

$$\delta Q_{PH,i} = \sqrt{\begin{array}{l}(\delta \dot{m}_w \cdot C_{p,w} \cdot (T_{w,in} - T_{w,out}))^2 \\ \quad + (\delta C_{p,w} \cdot \dot{m}_w \cdot (T_{w,in} - T_{w,out}))^2 \\ \quad\quad + (\delta T_{w,in} \cdot \dot{m}_w \cdot C_{p,w})^2 \\ \quad\quad\quad + (\delta T_{w,out} \cdot \dot{m}_w \cdot C_{p,w})^2 \\ \quad\quad\quad\quad + (Q_{loss})^2\end{array}} \tag{A.10}$$

The uncertainty of the isobaric heat capacity is the sum of the uncertainty of CoolProp and the uncertainty of average water temperature. This last one is determined by calculating the variation of the isobaric heat capacity due to uncertainty of the temperature measurement.

$$\begin{aligned}\delta c_{p,w} &= \sqrt{\delta C^2_{p,w,\text{CoolProp}} + \delta C^2_{p,w,T}} \\ &= \sqrt{\delta C^2_{p,w,\text{CoolProp}} + \left(\frac{\delta C_{p,w,T+\delta T} - \delta C_{p,w,T-\delta T}}{2}\right)^2}\end{aligned} \tag{A.11}$$

The heat loss to the environment is calculated using a one-dimensional model which is depicted in figure A.1. The model uses the electrical resistance analogy. The model calculates the heat loss based on the measured water and ambient air temperature and the known thermal resistances.

$$Q_{loss} = \frac{T_a - T_w}{R_i + R_{cu} + R_{insul.} + R_o} \tag{A.12}$$

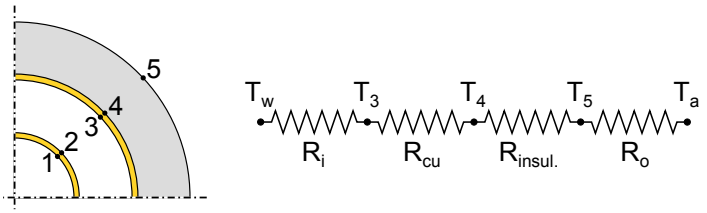

Figure A.1: A schematic representation of the model used to estimate the heat losses to the environment at the preheater. (refrigerant; 1-2: inner tube wall; 2-3: hot water; 3-4: outer tube wall; 4-5: insulation; ambient air)

$$\delta Q_{loss} = \sqrt{\begin{aligned}&\left(\frac{\delta T_a}{R_i + R_{cu} + R_{insul.} + R_o}\right)^2 \\ &+\left(\frac{\delta T_w}{R_i + R_{cu} + R_{insul.} + R_o}\right)^2 \\ &+\left(\frac{\delta R_{cu} \cdot (T_a - T_w)}{(R_i + R_{cu} + R_{insul.} + R_o)^2}\right)^2 \\ &+\left(\frac{\delta R_{insul.} \cdot (T_a - T_w)}{(R_i + R_{cu} + R_{insul.} + R_o)^2}\right)^2 \\ &+\left(\frac{\delta R_i \cdot (T_a - T_w)}{(R_i + R_{cu} + R_{insul.} + R_o)^2}\right)^2 \\ &+\left(\frac{\delta R_o \cdot (T_a - T_w)}{(R_i + R_{cu} + R_{insul.} + R_o)^2}\right)^2\end{aligned}} \tag{A.13}$$

$$R_{cu} = \frac{\log\left(\frac{D_4}{D_3}\right)}{2 \cdot \pi \cdot L \cdot k_{cu}} \tag{A.14}$$

$$\delta R_{cu} = \sqrt{\begin{aligned}&\left(\frac{\log\left(\frac{D_4}{D_3}\right)}{2 \cdot \pi \cdot L^2 \cdot k_{cu}} \cdot \delta L\right)^2 + \left(\frac{\log\left(\frac{D_4}{D_3}\right)}{2 \cdot \pi \cdot L \cdot k_{cu}^2} \cdot \delta k_{cu}\right)^2 \\ &+\left(\frac{\delta D_4}{2 \cdot \pi \cdot L \cdot k_{cu} \cdot D_4}\right)^2 + \left(\frac{\delta D_3}{2 \cdot \pi \cdot L \cdot k_{cu} \cdot D_3}\right)^2\end{aligned}} \tag{A.15}$$

$$R_{insul.} = \frac{\log\left(\frac{D_5}{D_4}\right)}{2 \cdot \pi \cdot L \cdot k_{insul.}} \tag{A.16}$$

$$\delta R_{insul.} = \sqrt{\begin{array}{l}\left(\frac{\delta D_5}{2\cdot\pi\cdot L\cdot k_{insul.}\cdot D_5}\right)^2+\left(\frac{\delta D_4}{2\cdot\pi\cdot L\cdot k_{insul.}\cdot D_4}\right)^2 \\ \quad+\left(\frac{\log\left(\frac{D_5}{D_4}\right)}{2\cdot\pi\cdot L^2\cdot k_{insul.}}\cdot\delta L\right)^2 \\ \quad+\left(\frac{\log\left(\frac{D_5}{D_4}\right)}{2\cdot\pi\cdot L\cdot k_{insul.}^2}\cdot\delta k_{insul.}\right)^2\end{array}} \tag{A.17}$$

The convection coefficient in the annulus of the tube-in-tube heat exchanger is determined using the correlation of Gnielinski [85] (eq. A.19 - A.22). The correlation is only valid for turbulent flows. Hence, during measurements the flow is constantly monitored in order to verify whether it remains turbulent. Furthermore the relative uncertainty on this heat transfer coefficient was safely assumed to be $30\,\%$.

$$R_i = \frac{1}{h_i\cdot\pi\cdot D_3\cdot L} \tag{A.18}$$

$$f_i = \left(1.58\cdot\log(Re) - 3.28\right)^{-2} \tag{A.19}$$

$$Nu_i = \frac{f}{2}\cdot\frac{(Re-1000)\cdot Pr}{1+12.7\cdot\sqrt{\frac{f}{2}}\cdot\left(Pr^{\frac{2}{3}}-1\right)}\cdot\left(1+\left(\frac{D_{H,w}}{L}\right)^{\frac{2}{3}}\right) \tag{A.20}$$

$$Nu_{corr.,i} = Nu_i\cdot\left(\frac{\mu}{\mu_{wall}}\right)^{0.25} \tag{A.21}$$

$$h_i = Nu_{corr.,i}\cdot\frac{k}{D_{H,h}} \tag{A.22}$$

$$\delta R_i = \sqrt{\left(\frac{\delta h_i}{h_i^2\cdot\pi\cdot D_3\cdot L}\right)^2+\left(\frac{\delta D_3}{h_i\cdot\pi\cdot D_3^2\cdot L}\right)^2+\left(\frac{\delta L}{h_i\cdot\pi\cdot D_3\cdot L^2}\right)^2} \tag{A.23}$$

The convection coefficient at the outside of the insulation layer is determined using the correlation of Churchill and Chu [86] (eq. A.25 - A.27). The relative uncertainty on this heat transfer coefficient was safely assumed to be $30\,\%$.

$$R_o = \frac{1}{h_o\cdot\pi\cdot D_5\cdot L} \tag{A.24}$$

$$Ra_o = \frac{g\cdot\beta\cdot\rho^2\cdot c_p\cdot(T_{wall}-T_a)\cdot D^3}{\mu\cdot k} \tag{A.25}$$

$$Nu_o = \left(0.6 + 0.387 \cdot \frac{Ra_o^{\frac{1}{6}}}{\left(1 + \left(\frac{0.559}{Pr}\right)^{\frac{9}{16}}\right)^{\frac{8}{27}}} \right)^2 \tag{A.26}$$

$$h_o = \frac{Nu_o \cdot k}{D} \tag{A.27}$$

$$\delta R_o = \sqrt{\left(\frac{\delta h_o}{h_o^2 \cdot \pi \cdot D_5 \cdot L}\right)^2 + \left(\frac{\delta D_5}{h_o \cdot \pi \cdot D_5^2 \cdot L}\right)^2 + \left(\frac{\delta L}{h_o \cdot \pi \cdot D_5 \cdot L^2}\right)^2} \tag{A.28}$$

$$Q_{PH} = \sum_i Q_{PH,i} \tag{A.29}$$

$$\delta Q_{PH} = \sqrt{\sum_i \left(\delta Q_{PH,i}^2\right)} \tag{A.30}$$

A.3.3 Vapour quality after the preheater

The vapour quality x after the preheater can be determined using a simple heat balance (eq. A.31).

$$x = \frac{\frac{Q_{heat}}{m_{refrig}} + H_{in} - H_{out,liq}}{H_{vap}} \tag{A.31}$$

$$\delta x = \sqrt{\begin{array}{c} \left(\frac{\delta Q_{heat}}{m_{refrig} \cdot H_{vap}}\right)^2 + \left(\frac{\delta H_{in}}{H_{vap}}\right)^2 + \left(\frac{-\delta H_{out,liq}}{H_{vap}}\right)^2 \\ + \left(\frac{\frac{Q_{heat}}{m_{refrig}} + H_{in} - H_{out,liq}}{{H_{vap}}^2} \cdot \delta H_{vap}\right)^2 \\ + \left(\frac{Q_{heat}}{{m_{refrig}}^2 \cdot H_{vap}} \cdot \delta m_{refrig}\right)^2 \end{array}} \tag{A.32}$$

A.3.4 Heat transferred to the refrigerant in the evaporator section

The heat transferred to the refrigerant in the evaporator section is the heat dissipated by the electrical heaters minus the heat loss to the environment.

$$Q_{TS} = \sum_i \left(P_{\text{electr.,i}} - Q_{loss,i}\right) \tag{A.33}$$

$$\delta Q_{TS} = \sqrt{\sum_i \left(\delta P_{\text{electr.,i}}^2 + \delta Q_{loss,i}^2\right)} \tag{A.34}$$

The heat loss to the environment is calculated using a one-dimensional model which is depicted in figure A.2. The model uses the electrical resistance analogy. The model calculates the heat loss based on the measured heater and ambient air temperature and the known thermal resistances.

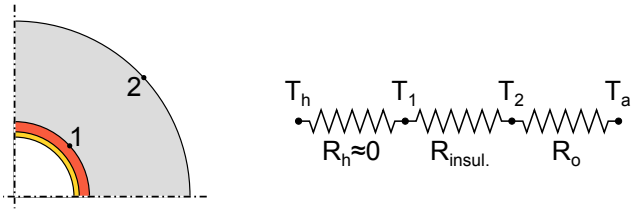

Figure A.2: A schematic representation of the model used to estimate the heat losses to the environment at the evaporator section. (refrigerant; tube wall; electrical heater; 1-2: insulation; ambient air)

$$Q_{loss,i} = \frac{T_a - T_h}{R_{insul.} + R_o} \tag{A.35}$$

$$\delta Q_{loss,i} = \sqrt{\left(\delta R_{insul.} \cdot \frac{T_a - T_h}{(R_{insul.} + R_o)^2}\right)^2 + \left(\delta R_o \cdot \frac{T_a - T_h}{(R_{insul.} + R_o)^2}\right)^2 + \left(\frac{\delta T_a}{R_{insul.} + R_o}\right)^2 + \left(\frac{\delta T_h}{R_{insul.} + R_o}\right)^2} \tag{A.36}$$

$$R_{insul.} = \frac{\log\left(\frac{D_2}{D_1}\right)}{2 \cdot \pi \cdot L \cdot k_{insul.}} \tag{A.37}$$

$$\delta R_{insul.} = \sqrt{\left(\frac{\delta D_2}{2 \cdot \pi \cdot L \cdot k_{insul.} \cdot D_2}\right)^2 + \left(\frac{\delta D_1}{2 \cdot \pi \cdot L \cdot k_{insul.} \cdot D_1}\right)^2 + \left(\frac{\log\left(\frac{D_2}{D_1}\right)}{2 \cdot \pi \cdot L^2 \cdot k_{insul.}} \cdot \delta L\right)^2 + \left(\frac{\log\left(\frac{D_2}{D_1}\right)}{2 \cdot \pi \cdot L \cdot k_{insul.}^2} \cdot \delta k_{insul.}\right)^2} \tag{A.38}$$

The convection coefficient at the outside of the insulation layer is determined using the correlation of Churchill and Chu [86] (eq. A.25 - A.27). The relative uncertainty on this heat transfer coefficient was safely assumed to be $30\,\%$.

$$R_o = \frac{1}{h_o \cdot \pi \cdot D_2 \cdot L} \tag{A.39}$$

$$\delta R_o = \sqrt{\left(\frac{\delta h_o}{h_o^2 \cdot \pi \cdot D_2 \cdot L}\right)^2 + \left(\frac{\delta D_2}{h_o \cdot \pi \cdot D_2^2 \cdot L}\right)^2 + \left(\frac{\delta L}{h_o \cdot \pi \cdot D_2 \cdot L^2}\right)^2} \quad \text{(A.40)}$$

A.3.5 Vapour quality at the inlet of a T-junction's branch

The vapour quality x at the inlet of a T-junction's branch can be determined using a simple heat balance (eq. A.41).

$$x_{branch,in} = \frac{\frac{-Q_{TS}}{m_{refrig}} + H_{out} - H_{in,liq}}{H_{vap}} \quad \text{(A.41)}$$

$$\delta x_{branch,in} = \sqrt{\begin{array}{l}\left(\frac{-\delta Q_{TS}}{H_{vap} \cdot m_{refrig}}\right)^2 + \left(\frac{Q_{TS}}{H_{vap} \cdot {m_{refrig}}^2} \cdot \delta m_{refrig}\right)^2 \\ \quad + \left(\frac{\delta H_{out}}{H_{vap}}\right)^2 + \left(\frac{-\delta H_{in,liq}}{H_{vap}}\right)^2 \\ \quad + \left(\frac{\frac{Q_{TS}}{m_{refrig}} - H_{out} + Hin,liq}{{H_{vap}}^2} \cdot \delta H_{vap}\right)^2\end{array}} \quad \text{(A.42)}$$

A.3.6 $dP_{junction}$

To determine the pressure drop over the junction, first a best linear fitting $(a \cdot x + b)$ through the points at the inlet and at the branch is calculated.

$$\sigma_{line} = \sqrt{\frac{1}{N_{points} - 2} \cdot \sum_{N_{points}} \left(P(x) - (a \cdot x + b)\right)^2} \quad \text{(A.43)}$$

The pressure drop over the junction is then given by:

$$dP_{junction} = b_{branch} - b_{inlet} \quad \text{(A.44)}$$

$$\delta dP_{junction} = \sqrt{\left(\delta P + 2 \cdot \sigma_{line,branch}\right)^2 + \left(\delta P + 2 \cdot \sigma_{line,inlet}\right)^2} \quad \text{(A.45)}$$

A.4 P& ID

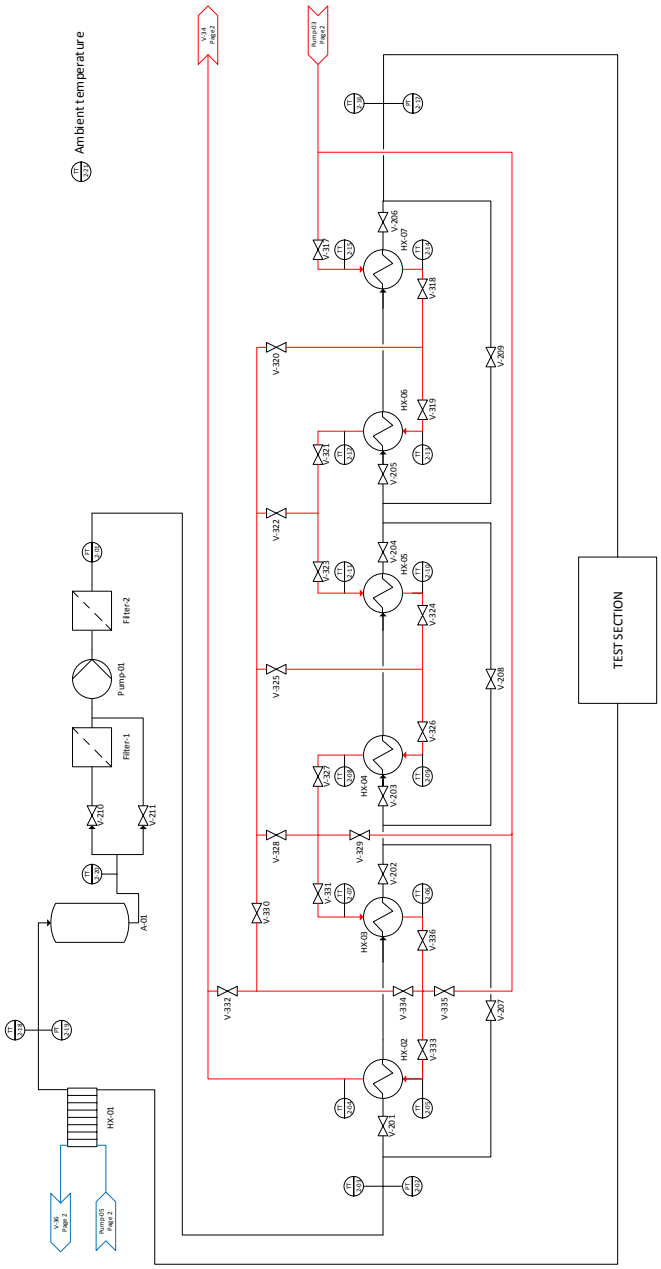

Figure A.3: P& ID of the flow conditioner.

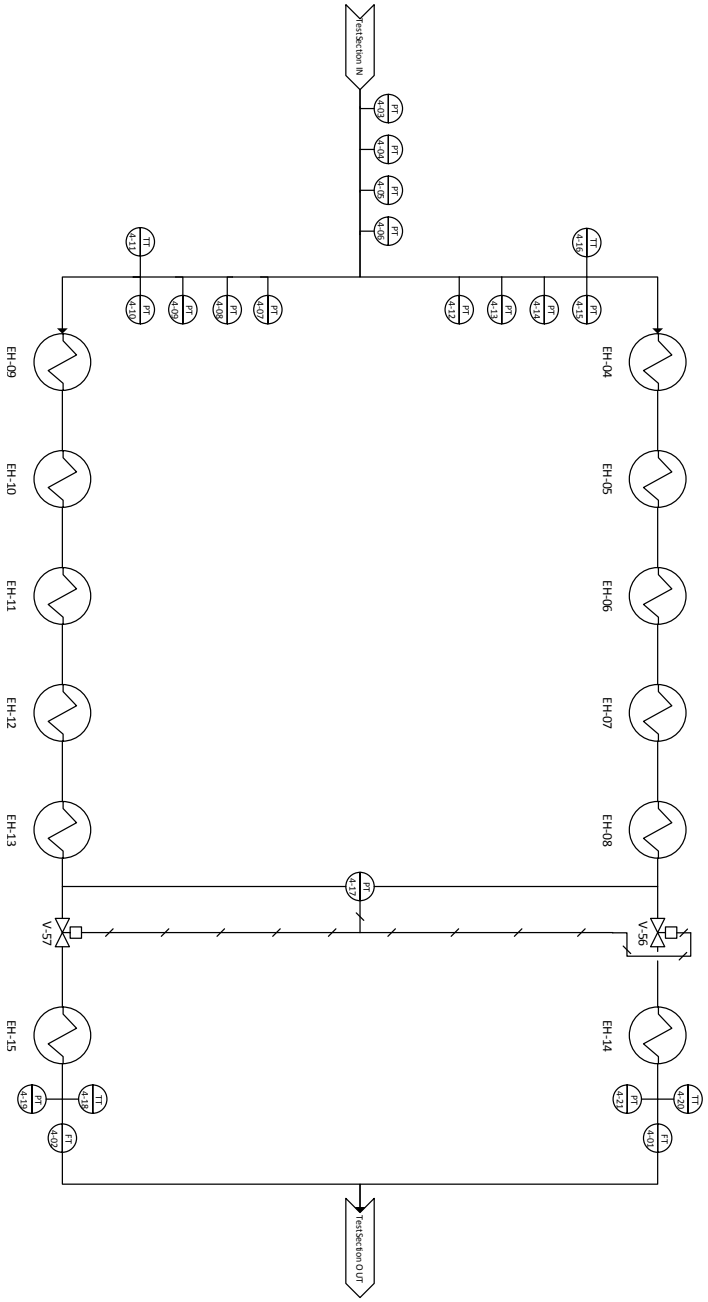

Figure A.4: P& ID of the test section.

B

Void fraction measurements

This chapter first describes the void fraction measuring method using the capacitive void fraction probe. Furthermore, the void fraction measurements are compared with existing models to verify if they are valid to use. Finally, the flow regime map of Wojtan *et al.* [28] is compared with the flow regime determination method developed by De Kerpel [21].

B.1 Measurement method

A description of the capacitive void fraction probe is given in section 3.2.3. The capacity measured at the probe is converted linearly to a voltage signal using a specially made signal conditioner. This voltage is then acquired with the data acquisition system.

The measured voltage is normalised to a value between 0 and 1. The normalisation function uses the voltage of a liquid filled and a vapour filled sensor at the measured saturation temperature. This normalised value is then converted to a void fraction ϵ using a flow regime dependant calibration curve. An example of such a calibration curve is shown in figure B.1. In this work, the flow regime is determined using the flow regime map of Wojtan *et al.* [28]. To verify if this flow regime map is accurate, the results were compared with the flow regime determination method developed by De Kerpel [21] in section B.3. The following section will explain the method to derive the flow regime dependant calibration curves.

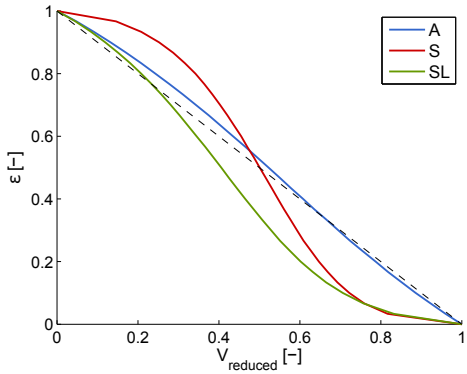

Figure B.1: The void fraction sensor calibration curves for R32.

B.1.1 Calibration curve

The calibration curves are constructed using finite element simulations of the sensor. These simulations are done in FEMM [87].

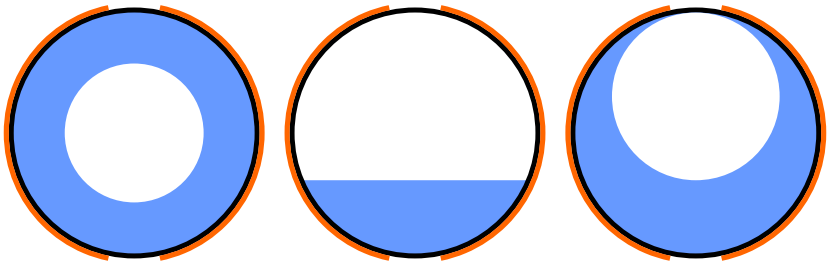

(a) annular *(b) stratified* *(c) slug*

Figure B.2: The simplified geometries implemented in the FEMM [87] simulations. (black: Kapton tube wall; blue: liquid phase; white: vapour phase; orange: electrodes)

For each flow regime, a simplified representation of the spacial distribution of the two phase was constructed. Figure B.2 shows the geometries for three flow regimes: annular, stratified and slug flow. For each geometry, several simulations with a varying void fraction are conducted to construct the relation between the capacity value and the void fraction (figure B.1). The intermittent flow regime does not use a particular geometry but is based on an interpolation between the calibration curves of an annular and a slug flow:

$$\epsilon = \frac{x - x_{i-sl}}{x_{i-a} - x_{i-sl}} \cdot \epsilon_A + \frac{x_{i-a} - x}{x_{i-a} - x_{i-sl}} \cdot \epsilon_{SL} \tag{B.1}$$

x_{i-a} is the vapour quality at which the transition between the intermittent and the

annular flow occurs. x_{i-sl} is the vapour quality at which the transition between an intermittent and an annular flow occurs.

B.2 Comparison with existing models

The experimental void fraction measurements were compared with the void fractions determined using an existing model.

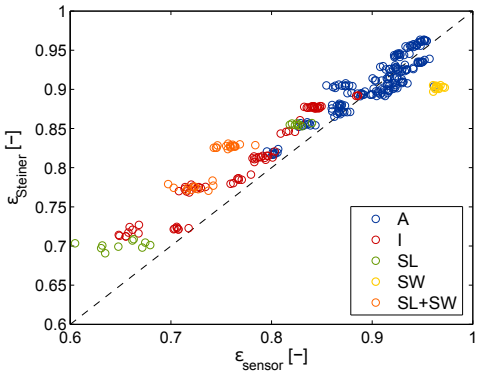

Figure B.3: The void fractions measured experimentally compared to the void fractions determined with the model of Steiner *[26]*

The first model tested is Steiner's [26] adaptation of the drift flux model of Rouhani and Axelsson [25]. This model is compared with the experimental results in figure B.3. The model clearly overpredicts the void fraction for lower void fraction. Only for the annular flow, the prediction is quite accurate as shown by the mean absolute errors (MAE) and the mean relative errors (MRE) in table B.1.

	A	I	SL	SW	SL+SW	All
MAE	0.014	0.033	0.041	0.062	0.063	0.026
MRE	−0.005	−0.033	−0.041	0.063	−0.063	−0.016

Table B.1: The mean absolute error (MAE) and the mean relative error (MRE) of Steiner's model [26] for the different flow regimes.

The second model evaluated is the model of Shoham et al. [88]. The comparison with the experimental results is shown in figure B.4. The model overpredicts the void fraction for most flow regimes except for stratified-wavy.

On average both models are capable of predicting the void fraction. However, the void fraction of stratified-wavy flow is not predicted well for both models.

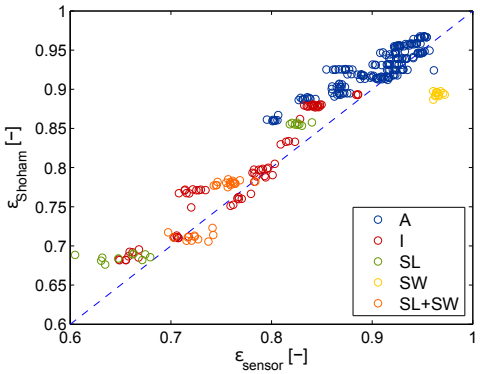

Figure B.4: The void fractions measured experimentally compared to the void fractions determined with the model of Shoham et al. *[88]*

	A	I	SL	SW	SL+SW	All
MAE	0.024	0.024	0.033	0.072	0.020	0.026
MRE	−0.023	−0.021	−0.033	0.072	−0.009	−0.018

Table B.2: The mean absolute error (MAE) and the mean relative error (MRE) of Shoham's models [88] for the different flow regimes.

In this work, Steiner's [26] adaptation of the drift flux model of Rouhani and Axelsson [25] will be used due to its simplicity.

B.3 Flow regime determination

As already explained in chapter 3.2.3, the flow regime can be determined based on the frequency spectrum of the signal of the voidfraction sensor. In the following paragraph the method will explained briefly. More details on the method are given in the work of De Kerpel [21].

A maximum overlap wavelet transform (MODWT) with the 8th order Daubechies wavelet function is performed on the time signal of the void fraction sensor. The wavelet variance is then calculated. The slope between the 3^{rd} and 4^{th} wavelet variance is used to classify the different flow regimes with a fuzzy clustering algorithm. The exact value of the slope at the flow regime transition, depends on the sensor geometry and the fluid. Due to the limited dataset and a time constraint, the exact value at the flow regime transition was not determined. However, figure B.5 can be used to verify the accuracy of the flow regime map of Wojtan *et al.* [28] for this refrigerant.

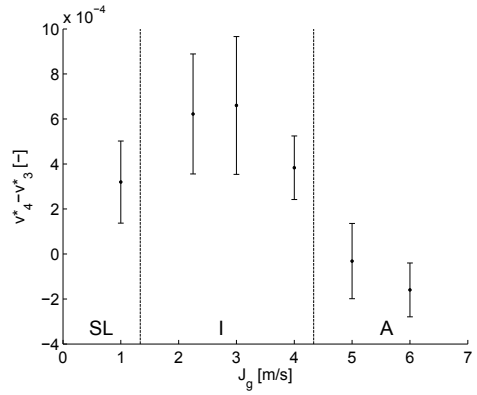

Figure B.5: The difference between the 3rd and 4th wavelet variance as function of the superficial vapour velocity (R32; T_{sat} = 10 °C; J_l = 0.2 m/s). The dashed lines indicate the flow regime transitions according to Wojtan et al. *[28].*

Figure B.5 displays the difference between the 3rd and 4th wavelet variance as function of the superficial vapour velocity. The dashed lines in the figure indicate the flow regime transitions according to Wojtan *et al.* [28]. The value of the slope is significantly larger for the intermittend than for the annular flow. Hence, the classification of these points according to flow regime map ofWojtan *et al.* [28] corresponds with the classification found experimentally.

C

List of experimental data

fluid	θ	T_{sat}	J_l	J_g	G	x	**flow regime**
R32	0	10	0.2	1.5	249	0.18	I
	0	10	0.2	3	295	0.31	I
	0	10	0.3	1.5	351	0.13	I
	0	10	0.3	3	397	0.23	I
	0	20	0.2	1.5	258	0.24	I
	0	20	0.2	3	319	0.38	I
	0	20	0.3	1.5	356	0.17	I
	0	20	0.3	3	417	0.29	I
	0	10	0.2	5	355	0.43	A
	0	10	0.2	4	325	0.37	I
	0	10	0.2	6	385	0.47	A
	0	10	0.2	1	234	0.13	SL
	0	10	0.2	2.25	272	0.25	I
	0	10	0.1	3	193	0.47	A
	0	10	0.1	5	253	0.60	A
	0	10	0.1	4	223	0.54	A
	0	20	0.2	4	360	0.45	A
	0	10	0.1	6	283	0.64	A
	0	10	0.1	2	162	0.37	I
	0	10	0.1	1	132	0.23	SL+SW
	0	10	0.05	2	111	0.54	SW
	0	10	0.05	3	142	0.64	A
	0	10	0.05	4	172	0.70	A
	0	10	0.05	5	202	0.75	A
	0	20	0.1	3	221	0.56	A
	0	10	0.279	2.2	351	0.19	I
	0	10	0.189	5.25	351	0.45	A
	0	10	0.171	5.83	351	0.50	A
	0	10	0.1	1.5	147	0.31	SL+SW
	0	10	0.1	2.5	178	0.43	I
	0	10	0.05	6	232	0.78	A
	45	10	0.2	1.5	249	0.18	I
	45	10	0.2	3	295	0.31	I
	45	10	0.3	1.5	351	0.13	I
	45	10	0.3	3	397	0.23	I
	22.5	10	0.2	1.5	249	0.18	I
	22.5	10	0.2	3	295	0.31	I
	22.5	10	0.3	1.5	351	0.13	I
	22.5	10	0.3	3	397	0.23	I

Table C.1: The overview of the experimental inlet conditions tested in this work (part 1).

fluid	θ	T_{sat}	J_l	J_g	G	x	**flow regime**
R1234ze	0	20	0.15	1.5	211	0.16	SL
	0	20	0.15	3	245	0.28	I
	0	20	0.225	1.5	299	0.11	I
	0	20	0.225	3	333	0.20	I
R134a	0	20	0.2	1.5	287	0.15	I
	0	20	0.2	3	328	0.25	I
	0	20	0.3	1.5	409	0.10	I
	0	20	0.05	4	172	0.64	A
	0	20	0.05	5	200	0.69	A
	0	20	0.05	2	117	0.48	SW
	0	20	0.05	3	145	0.58	SW
R125	0	10	0.2	1.5	341	0.25	I
	0	10	0.2	3	427	0.40	A
	0	10	0.3	1.5	468	0.18	I
	0	20	0.2	1.5	361	0.32	I
	0	20	0.2	3	478	0.49	A
	0	20	0.3	1.5	482	0.24	I
	0	20	0.3	3	599	0.39	A
	22.5	10	0.2	1.5	341	0.25	I
	22.5	10	0.2	3	427	0.40	A
	22.5	10	0.3	1.5	468	0.18	I

Table C.2: The overview of the experimental inlet conditions tested in this work (part 2).

D

Evaluation of existing phase distribution models

This chapter examines the prediction capability of the existing phase distribution models. The models are evaluated using the water-air and water-steam phase distribution data of horizontal impacting T-junctions found in the literature.

Each model has different input and output parameters which makes quantitative comparisons between the different models difficult. Hence, it was chosen to test the prediction of each model using its own output parameter. For each model the MAD, the MRD and the percentage of data with a MAD smaller than 0.05 was determined and will be discussed in the following sections.

D.1 Models of Azzopardi *et al.* [57, 58]

The first model of Azzopardi *et al.* [57] predicts the liquid fraction distribution F_l for a given inlet flow and a given vapour fraction distribution F_g. Table D.1 illustrates the prediction capabilities of this model for the data found in the literature.

In general, this model is not very capable of predicting the phase distribution. It only predicts the annular water-air data rather well. This can be explained by the fact that the model was constructed using annular and intermittent water-air data. As expected, the model is not suited for stratified flows because the model was made for a T-junction with a vertical inlet. Stratified flows do not occur in a

vertical flow due to the different orientation of the gravity force. Finally, the phase distribution prediction for the water-steam data is really substandard as the model was developed using only water-air data. Hence, the model does not capture the effects related to the fluid properties.

dataset		**# points**	**MRD**	**MAD**	**MAD <0.05**
El-Shaboury *et al.* [47]	A	10	−0.01	0.027	80 %
	SW	26	−0.091	0.108	50 %
	S	15	0.065	0.092	67 %
	All	51	−0.029	0.087	61 %
Ottens *et al.* [52]	SW	35	−0.052	0.147	31 %
	All	35	−0.052	0.147	31 %
Chien and Rubel [54, 73]	A	136	−0.021	0.064	42 %
	All	136	−0.021	0.064	42 %
Hong and Christon [53]	A	16	0	0.081	25 %
	I	4	0	0.015	100 %
	SW	8	0	0.137	0 %
	SL+SW	10	0	0.061	40 %
	All	38	0	0.081	32 %
Mohamed *et al.* [37]	A	32	0	0.040	69 %
	SW	42	0	0.090	45 %
	S	21	0	0.075	43 %
	All	95	0	0.070	53 %
Mohamed *et al.* [42]	A	39	−0.004	0.032	77 %
	SW	35	−0.002	0.095	29 %
	S	22	0	0.077	36 %
	All	96	−0.002	0.065	50 %
water-air data		277	−0.013	0.081	51 %
water-steam data		174	−0.016	0.068	40 %
all data		451	−0.014	0.076	46 %

Table D.1: The prediction capabilities of Azzopardi's [57] model for the data found in the literature.

The second model of Azzopardi *et al.* [58] predicts the vapour fraction distribution F_g for a given inlet condition and a given liquid fraction distribution F_l. Table D.2 illustrates the prediction capabilities of this model for the data found in the literature.

In contrast to their previous model, this model performs better for the water-steam data than for the water-air data. However, the model still does not capture all the effects related to fluid properties.

dataset		**# points**	**MRD**	**MAD**	**MAD <0.05**
El-Shaboury *et al.* [47]	A	10	0.029	0.079	30 %
	SW	26	0.083	0.104	46 %
	S	15	−0.105	0.112	53 %
	All	51	0.017	0.101	45 %
Ottens *et al.* [52]	SW	35	0.043	0.1	40 %
	All	35	0.043	0.1	40 %
Chien and Rubel [54, 73]	A	136	−0.018	0.03	80 %
	All	136	−0.018	0.03	80 %
Hong and Christon [53]	A	16	0	0.092	37 %
	I	4	0	0.06	50 %
	SW	8	0	0.069	25 %
	SL+SW	10	0	0.029	80 %
	All	38	0	0.067	47 %
Mohamed *et al.* [42]	A	39	0.003	0.081	33 %
	SW	35	0.003	0.058	60 %
	S	22	0.001	0.058	45 %
	All	96	0.003	0.067	46 %
Mohamed *et al.* [37]	A	32	0	0.1	25 %
	SW	42	0.002	0.075	50 %
	S	21	0	0.089	33 %
	All	95	0.001	0.086	38 %
water-air data		277	0.010	0.084	42 %
water-steam data		174	−0.014	0.038	73 %
all data		451	0.001	0.066	54 %

Table D.2: The prediction capabilities of Azzopardi's [58] model for the data found in the literature.

D.2 Models of Ottens *et al.* [52]

Ottens *et al.* [52] developed two models: the double stream model and the advanced double stream model. The advanced model is an extension of the normal double stream model which nullifies some assumptions made in the original model. Both models predict the liquid fraction distribution F_l for a given inlet condition and a given vapour fraction distribution F_g. The prediction capabilities of the double stream model and the advanced double stream model are respectively given in table D.3 and table D.4.

dataset		**# points**	**MRD**	**MAD**	**MAD <0.05**
El-Shaboury *et al.* [47]	A	10	−0.100	0.183	30 %
	SW	26	0.024	0.043	77 %
	S	15	−0.103	0.110	47 %
	All	51	−0.038	0.090	59 %
Ottens *et al.* [52]	SW	35	0.073	0.105	49 %
	All	35	0.073	0.105	49 %
Chien and Rubel [54, 73]	A	136	0.130	0.176	20 %
	All	136	0.130	0.176	20 %
Hong and Christon [53]	A	16	0	0.144	38 %
	I	4	0.000	0.283	00 %
	SW	8	0.000	0.178	25 %
	SL+SW	10	0.000	0.220	20 %
	All	38	0.000	0.186	26 %
Mohamed *et al.* [37]	A	32	0.001	0.206	13 %
	SW	42	0.002	0.071	60 %
	S	21	0.000	0.180	14 %
	All	95	0.001	0.140	34 %
Mohamed *et al.* [42]	A	39	0.003	0.083	54 %
	SW	35	0.002	0.091	49 %
	S	22	0.000	0.070	64 %
	All	96	0.002	0.083	54 %
water-air data		277	0.003	0.107	47 %
water-steam data		174	0.102	0.178	21 %
all data		451	0.041	0.134	37 %

Table D.3: The prediction capabilities of the double stream model [52] for the data found in the literature.

The first thing to notice is the small difference in prediction capability of both models. Even though the advanced model abrogates some assumptions and is more complex to solve, it does not translate in better performance. Secondly, the model does not predict the authors own data more accurately than other water-air data found in the literature. Finally, the prediction of the water-steam data is significantly worse than the prediction of the water-air data. Furthermore, the

model over-predicts the data of Chien and Rubel significantly. Hence, these models do not capture the fluid properties related effects and are only suited for water-air mixtures.

dataset		**# points**	**MRD**	**MAD**	**MAD <0.05**
El-Shaboury *et al.* [47]	A	10	−0.047	0.082	50 %
	SW	26	−0.006	0.046	65 %
	S	15	0.153	0.196	40 %
	All	51	0.033	0.097	55 %
Ottens *et al.* [52]	SW	35	0.066	0.108	37 %
	All	35	0.066	0.108	37 %
Chien and Rubel [54, 73]	A	136	0.182	0.244	17 %
	All	136	0.182	0.244	17 %
Hong and Christon [53]	A	16	−0.001	0.195	38 %
	I	4	−0.005	0.315	0 %
	SW	8	−0.076	0.252	0 %
	SL+SW	10	−0.051	0.220	30 %
	All	38	−0.030	0.226	24 %
Mohamed *et al.* [37]	A	32	0.031	0.090	56 %
	SW	42	0.007	0.051	67 %
	S	21	0.001	0.187	14 %
	All	95	0.014	0.094	52 %
Mohamed *et al.* [42]	A	39	0.001	0.115	41 %
	SW	35	0.001	0.092	54 %
	S	22	0.003	0.094	41 %
	All	96	0.002	0.102	46 %
water-air data		277	0.020	0.099	48 %
water-steam data		174	0.136	0.240	18 %
all data		451	0.064	0.154	37 %

Table D.4: The prediction capabilities of the advanced double stream model [52] for the data found in the literature.

D.3 Model of Hong and Christon [53]

The model of Hong and Christon [53] predicts the liquid fraction distribution F_l for a given inlet flow and a given vapour fraction distribution F_g. Its prediction capabilities are given in table D.5.

As expected, the model is best suited for water-steam flows according to table D.5. More specifically, this model was developed using water-steam data. Furthermore, the best prediction capabilities were found for their own data. Finally, the model is not capable of predicting the phase distribution of stratified flows.

dataset		**# points**	**MRD**	**MAD**	**MAD <0.05**
El-Shaboury *et al.* [47]	A	10	−0.042	0.085	50 %
	SW	26	−0.048	0.117	31 %
	S	15	−0.162	0.230	0 %
	All	51	−0.080	0.144	25 %
Ottens *et al.* [52]	SW	35	0.080	0.197	9 %
	All	35	0.080	0.197	9 %
Chien and Rubel [54, 73]	A	136	0.045	0.071	40 %
	All	136	0.045	0.071	40 %
Hong and Christon [53]	A	16	0.000	0.033	75 %
	I	4	0.000	0.101	0 %
	SW	8	0.002	0.037	50 %
	SL+SW	10	0.000	0.093	20 %
	All	38	0.000	0.057	47 %
Mohamed *et al.* [37]	A	32	0.000	0.072	69 %
	SW	42	0.002	0.085	24 %
	S	21	0.010	0.204	0 %
	All	95	0.003	0.107	34 %
Mohamed *et al.* [42]	A	39	−0.004	0.096	21 %
	SW	35	−0.011	0.106	14 %
	S	22	0.000	0.125	5 %
	All	96	−0.005	0.106	15 %
water-air data		277	−0.006	0.125	22 %
water-steam data		174	0.035	0.068	41 %
all data		451	0.010	0.103	30 %

Table D.5: The prediction capabilities of the model of Hong and Christon [53] for the data found in the literature.

D.4 Model of Chien and Rubel [54, 73]

The model of Chien and Rubel [54, 73] predicts the liquid fraction distribution F_l for a given inlet flow and a given vapour fraction distribution F_g. Its prediction capability is given in table D.6.

First of all, the most accurate predictions are found for their own data. Further, as expected, the model gives the best results for water-steam data. More specifically, this model was developed using water-steam data.

dataset		**# points**	**MRD**	**MAD**	**MAD <0.05**
El-Shaboury *et al.* [47]	A	10	0.034	0.077	50 %
	SW	26	0.086	0.105	46 %
	S	15	−0.101	0.111	60 %
	All	51	0.020	0.102	51 %
Ottens *et al.* [52]	SW	35	0.043	0.106	49 %
	All	35	0.043	0.106	49 %
Chien and Rubel [54, 73]	A	136	−0.004	0.028	84 %
	All	136	−0.004	0.028	84 %
Hong and Christon [53]	A	16	0.000	0.078	38 %
	I	4	0.000	0.033	50 %
	SW	8	0.000	0.079	25 %
	SL+SW	10	0.000	0.028	80 %
	All	38	0.000	0.060	47 %
Mohamed *et al.* [37]	A	32	0.000	0.092	38 %
	SW	42	0.002	0.084	45 %
	S	21	0.000	0.090	33 %
	All	95	0.001	0.088	40 %
Mohamed *et al.* [42]	A	39	0.003	0.078	36 %
	SW	35	0.003	0.064	63 %
	S	22	0.000	0.065	45 %
	All	96	0.002	0.070	48 %
water-air data		277	0.010	0.087	46 %
water-steam data		174	−0.003	0.035	76 %
all data		451	0.005	0.067	57 %

Table D.6: The prediction capabilities of the model of Chien and Rubel [54, 73] for the data found in the literature.

D.5 Model of El-Shaboury *et al.* [47]

The most recent phase distribution model is developed by El-Shaboury *et al.* [47]. In contrast to previous models, this model predicts both the liquid fraction distribution F_l and the vapour fraction distribution F_g for a given inlet flow and a given total mass distribution. In this manuscript, only the prediction of the liquid fraction distribution F_l is given (see table D.7). The results of the vapour fraction distribution F_g are very similar.

First of all, the prediction of their own data is excellent. More generally, the prediction of the water-air data is very good. In contrast, the prediction of the water-steam data is substandard. Namely, the MAD for the water-steam data is 0.32 which means that on average the F_l value deviates with 0.32 from the real value. This deviation is very large compared to the range of F_l (0 - 1). Hence, this model appears not to be suited for mixtures other than water-air.

dataset		**# points**	**MRD**	**MAD**	**MAD <0.05**
El-Shaboury *et al.* [47]	A	10	-0.003	0.005	$100\,\%$
	SW	26	0.171	0.181	$73\,\%$
	S	15	-0.001	0.005	$100\,\%$
	All	51	0.086	0.095	$86\,\%$
Ottens *et al.* [52]	SW	35	0.060	0.127	$37\,\%$
	All	35	0.060	0.127	$37\,\%$
Chien and Rubel [54, 73]	A	136	-0.168	0.317	$0\,\%$
	All	136	-0.168	0.317	$0\,\%$
Hong and Christon [53]	A	16	0.000	0.340	$0\,\%$
	SW	8	0.000	0.393	$0\,\%$
	All	38	0.000	0.358	$0\,\%$
Mohamed *et al.* [37]	A	32	0.001	0.004	$100\,\%$
	SW	42	0.007	0.016	$95\,\%$
	S	21	0.000	0.050	$52\,\%$
	All	95	0.003	0.020	$87\,\%$
Mohamed *et al.* [42]	A	39	0.002	0.047	$64\,\%$
	SW	35	0.012	0.069	$71\,\%$
	S	22	0.000	0.043	$64\,\%$
	All	96	0.005	0.054	$67\,\%$
water-air data		277	0.026	0.059	$74\,\%$
water-steam data		174	-0.143	0.323	$0\,\%$
all data		451	-0.036	0.156	$45\,\%$

Table D.7: The prediction capabilities of the model of El-Shaboury et al. *[47] for the data found in the literature.*

D.6 Conclusion

In general, one can conclude that the largest prediction capability of the models is for their own data. Secondly, none of the models incorporates the influence of the fluid properties on the phase distribution. Most models give the best results for the fluid for which the model was designed. Hence, a new model is needed which includes the effects of fluid properties and is capable of predicting phase distribution for different two-phase mixtures.

Finally, the model of El-Shaboury *et al.* [47] is recommended for water-air mixtures. For water-steam mixtures, both the model of Chien and Rubel [54, 73] and Azzopardi *et al.* [58] work well. Both models also give the best overall performance (water-air data and water-steam data).

E

Publications

E.1 Related publications in peer-reviewed international journals

- M. Billiet, B. Ameel, R. Charnay, R. Revellin, and M. De Paepe, "Flow regime based heat transfer correlation for R245fa in a 3 mm tube," Int. J. Heat Mass Transf., vol. 117, pp. 1304–1311, 2018.

E.2 Other publications in peer-reviewed international journals

- M. Lazova, A. Kaya, M. Billiet, S. Lecompte, D. Manolakos, and M. De Paepe, "Experimental assessment of a helical coil heat exchanger operating at subcritical and supercritical conditions in a small-scale solar organic rankine cycle," Energies, vol. 10, no. 5, 2017.

- M. Billiet, S. De Schampheleire, H. Huisseune, and M. De Paepe, "Influence of orientation and radiative heat transfer on aluminum foams in buoyancy-induced convection," Materials (Basel)., vol. 8, no. 10, pp. 6792–6805, 2015.

E.3 Related publications in proceedings of international conferences

- M. Billiet, Y. Bastien, M. Lazova, A. Kaya, S. Lecompte, and M. De Paepe, "The distribution over an impacting T-junction of two-phase R32 under heat pump conditions," in Heat Transfer, Fluid Mechanics and Thermodynamics, 13th International conference, Proceedings, 2017.

- M. Billiet, Y. Bastien, S. Lecompte, M. Lazova, A. Kaya, and M. De Paepe, "The distribution of two-phase R32 over an impacting T-junction," in 9th World Conference on Experimental Heat Transfer, Fluid Mechanics and Thermodynamics, 2017.

- M. Billiet, R. Revellin, R. Charnay, and M. De Paepe, "Experimental two-phase heat transfer study of R245fa in horizontal mini-channels at high saturation temperatures," in Proceedings of 7th European Thermal-Sciences Conference, 2016.

- M. Billiet, R. Charnay, R. Revellin, L. Bokisova, and M. De Paepe, "Two-phase heat transfer measurements of R254fa at high saturation temperatures in horizontal mini-channels," in 12th International Conference on Heat Transfer, Fluid Mechanics and Thermodynamics, 2016.

E.4 Other publications in proceedings of international conferences

- W. Faes, S. Lecompte, J. Van Bael, R. Salenbien, M. Billiet, and M. De Paepe, "Design of an experimental set-up to determine the influence of corrosion on heat transfer," in Heat Transfer, Fluid Mechanics and Thermodynamics, 13th International conference, Proceedings, 2017.

- M. Lazova, A. Kaya, M. Billiet, S. Lecompte, and M. De Paepe, "Experimental investigation of a forced convection heat transfer of the organic fluid R-125 at supercritical pressures and under organic rankine cycle conditions," in Heat Transfer, Fluid Mechanics and Thermodynamics, 13th International conference, Proceedings, 2017.

- B. Ameel, S. Lecompte, M. Billiet, D. Daenens, and M. De Paepe, "Determining heat losses in a reheat furnace : a case study," in Proceedings of ECOS 2017 - The 30th Environmental Conference on Efficiency, Cost, Optimization, Simulation and Environmental Impact of Energy systems, 2017.

- M. Billiet, S. De Schampheleire, H. Huisseune, Z. H. Qiu, and M. De Paepe, "Experimental investigation of the effects of foam height, emissivity and orientation on buoyancy-driven convection in open-cell aluminium foam," in 11th International Conference on Heat Transfer, Fluid Mechanics and Thermodynamics, Proceedings, 2015, pp. 833–838.
- M. Billiet, S. De Schampheleire, H. Huisseune, and M. De Paepe, "Experimental study of the effects of foam height, orientation and radiative heat transfer on buoyancy-driven convection," in MetFoam 2015, Proceedings, 2015.
- K. De Kerpel, S. De Schampheleire, A. Kaya, M. Billiet, and M. De Paepe, "The refrigerant two-phase flow void fraction in the vicinity of a sharp return bend," in Refrigeration Science and Technology, 2015.

References

[1] European Commission. *Buildings - European Commission*. https://ec.europa.eu/energy/en/topics/energy-efficiency/buildings. Accessed: 04-09-2018.

[2] Gunda Mader, Björn Palm, and Brian Elmegaard. *Maldistribution in air–water heat pump evaporators. Part 1: Effects on evaporator, heat pump and system level*. International Journal of Refrigeration, 50:207–216, 2015.

[3] Ralph Keeling and Pieter Tans. *dataset of mean carbon dioxide measured at Mauna Loa Observatory, Hawaii (NOAA/ESRL)*. https://www.esrl.noaa.gov/gmd/ccgg/trends/data.html. Accessed: 04-09-2018.

[4] Jay H. Lawrimore, Matthew J. Menne, Byron E. Gleason, Claude N. Williams, David B. Wuertz, Russell S. Vose, and Jared Rennie. *An overview of the Global Historical Climatology Network monthly mean temperature data set, version 3*. Journal of Geophysical Research: Atmospheres, 116(D19), 2011.

[5] T.F. Stocker, D. Qin, G.-K. Plattner, M. Tignor, S.K. Allen, J. Boschung, A. Nauels, Y. Xia, V. Bex, and P.M. Midgley. *IPCC, 2013: Summary for Policymakers*, page 1–30. Cambridge University Press, 2014.

[6] *2050 low-carbon economy — Climate Action*. https://ec.europa.eu/clima/policies/strategies/2050_en. Accessed: 04-09-2018.

[7] eurostat. *Final energy consumption by sector (EuroStat dataset)*. http://ec.europa.eu/eurostat/tgm/table.do?tab=table&plugin=1&language=en&pcode=tsdpc320. Accessed: 04-09-2018.

[8] Andrew Clark Beaver, J M Yin, C W Bullard, and P S Hrnjak. *An experimental investigation of transcritical carbon dioxide systems for residential air conditioning*. Technical report, Air Conditioning and Refrigeration Center. College of Engineering. University of Illinois at Urbana-Champaign., 1999.

[9] Jong Min Choi, W Vance Payne, and Piotr A Domanski. *Effects of non-uniform refrigerant and air flow distributions on finned-tube evaporator performance (Paper 40)*. In Proceedings of International Congress Refrigeration, 2003.

[10] Christian K Bach, Eckhard A Groll, and James E Braun. *Application Of A Hybrid Control Of Expansion Valves To A 3-Ton Large Room Cooling System (Paper 1171)*. In Proceedings of International Refrigeration and Air Conditioning Conference, 2012.

[11] Christian K Bach, Eckhard A Groll, and James E Braun. *Application of a Hybrid Control of Expansion Valves to a 5-ton Domestic Heat Pump (Paper 1355)*. In Proceedings of International Refrigeration and Air Conditioning Conference, 2012.

[12] Hanfei Tuo and Pega Hrnjak. *Flash gas bypass in mobile air conditioning system with R134a*. International Journal of Refrigeration, 35(7):1869–1877, 2012.

[13] Jangho Lee and Piotr A Domanski. *Impact of air and refrigerant maldistributions on the performance of finned-tube evaporators with R22 and R407C*. Technical Report DOE/CE/23810-81, Building Environment Division, NIST, 1997.

[14] Sivert Vist. *Two-phase Flow Distribution in Heat Exchanger Manifolds*. PhD thesis, Norwegian University of Science and Technology, Department of Energy and Process Engineering, 2004.

[15] Jun-Hyeung Kim, James E. Braun, and Eckhard A. Groll. *A hybrid method for refrigerant flow balancing in multi-circuit evaporators: Upstream versus downstream flow control*. International Journal of Refrigeration, 32(6):1271–1282, 2009.

[16] Wiebke Brix, Martin Ryhl Kærn, and Brian Elmegaard. *Modelling distribution of evaporating CO2 in parallel minichannels*. International Journal of Refrigeration, 33(6):1086–1094, 2010.

[17] Martin Ryhl Kærn, Wiebke Brix, Brian Elmegaard, and Lars Finn Sloth Larsen. *Compensation of flow maldistribution in fin-and-tube evaporators for residential air-conditioning*. International Journal of Refrigeration, 34(5):1230–1237, 2011.

[18] Gunda Mader, Björn Palm, and Brian Elmegaard. *Maldistribution in air–water heat pump evaporators. Part 2: Economic analysis of counteracting technologies*. International Journal of Refrigeration, 50:217–226, 2015.

[19] M Nakayama, Y Sumida, S Hirakuni, and A Mochizuki. *Development of a refrigerant two-phase flow distributor for a room air conditioner (Paper 497)*. In Proceedings of International Refrigeration and Air Conditioning Conference, pages 313–320, 2000.

[20] Shun Yoshioka, Hyunyoung Kim, and Kazushige Kasai. *Performance Evaluation and Optimization of A Refrigerant Distributor for Air Conditioner*. Journal of Thermal Science and Technology, 3(1):68–77, 2008.

[21] Kathleen De Kerpel. *Refrigerant two-phase flow behaviour and pressure drop up- and downstream of a sharp return bend*. PhD thesis, Ghent University, 2015.

[22] Hugo Canière. *Flow pattern mapping of horizontal evaporating refrigerant flow based on capacitive void fraction measurements*. PhD thesis, Ghent University, 2009.

[23] John R. Thome. *Void Fractions in Two-Phase Flows*. In The Heat Transfer Engineering Data Book III. Wieland-Werke AG, Ulm, 2016.

[24] L. Wojtan. *Experimental and Analytical Investigation of Void Fraction and Heat Transfer During Evaporation in Horizontal Tubes*. PhD thesis, Ecole Polytechnique Fédérale de Lausanne, 2004.

[25] S.Z Rouhani and E Axelsson. *Calculation of void volume fraction in the subcooled and quality boiling regions*. International Journal of Heat and Mass Transfer, 13(2):383 – 393, 1970.

[26] D. Steiner. *Heat Transfer to Boiling Saturated Liquids*. In VDI-Wärmeatlas. Springer, 1993.

[27] T.N. Wong and Y.K. Yau. *Flow patterns in two-phase air-water flow*. International Communications in Heat and Mass Transfer, 24(1):111 – 118, 1997.

[28] Leszek Wojtan, Thierry Ursenbacher, and John R. Thome. *Investigation of flow boiling in horizontal tubes: Part I—A new diabatic two-phase flow pattern map*. International Journal of Heat and Mass Transfer, 48(14):2955–2969, 2005.

[29] P Barbieri, José M.Saiz Jabardo, and Enio P. Bandarra Filho. *Flow patterns in convective boiling of refrigerant R-134a in smooth tubes of several diameters*. In Proceedings of the 5th European Thermal-Sciences Conference, 2008.

[30] Hugo Canière, Bruno Bauwens, Christophe T'Joen, and Michel De Paepe. *Mapping of horizontal refrigerant two-phase flow patterns based on clustering of capacitive sensor signals*. International Journal of Heat and Mass Transfer, 53(23-24):5298–5307, 2010.

[31] Wanchun Sun, Yanchu Liu, Kui He, and Shuangfeng Wang. *The phase distribution of gas-liquid two-phase flow in microimpacting T-junctions with different branch channel diameters*. Chemical Engineering Journal, 333:34–42, 2018.

[32] Nan Zheng, Li Zhao, and Jinjia Wei. *Experimental research on liquid-vapor two-phase flow separation of zeotropic mixtures at an impacting T-junction*. Experimental Thermal and Fluid Science, 89:140–152, 2017.

[33] Nan Zheng, Yunho Hwang, Li Zhao, and Shuai Deng. *Experimental study on the distribution of constituents of binary zeotropic mixtures in vertical impacting T-junction*. International Journal of Heat and Mass Transfer, 97:242–252, 2016.

[34] Nan Zheng, Li Zhao, Yunho Hwang, Jing Zhang, and Xingyang Yang. *Experimental study on two-phase separation performance of impacting T-junction*. International Journal of Multiphase Flow, 83:172–182, 2016.

[35] Jinfang Chen, Shuangfeng Wang, Hongfeng Ke, Mi Zhou, and Xuanyou Li. *Experimental investigation of annular two-phase flow splitting at a microimpacting T-junction*. Chemical Engineering Science, 118:154–163, 2014.

[36] Jinfang Chen, Shuangfeng Wang, Xinqiang Zhang, Hongfeng Ke, and Xuanyou Li. *Experimental investigation of two-phase slug flow splitting at a micro impacting T-junction*. International Journal of Heat and Mass Transfer, 81:939–948, 2015.

[37] M.A. Mohamed, H.M. Soliman, and G.E. Sims. *Effects of pipe size and system pressure on the phase redistribution in horizontal impacting tee junctions*. Experimental Thermal and Fluid Science, 54:219–224, 2014.

[38] C Bertani, M Malandrone, and B Panella. *Experimental study on the flow patterns and the two-phase pressure drops in a horizontal impacting T-Junction*. Journal of Physics: Conference Series, 501, 2014.

[39] Hanfei Tuo and Pega Hrnjak. *Vapor–liquid separation in a vertical impact T-junction for vapor compression systems with flash gas bypass*. International Journal of Refrigeration, 40:189–200, 2014.

[40] A.M. Elazhary and H.M. Soliman. *Single- and two-phase pressure losses in a horizontal mini-size impacting tee junction with a rectangular cross-section*. Experimental Thermal and Fluid Science, 41:67–76, 2012.

[41] A M Elazhary and H M Soliman. *Two-phase flow in a horizontal mini-size impacting T-junction with a rectangular cross-section*. International Journal of Multiphase Flow, 42:104–114, 2012.

[42] M.A. Mohamed, H.M. Soliman, and G.E. Sims. *Experimental investigation of two-phase flow splitting in an equal-sided impacting tee junction with inclined outlets*. Experimental Thermal and Fluid Science, 35(6):1193–1201, 2011.

[43] M.A. Mohamed, H.M. Soliman, and G.E. Sims. *Conditions for complete phase separation in an impacting tee junction at various inclinations of the outlet arms*. International Journal of Multiphase Flow, 47:66–72, 2012.

[44] Alen Savo Milosevic. *Flash gas bypass concept utilizing low pressure refrigerants*. PhD thesis, University of Illinois at Urbana-Champaign, 2010.

[45] A P Doherty, A Murphy, and P L Spedding. *Fluid flow in an impacting symmetrical tee junction II: two-phase air/water flow*. Asia-Pacific Journal of Chemical Engineering, 4(4):424–431, 2009.

[46] A. Murphy, P. L. Spedding, and A. P. Doherty. *Two-phase bifurcated dividing pipe flow*. Asia-Pacific Journal of Chemical Engineering, 4(1):73–79, 2009.

[47] A M F El-Shaboury, H M Soliman, and G E Sims. *Two-phase flow in a horizontal equal-sided impacting tee junction*. International Journal of Multiphase Flow, 33(4):411–431, 2007.

[48] Shuangfeng Wang and Masahiro Shoji. *Fluctuation characteristics of two-phase flow splitting at a vertical impacting T-junction*. International Journal of Multiphase Flow, 28(12):2007–2016, 2002.

[49] M Tshuva, D Barnea, and Y Taitel. *Two-phase flow in inclined parallel pipes*. International Journal of Multiphase Flow, 25(6-7):1491–1503, 1999.

[50] Dimitri Hatziavramidis, Bing Sun, and Dimitri Gidaspow. *Gas-liquid flow through horizontal tees of branching and impacting type*. AIChE journal, 43(7):1675–1683, 1997.

[51] T. Fujii, N. Takenaka, T. Nakazawa, and H. Asano. *The phase separation characteristics of a gas–liquid two-phase flow in the impacting T-junction*. In Proc. 2nd Int. Conf. on Multiphase Flow, Kyoto, Japan, pages 627–632, 1995.

[52] Marcel Ottens, Arthur de Swart, Huub C.J. Hoefsloot, and Peter J. Hamersma. *Gas-Liquid Flow Splitting in Regular, Reduced and Impacting T Junctions.* Impiantistica Italiana, 8:26–37, 1995.

[53] K.C. C Hong and Suzanne Griston. *Two-Phase Flow Splitting at an Impacting Tee*. SPE Production & Facilities, 10(3):184–190, 1995.

[54] Sze-Foo Chien and Mark T. Rubel. *Phase Splitting of Wet Steam in Annular Flow Through a Horizontal Impacting Tee Junction*. SPE Production Engineering, 7(04):368–374, 1992.

[55] L Lightstone, S I Osamusali, and Jen-Shih Chang. *Gas-liquid two-phase flow in symmetrically dividing horizontal tubes*. AIChE Journal, 37(1):111–122, 1991.

[56] S T Hwang, H M Soliman, and R T Lahey Jr. *Phase separation in impacting wyes and tees*. International Journal of Multiphase Flow, 15(6):965–975, 1989.

[57] B. J. Azzopardi, A. Purvis, and A. H. Govan. *Flow split of churn flow at a vertical impacting T*. Technical report, Harwell Laboratory, Thermal Hydraulics Division, 1986.

[58] B.J. Azzopardi, A. Purvis, and A.H. Govan. *Annular two-phase flow split at an impacting T*. International Journal of Multiphase Flow, 13(5):605–614, 1987.

[59] Akimi Serizawa, Ziping Feng, and Zensaku Kawara. *Two-phase flow in microchannels*. Experimental Thermal and Fluid Science, 26(6):703 – 714, 2002.

[60] Mikio Suo and Peter Griffith. *Two-phase flow in capillary tubes*. Journal of Basic Engineering, 86(3):576–582, 1964.

[61] R Nagai, Y Tabata, M Sadatomi, A Kawahara, and A Santoso. *Experimental Study on Two-Phase Pressure Drop through Horizontal Mini-Channel with Y-Branch*. Journal of Mechanical Engineering and Automation, 6(4):78–84, 2016.

[62] John R. Thome. *Boiling of new refrigerants: A state-of-the-art review*. International Journal of Refrigeration - Revue Internationale du Froid, 19(7):435–457, 1996.

[63] B. J. McKeon and A. J. Smits. *Static pressure correction in high Reynolds number fully developed turbulent pipe flow*. Measurement Science and Technology, 13(10):1608–1614, 2002.

[64] Kathleen De Kerpel, Sven De Schampheleire, Timothy De Keulenaer, and Michel De Paepe. *Two-phase flow regime assignment based on wavelet features of a capacitance signal*. International Journal of Heat and Fluid Flow, 56:317–323, 2015.

[65] K De Kerpel, B Ameel, and C T'Joen. *Flow regime based calibration of a capacitive void fraction sensor for small diameter tubes*. International Journal of Refrigeration, 36:390–401, 2013.

[66] V. Gnielinski. *New equations for heat and mass transfer in the turbulent flow in pipes and channels*. NASA STI/Recon Technical Report A, 75:8–16, 1975.

[67] P.R. Bevington and D.K. Robinson. *Data Reduction and Error Analysis for the Physical Sciences*. McGraw-Hill, 3th edition, 2003.

[68] Julius O. Smith. *Spectral Audio Signal Processing*. `http://-ccrma.stanford.edu/~jos/sasp/`, 2011. online book, 2011 edition.

[69] J.C. Dallman, J.E. Laurinat, and T.J. Hanratty. *Entrainment for horizontal annular gas-liquid flow*. International Journal of Multiphase Flow, 10(6):677–689, 1984.

[70] L.E. Patruno, P.A. Marchioro Ystad, C.B. Jenssen, J.M. Marchetti, C.A. Dorao, H.F. Svendsen, and H.A. Jakobsen. *Liquid entrainment—Droplet size distribution for a low surface tension mixture*. Chemical Engineering Science, 65(18):5272–5284, 2010.

[71] Andrea Cioncolini and John R. Thome. *Prediction of the entrained liquid fraction in vertical annular gas–liquid two-phase flow*. International Journal of Multiphase Flow, 36(4):293–302, 2010.

[72] H. Ito and K. Imai. *Energy Losses at 90° Pipe Junctions*. Journal of the Hydraulics Division, 99(9):1353–1368, 1973.

[73] Sze-Foo Chien and Mark T. Rubel. *Phase Splitting of Wet Steam in Annular Flow Through a Horizontal Branching Tee*. SPE Production & Facilities, 7(4):368–374, 1996.

[74] Ian H. Bell, Jorrit Wronski, Sylvain Quoilin, and Vincent Lemort. *Pure and Pseudo-pure Fluid Thermophysical Property Evaluation and the Open-Source Thermophysical Property Library CoolProp*. Industrial & Engineering Chemistry Research, 53(6):2498–2508, 2014.

[75] John Robert Taylor. *An Introduction to Error Analysis: The Study of Uncertainties in Physical Measurements*. University Science Books, 1997.

[76] Thomas Leininger. *Statistics 101*. `http://www2.stat.duke.edu/~tjl13/s101/slides/unit6lec3H.pdf`. Accessed: 04-09-2018.

[77] E. W. Lemmon. *REFPROP 7, Enthalpy uncertainty*, November 2006.

[78] W. Wagner and A. Pruss. *The IAPWS Formulation 1995 for the Thermodynamic Properties of Ordinary Water Substance for General and Scientific Use*. Journal of Physical and Chemical Reference Data, 31(2):387–535, 2002.

[79] Reiner Tillner-Roth and Akimichi Yokozeki. *An international standard equation of state for difluoromethane (R-32) for temperatures from the triple point at 136.34 K to 435 K and pressures up to 70 MPa*. Journal of Physical and Chemical Reference Data, 26(6):1273–1328, 1997.

[80] Reiner Tillner-Roth and Hans Dieter Baehr. *A International Standard Formulation for the Thermodynamic Properties of 1,1,1,2-Tetrafluoroethane (HFC-134a) for Temperatures from 170 K to 455 K and Pressures up to 70 MPa*. Journal of Physical and Chemical Reference Data, 23(5):657–729, 1994.

[81] E. W. Lemmon. *Pseudo-Pure Fluid Equations of State for the Refrigerant Blends R-410A, R-404A, R-507A, and R-407C*. International Journal of Thermophysics, 24(4):991–1006, 2003.

[82] E.W. Lemmon and R.T Jacobsen. *A Generalized Model for the Thermodynamic Properties of Mixtures*. International Journal of Thermophysics, 20(3):825–835, 1999.

[83] M. Richter, M. O. McLinden, and E. W. Lemmon. *Thermodynamic Properties of 2,3,3,3-Tetrafluoroprop-1-ene (R1234yf): Vapor Pressure and p-rho-T Measurements and an Equation of State*. Journal of Chemical & Engineering Data, 56(7):3254–3264, 2011.

[84] Eric W. Lemmon and Richard T. Jacobsen. *A new functional form and new fitting techniques for equations of state with application to pentafluoroethane (HFC-125)*. Journal of Physical and Chemical Reference Data, 34(1):69–108, 2005.

[85] Volker Gnielinski. *G2 Heat Transfer in Concentric Annular and Parallel Plate Ducts*, pages 701–708. Springer Berlin Heidelberg, Berlin, Heidelberg, 2010.

[86] Stuart W. Churchill and Humbert H.S. Chu. *Correlating equations for laminar and turbulent free convection from a horizontal cylinder*. International Journal of Heat and Mass Transfer, 18(9):1049–1053, 1975.

[87] D. C. Meeker. *Finite Element Method Magnetics, Version 4.2 (25Feb2018 Build)*. `http://www.femm.info`.

[88] O. Shoham, J.P. Brill, and Y. Taitel. *Two-Phase Flow Splitting in a Tee Junction- Experiment and Modeling*. Chemical Engineering Science, 42:2667–2676, 1987.